Magnetic properties of small multi-layered rings

by

Wonjoon Jung

B.S. Metallurgical Engineering, 1998
Seoul National University, Seoul, Korea

M.S. Materials Science and Engineering, 2000
Seoul National University, Seoul, Korea

Submitted to the Department of Materials Science and Engineering
in Partial Fulfillment of the Requirements for the Degree of

Doctor of Philosophy in Materials Science and Engineering

at the
Massachusetts Institute of Technology

September 2007

Signature of Author: ______________________________
Department of Materials Science and Engineering
August 10, 2007

Certified by: ______________________________
Caroline A. Ross
Professor of Materials Science and Engineering
Thesis Supervisor

Accepted by: ______________________________
Samuel M. Allen
POSCO Professor of Physical Metallurgy
Chair, Departmental Committee on Graduate Students

Magnetic properties of small multi-layered rings

by

Wonjoon Jung

Submitted to the Department of Materials Science and Engineering
On August 10, 2007 in Partial Fulfillment of the Requirements for the
Degree of Doctor of Philosophy in Materials Science and Engineering

Abstract

Thin film rings can be an alternative geometry of magnetic memory cells, in which data bits are stored by the chirality of the flux-closed or 'vortex' state of the ring. The absence of the stray field in the vortex state is advantageous of high density data storage. Elliptical rings with 3 / 2 μm major / minor diameter and widths of 300 nm above were fabricated from multi-layer thin film structures such as the ferromagnetic-antiferromagnetic exchange bias bilayer or giant magnetoresistance (GMR) spin valve structure, and their magnetic and magnetoelectric properties were investigated.

Exchange-biased elliptical rings show an interplay between shape anisotropy and exchange anisotropy. When both the exchange bias and applied field are oriented along the major axis, an elliptical ring shows a shifted hysteresis loop and strong in-plane anisotropy. The switching behavior and vortex state stability of the rings are strongly dependent on the pinning direction and applied field direction relative to the major axis of the ellipse.

It has proven difficult to control the vortex chirality in a simple manner. A model is described that predicts the vortex chirality of an elliptical magnetic ring as a function of the direction of the applied field and of the exchange bias, based on the change in the energy of the system as the domain walls move. Experimental measurements of the chirality in Co and Co / IrMn magnetic rings with a 3.2 μm major axis are in excellent agreement with the model. The vortex circulation direction can therefore be tailored with an appropriate combination of the applied field direction and exchange bias direction with respect to the major axis.

NiFe / Cu / Co / IrMn spin valve elliptical rings with 3.2 / 1.9 μm major / minor diameter and the width of 340 – 370 nm were fabricated and the magnetoresistance (MR) of the rings were measured with applying an in-plane field. Spin valve rings show asymmetric MR curves with three different MR states. Minor loop MR measurements, which give rise to switching of only the free layer of the spin valve ring, demonstrate that an individual control of the vortex chirality in each ferromagnetic layer is possible in a ring-shaped multilayered structure, such as a spin valve ring.

Thesis Supervisor: Caroline A. Ross
Title: Professor of Materials Science and Engineering

Table of contents

List of figures

List of tables

Acknowledgements

I have been a student for the past 24 years, and I am about to finish my education with a doctoral degree from MIT. Such a long education in excellent schools is certainly a privilege that not many people can enjoy. That is why with this doctoral degree I feel obliged to contribute to society. As a Christian, I will live my post-student life to benefit others using what I have learned.

I would like to thank my advisor Professor Caroline Ross for her support and patience throughout my stay at MIT. Her encouragement and insightful advices helped me overcome frustration and make progress. I am so grateful to my committee members, Professor Robert (Bob) O'Handley, Professor Harry Tuller, and Professor Henry (Hank) Smith for valuable suggestions on my research. Discussions I had with them allowed me to notice what I had overlooked and bolster my understanding of the physical principles involved with my research topic.

I feel blessed to be a part of Ross group. I want to thank all of whom I met in the group for their friendship and support, especially to Dr. Fernando Castaño for being a good teacher and a wonderful friend. I also thank Dr. Debbie Morecroft, Irénée Colin, and Alexander Eilez who worked with me on the magnetic ring project.

I would like to thank people in Nanostructures laboratory (NSL) for sharing their expertise, especially to Dr. Rajesh Menon, Bryan Cord, and Jim Daley. Rajesh helped me make ring structures using ZPAL.

I am grateful to David Bono for helping me make experimental equipments for field cooling, and to Libby Shaw for teaching me how to use AFM/MFM.

I have to thank Dr. Mary Ellen Rhinehart in MIT medical. She is one of the most wonderful persons that I have ever met in my life. I will remember her hospitality and kindness shown me at the most difficult of times.

I want to thank my friends at MIT. There are so many names and so many good memories going through my mind right now. I miss my mom Heesoon and my sister Youjin who live in Korea. Even though we are apart, they are always in my thoughts and prayers. Finally I thank my wife Eunsil for the joy she brought to my life. Eunsil, I want to say this. I love you.

Chapter 1

Introduction

1.1 Overview

Magnetism is a subject of intense research interest and has many uses in electronics and data recording. In the last two decades there have been major breakthroughs in magnetic materials that enabled important progress in magnetic data storage and spintronics. One example of such developments is the discovery of giant magnetoresistance (GMR) [1-7]. GMR is a magnetic phenomenon that occurs in alternating magnetic-nonmagnetic multilayers, in which the electric resistance varies depending on the relative magnetization of the magnetic layers. Introduction of GMR read heads for magnetic disk drives enabled a remarkable 100% annual growth rate of the areal density of hard disks to continue for several years [8].

Research on small magnetic elements of various multilayer thin film structures is of significant fundamental and practical interest. Small magnetic structures display a range of magnetic states and phenomena, which can be utilized for magnetic memory [9-13] and logic devices [14-18], and magnetic sensors [19]. The magnetization states and switching behaviors of the small magnets are closely related to their shape, dimensions, and thin film structures. Investigation on such relationships would provide useful insights into the magnetism in small elements and control over the device operation.

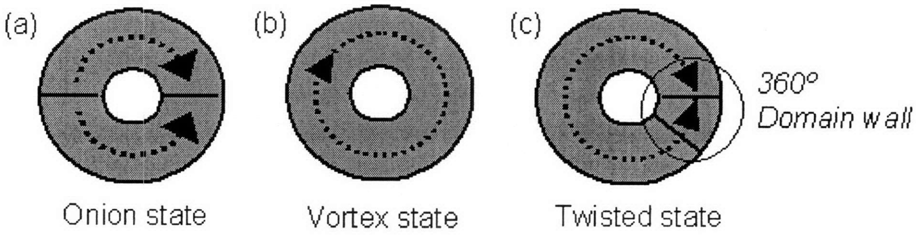

Figure 1.1 Schematic illustrations of the magnetization states of ferromagnetic rings. Arrows represent the direction of the magnetization, and solid lines the 180° domain walls.

Most work on small thin film magnetic elements has been carried out on magnetic bars, wires, and disks [20-32]. Recently there has been an upsurge in interest in magnetic rings [33-48]. This thesis concerns the magnetic properties of ring-shaped multilayer structures. Relatively little attention has been given to multilayered magnetic rings despite their technological importance and scientific interest. In this work, the effect of shape, dimension, and thin film structures on the magnetic states and magnetization reversal of ring magnets is investigated and control of the magnetic properties of rings using those effects is demonstrated. This chapter will provide background information and a literature survey on the ring magnets, exchange bias, and GMR structures as a general introduction to the thesis.

1.2 Magnetic rings

A range of topologically distinct magnetic states has been identified in thin film magnetic rings. As a ring is saturated in an applied field and the field diminishes, the magnetization of each half of the ring is oriented following the boundary of the ring, and two head-to-head domain walls form (Fig. 1.1(a)). This is an equilibrium magnetic state referred to as the 'onion' state [42].

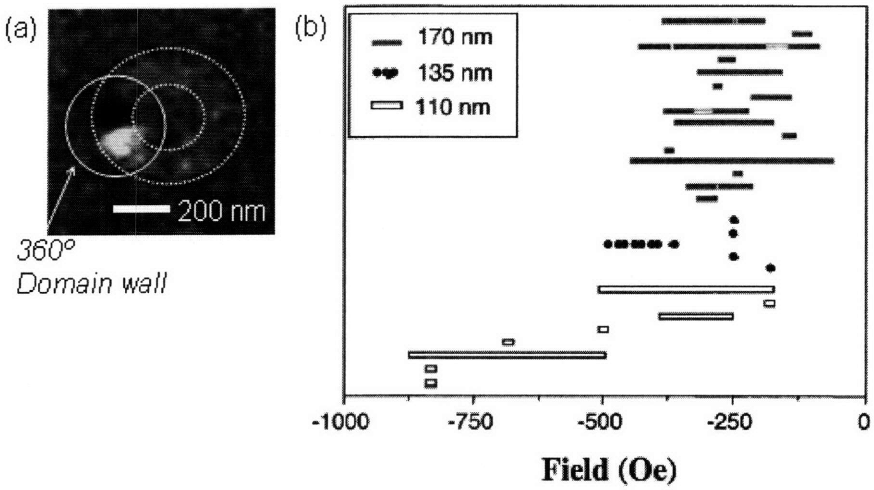

Figure 1.2 Magnetic force micrograph (a) and field ranges (b) over which the twisted states are stable in arrays of 520-nm-diameter Co (10nm) rings of width 110, 135, and 170 nm [49]. Dotted line in (a) shows the boundary of the ring. Each line in (b) represents the result of an individual ring measured in the experiment.

As the field continues to reverse, one of the domain walls of the onion state unpins and moves until it approaches and annihilates the other wall and the 'vortex' state forms (Fig. 1.1(b)). In a perfect ring the two domain walls of the onion state might unpin at the same field and rotate simultaneously. However, irregularities in the shape and defects in the film structure result in a difference in the pinning strength for each domain wall and one wall usually unpins earlier than the other. The vortex state is a flux-closed state, in which the magnetization is oriented circumferentially and there are no domain walls. This state has been proposed for data storage devices in which the chirality of the magnetization rotation is utilized to store a data bit [9], as was practiced in one of the first-generation computer memories, the magnetic core memory.

Sometimes the 'twisted' magnetic state [49, 50] that precedes vortex formation appears during the onion-to-vortex transition (Fig. 1.1(c)). The twisted state is a metastable magnetic state that contains an in-plane 360° domain wall, which is formed by the movement of one of the onion state 180° domain walls towards the other wall. Fig. 1.2(a) shows the 360° domain walls in the twisted states of Co rings imaged using magnetic force microscopy (MFM) [50]. The twisted state is ultimately annihilated to generate the vortex state and the field range over which the twisted state persists has a wide distribution as shown in Fig. 1.2(b). Some of the twisted states remain stable over considerable field ranges of several hundreds of Oe. As the field reverses further, the vortex state switches into the reversed onion state.

The switching behavior of the rings is determined by a number of different factors such as the shape, geometrical parameters, and crystalline structure of the magnetic material. For example, when a thin, wide ring is reversed from the onion state, a direct transition from the onion state to the reverse onion state (Fig. 1.3(a)) is more likely to occur instead of the two step switching [34, 46] shown in Figure 1.3(b). Because the vortex or twisted state has zero or very close to zero net magnetization respectively and the twisted-to-vortex transition does not lead to a change in magnetic moment, the magnetization curve of the rings shown in Figure 1.3(b) exhibits two-step switching.

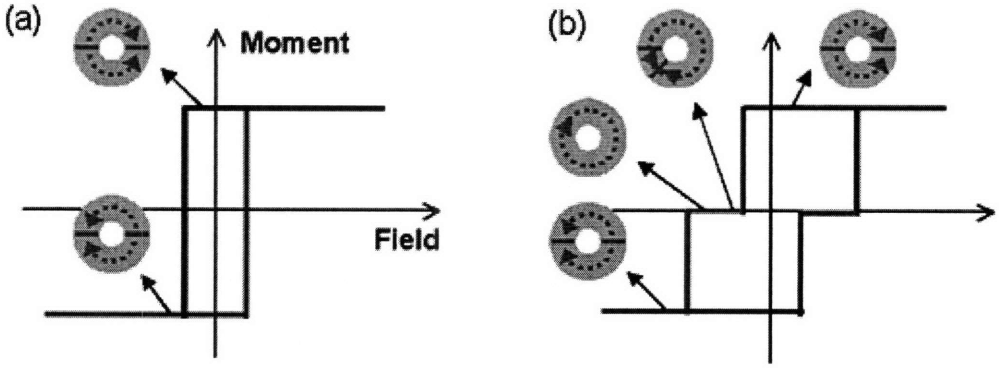

Figure 1.3 Schematics of switching behaviors and corresponding magnetic states of a ring magnet: (a) direct switching from the forward onion to the reverse onion. (b) two-step switching via formation of the vortex state or the twisted state.

The reversal mechanism can be explained by taking into account the competition between two energy terms, the exchange energy and the magnetostatic energy [51]. The exchange energy is a measure of the strength with which the electron spins in a ferromagnetic material align themselves parallel to each other. Therefore, in a ferromagnet, uniform magnetization leads to the minimum exchange energy. The exchange energy density f_{EX} can be expressed as

$$f_{EX} = -A\cos\theta_{ij} \qquad (1.1)$$

where A denotes the exchange stiffness constant, typically $1 \sim 2 \times 10^{-11}$ J/m for most ferromagnetic materials, and θ_{ij} is the angle between the two adjacent spin directions i and j.

The magnetostatic energy is the volume integral of the stray field over all space. Generally the formation of domains decreases the magnetostatic energy due to the reduced spatial extent of the stray field. Magnetization vortices also lead to reduction of the magnetostatic energy. However the exchange energy is increased by the formation of domains and vortices.

Formation of the vortex state in a ring is favored if the total free energy is dominated by the magnetostatic energy since the vortex state is free from stray fields. For thin rings the magnetostatic energy is less significant compared to the exchange energy. That prevents thin rings from forming the vortex state, and thin rings switch directly into the reverse onion state via nucleation of reverse domains. For wide rings the magnetic moment is less confined by the boundaries, that is, the local anisotropy is weak. This gives the spins more degree of freedom to rotate and allows the nucleation of a reverse domain more easily compared with a narrow ring.

The thickness and width of the ring also influence the switching fields. Vortex stability, the difference between the onion-to-vortex switching field and the vortex-to-reverse onion switching field, generally decreases as the width increases or the thickness decreases. This dependence can be understood using similar reasoning to that used to explain dependence of vortex formation on those parameters.

The microstructure of the materials also affects the switching behavior of the rings. Magnetic materials have preferences for the magnetization to lie in a particular crystalline direction, which is referred to as the magnetocrystalline anisotropy. For instance, hcp Co has a uniaxial crystalline anisotropy with the easy axis along the c axis and fcc Ni and bcc Fe have a cubic anisotropy. In a single-crystal fcc-Co ring, the cubic magnetocrystalline anisotropy suppresses the onion-to-vortex transition when a field is applied along the magnetocrystalline hard axis [39].

The 180° domain walls of the rings can adopt two types of configuration, a transverse wall with an in-plane 180° rotation of magnetization (Fig. 1.4(a)) and a vortex wall (Fig. 1.4(b)). The transverse wall has high magnetostatic energy due to the stray field, while the vortex wall, which exhibits much less stray field, has higher exchange energy than the transverse wall. According to the micromagnetic simulations carried out by McMichael and Donahue [52], the increase in the exchange energy as the transverse wall changes into the vortex wall is linearly proportional to the thickness. However the reduction in the magnetostatic energy with such a transition is proportional to the thickness quadratically. Therefore in thick rings the vortex domain wall is expected to be favored. The vortex wall is also favored in a wide ring since the magnetostatic energy reduction is more sensitive to the width of the ring [53].

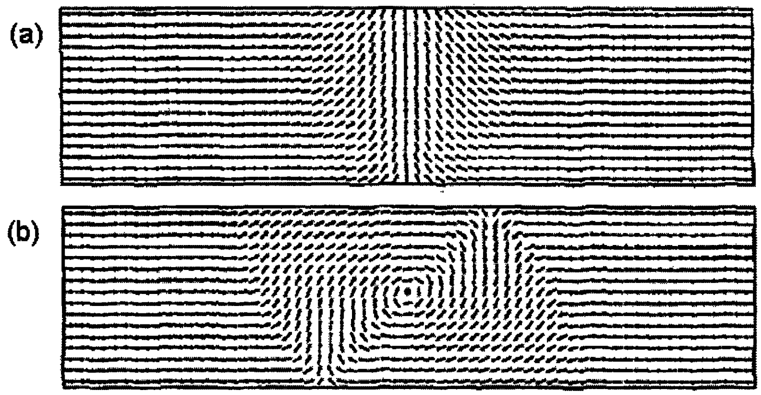

Figure 1.4 Calculated spin configurations of a transverse domain wall in a 2nm thick, 250 nm wide NiFe strip (a), and of a vortex wall in a 32 nm thick, 250 nm wide NiFe strip (b) [52].

Modification of the shape also affects the magnetic properties of the rings. A notch, flat edge [40, 54, 55] or width variation [43, 47, 56] around the ring was introduced in order to locate the domain walls at a desired position or to control the magnetization direction of the vortex state, which is referred to as the vortex chirality. Control of the vortex chirality is very important for applications in data storage, since the ring shape memory elements are proposed to store data bits according to their chirality. The chirality can be also controlled by the distortion of the ring into an ellipse [57]. The elliptical ring is a useful test bed for studies on the domain wall nucleation and propagation due to its well defined onion state with strong preferential positions for the domain walls. The shape anisotropy of elliptical rings allows the vortex stability to change depending on the field direction with respect to the major axis [58, 59]. The vortex stability is lower as the field is applied along the minor axis.

Relatively few studies have been carried out on the effect of the multilayer thin film structures on the properties of the rings, in spite of its importance in technological applications. There are some reports on rings with exchange-biased structures [41, 60-62]. A few theoretical and experimental studies have been carried out on rings consisting of Co / Cu / NiFe GMR structures [63-70].

1.3 Exchange bias

1.3.1 Introduction of ferromagnetic-antiferromagnetic exchange coupling

When a ferromagnet (FM) is in contact with an antiferromagnet (AFM), in which atomic moments couple in antiparallel arrangements with zero net magnetization, a magnetic anisotropy is induced in the ferromagnet. This phenomenon is called ferromagnetic-antiferromagnetic exchange coupling, and the anisotropy is referred to as the exchange anisotropy [71-73]. The exchange anisotropy appears typically after field cooling, in which a FM / AFM couple is cooled from a temperature above the Néel temperature (T_N) in the presence of an external field. The field cooling procedure results in a shifted hysteresis loop (exchange bias $H_E = (H_2 + H_1) / 2$) and an increase in the coercivity ($H_C = (H_2 - H_1) / 2$) of the FM / AFM couple. Figure 1.5 shows an example of a shifted hysteresis loop of Fe / FeF_2 and a torque measurement of a Co / CoO film [72]. The torque curve exhibits one absolute minimum, instead of two minima 180° apart, which is a characteristic of the uniaxial anisotropy. This means the FM / AFM couple has only one easy direction and the exchange anisotropy is unidirectional.

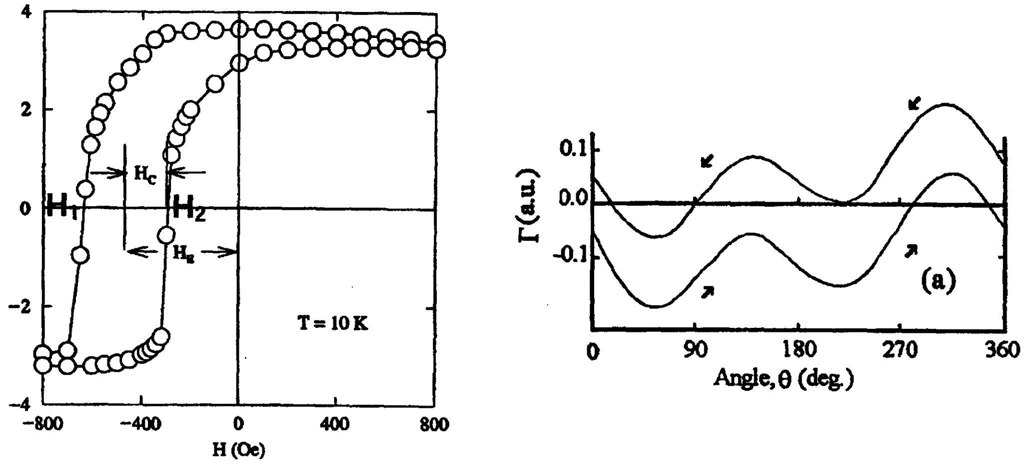

Figure 1.5 Left: hysteresis loop of a FeF_2/Fe bilayer at T = 10K after field cooling, H_E denotes the exchange bias, and H_C the coercivity. Right: Torque magnetization of an oxidized Co film at T = 77K after field cooling [72].

The exchange bias effect has been widely used in modern technology since the introduction of giant magnetoresistive (GMR) spin-valve heads in magnetic recording.
In the following sections, we will discuss several theoretical models for the exchange coupling mechanisms, antiferromagnetic materials, and magnetic properties of layered systems.

1.3.2 Discovery of Meiklejohn and Bean

Exchange bias was discovered by Meiklejohn and Bean in 1956 by observing the hysteresis loops of fine cobalt particles [74, 75]. The hysteresis loop of Co particles shifted when the particles were cooled in a magnetic field. This effect was understood in terms of the presence of an antiferromagnetic CoO thin layer, which naturally grows on the surface of the particles. CoO formation leads to exchange coupling between Co and CoO as it is cooled in a magnetic field through its Néel temperature (-3 °C). Meiklejohn and Bean presumed that the uncompensated spins in the CoO (111) plane at the Co / CoO interface causes the bias.

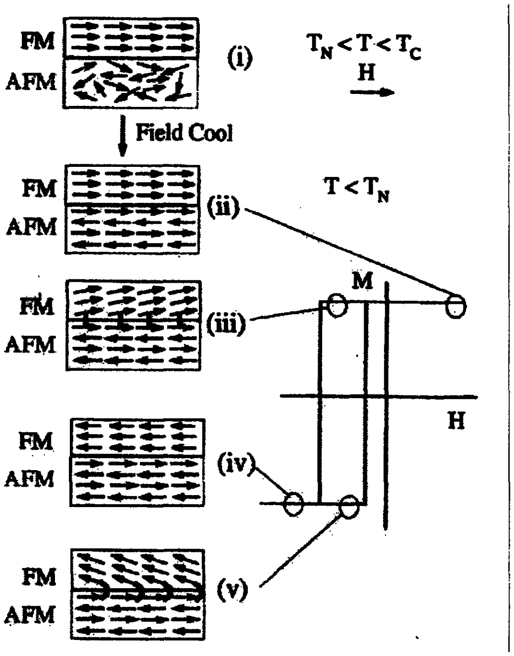

Figure 1.6 Schematic diagram of the spin configuration of an FM-AFM bilayer at different stages (i)-(v) of an exchange-biased hysteresis loop [72].

Meiklejohn and Bean's explanation is described in Figure 1.6, which shows the spin configurations of a FM / AFM bilayer at various states of an exchange biased hysteresis loop. A magnetic field, which is enough to saturate the FM layer, is applied to the system in the temperature $T_N < T < T_C$, where T_C represents the Curie temperature of the FM. Since $T > T_N$, the antiferromagnetic spins remain in a disordered state. After field cooling (Fig. 1.6(ii), $T < T_N$), the AFM spins at the interface are aligned parallel to the FM spins while the rest of the AFM spins form an antiparallel configuration. To reverse the FM layer a larger field is needed due to the exchange coupling, while the FM switches at a smaller field in a direction parallel to the coupling. Therefore, the hysteresis loops exhibits a shift in the field axis, which is referred to as the exchange bias.

In a simple model the total free energy per unit area can be written as

$$E = -\mu_0 H M_F t_F \cos(\theta - \beta) + K_F t_F \sin^2 \beta + K_{AF} t_{AF} \sin^2 \alpha - J_{INT} \cos(\beta - \alpha) \qquad (1.2)$$

where H: the external field on the ferromagnetic layer,
M_F: the saturation magnetization of the ferromagnet,
t_F: the thickness of the ferromagnet,
t_{AF}: the thickness of the antiferromagnetic layer,
K_F: the anisotropy constant of the ferromagnet,
K_{AF}: the anisotropy constant of the antiferromagnet,

J_{INT}: the interface coupling constant,
β: the angle between the magnetization and the easy axis of the ferromagnet,
α: the angle between the antiferromagnetic sublattice magnetization and the antiferromagnetic anisotropy axis,
θ: the angle between the external field and the ferromagnetic anisotropy axis.

If the ferromagnetic anisotropy can be neglected, after minimizing the energy with respect to α and β the exchange bias field is described as

$$H_{eb} = \frac{J_{INT}}{\mu_0 M_F t_F} \alpha \frac{1}{t_F} \qquad (1.3)$$

The following condition is required for the observation of exchange anisotropy

$$K_{AF} t_{AF} \geq J_{INT} \qquad (1.4)$$

These results are commonly observed in experiments on FM / AFM bilayer systems. The exchange bias is inversely proportional to the thickness of the FM layer and no exchange bias appears until the thickness of the AFM reaches a critical value.

The model of Meiklejohn and Bean is an intuitive explanation for the phenomena of exchange bias, however it is too simple to account for various experimental results. The most prominent problem is that its prediction of an exchange bias field is several orders of magnitude larger than all experimental data. In addition, the model supposes a perfectly smooth interface containing uncompensated spins. Some experimental results conflict with this model. For example, It has been reported that polycrystalline AFM layers show higher exchange fields than single crystal AFM films [76]. Exchange bias was found not only in an uncompensated FM / AFM interface but also in a fully compensated interface [77].

1.3.3 Domain wall model of Mauri

Mauri et al. [78] proposed the presence of a planar domain wall at the FM / AFM interface which results in a reduced exchange energy compared to the model of Meiklejohn and Bean. In Mauri's model the AFM is supposed to be infinitely thick and have much lower domain wall energy than the FM layer so the domain wall forms only in the AFM layer. The FM layer is assumed to be thin and all the spins in the FM are parallel.

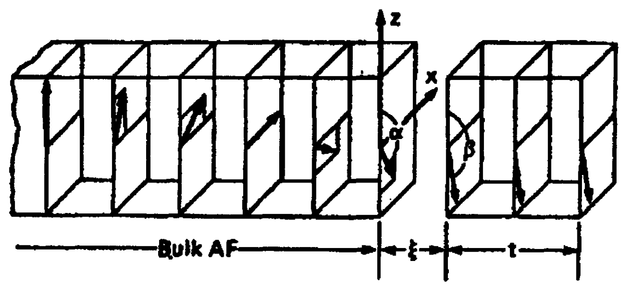

Figure 1.7 Magnetic model of Mauri for the interface of a thin ferromagnetic film on a thick antiferromagnetic substrate [78].

The total free energy per unit area of the system can be described as

$$E = 2\sqrt{A_{AF}K_{AF}}(1-\cos\alpha) + \frac{A_{AF-F}}{\xi}(1-\cos(\alpha-\beta)) + K_F t_F \cos^2\beta +_{\mu 0} HM_F t_F \cos(\theta-\beta)$$

(1.5)

K_{AF} and A_{AF} denote the anisotropy constant and the exchange stiffness of the AFM, respectively, whereas K_F is the anisotropy constant of the FM. A_{AF-F} is the interfacial coupling constant, ξ the distance between the two layers, t_F the FM thickness, H the external field and θ the angle of H with respect to the easy axis of the FM. The first term in Equation (1.5) is the domain wall energy in the AFM and the second the interface energy. The third and the last terms denote the anisotropy energy and the Zeeman energy of the FM, respectively.

Minimizing Equation (1.5) with respect to α and β for a given external field yields the following two limiting cases.

When the interface energy is much larger than the domain wall energy (strong interfacial coupling),

$$H_{eb} = -2\frac{\sqrt{A_{AF}K_{AF}}}{\mu_0 M_F t_F} \qquad (1.6)$$

When the interface energy is much smaller than the domain wall energy (weak interfacial coupling)

$$H_{eb} = -\frac{A_{AF-F}}{\xi\mu_0 M_F t_F} \qquad (1.7)$$

With $J_{INT} = A_{AF-F} / \xi$, the above becomes identical to the expression of Meiklejohn and Bean, Equation (1.3).

In the case of strong interface coupling and low domain wall energy, the model successfully reduces the exchange bias by a factor of 100, which is consistent with experimental observations. However, most experimental data favor rather weak interface coupling and, more importantly, the model still assumes a uniform and perfectly uncompensated interfacial plane, which is non-realistic.

1.3.4 Malozemoff's random field model

Discarding the assumption of a perfectly uncompensated interface in Mauri's model, Malozemoff argued that the roughness and structural defects in the interface cause an imbalance of the interfacial AFM moments [79]. He suggested that the AFM layer breaks up into domains, which are perpendicular to the interface, not planar. A larger number of the AFM domains would lower the interface energy, but enhance the domain wall energy of the system so there is an optimal size of the domains, which is estimated as

$$L \approx \pi \sqrt{\frac{A}{K}} \qquad (1.8)$$

where A represents the exchange constant in the antiferromagnet and K the uniaxial anisotropy.

Malozemoff's random field model argues that in a region that N antiferromagnetic spins exist average $z\sqrt{N}$ spins are uncompensated, where z is a number in the order of unity. The number of spins N in the area L^2 is $N = L^2 / a^2$, where a denotes the lattice constant. Accordingly, the exchange bias field is

$$H_{eb} = -2\frac{z\sqrt{AK}}{\pi^2 \, M_F t_F} \qquad (1.9)$$

This equation is very similar to the one of Mauri's for large interfacial energy, Equation (1.6).

Malozemoff's model explains several properties of exchange-biased systems. For instance, the training effect can be explained by the annihilation of AFM domains during the first hysteresis cycle. However, this model contains a statistical argument for the uncompensated spin density, which it is not explicitly convincing.

1.3.5 Koon's spin flop coupling at compensated interfaces

Nogués et al. found a large bias field for the compensated (110) interface orientation in the FeF_2 / Fe bilayer system [77]. Further, they discovered that the exchange bias field decreases with increasing interface roughness. Also Jungblut et al. suggested that the exchange coupling occurs by the AFM moments aligned along the AFM easy axis, which is perpendicular to the FM moment.

In order to explain these results, Koon proposed the spin flop model at fully compensated interfaces [80]. In his model, AFM spins are aligned along the AFM easy axis, which is perpendicular with respect to the FM spins (Fig. 1.8). In the vicinity of the interface, AFM spins are canted by a small angle θ toward the FM magnetization direction as they are coupled to the FM (Fig. 1.8(b)). FM produces a small net moment in the AFM, which is parallel to the magnetization of the FM and perpendicular to the easy axis in the AFM. This model is energetically favored since it is easier to cant the AFM moments with a field applied along the perpendicular direction to the AFM easy axis rather than with a parallel field.

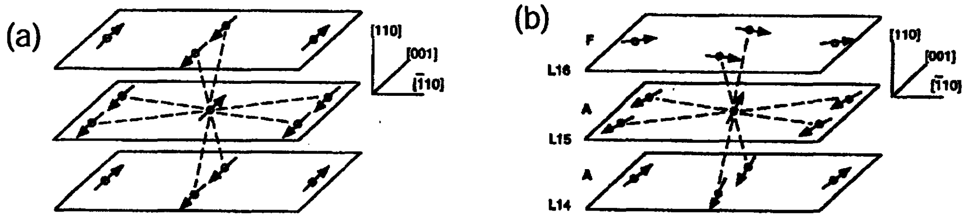

Figure 1.8 Spin configuration of Koon's model inside the antiferromagnet (a), which shows the fully compensated surface. Spins across the FM / AFM interface plane exhibit a perpendicular configuration (b). Exchange bonds are shown by the dashed lines [80].

Koon's model can be an explanation for the existence of an exchange bias in systems with a fully compensated FM / AFM interface. However, calculation results presented by Shulthess and Butler [81] suggest that that Koon's spin flop coupling leads not to a unidirectional anisotropy but results in an unidirectional anisotropy.

1.3.6 Interfacial uncompensated antiferromagnetic spins of Takano

Takano et el. demonstrated the experimental correlation between the interfacial uncompensated CoO spins and the exchange field in polycrystalline CoO / NiFe bilayers [82]. They measured thermoremanent magnetization (TRM) in CoO / MgO layers, and from the data confirmed that the uncompensated moment exists at the CoO interfaces. The measured uncompensated moment represented ~ 1% of the spins in a mono-atomic layer of CoO. They also found that the strength of the exchange field is linearly proportional to the inverse of the CoO crystallite diameter, i.e. $H_{eb} \propto L^{-1}$ in the experiments with the CoO / NiFe bilayers.

A statistical analysis was carried out on the number of uncompensated spins $< \Delta N >$ on a surface inclined at an angle θ to the ferromagnetically coupled (111) planes (Fig. 1.9). From the analysis they found that the following relationship exists between $< \Delta N >$ and the domain size L, $< \Delta N > \propto L^{0.90\sim1.04}$. Because the exchange field is proportional to $< \Delta N > / L^2$, the analysis suggests $H_{eb} \propto L^{-1}$, which was confirmed by experimental data. They demonstrated that the origin of the exchange biasing mechanism is the uncompensated interfacial AFM spins in polycrystalline films with grain boundaries and interfacial roughness.

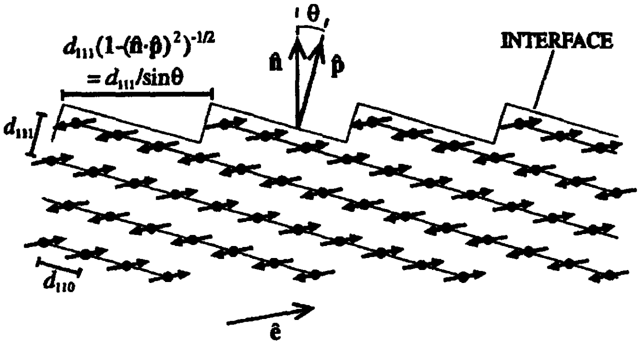

Figure 1.9 Schematic of interface cross section of exchange-biased structure in Takano's model [82].

1.3.7 Metallic AFM thin film materials

Though almost all of the current applications of exchange biased film structures use metallic AFMs, there is less understanding of the basic phenomena related to metallic AFMs compared with oxide AFMs. Investigating basic properties of metallic AFMs is complicated because the crystal structures of metallic AFMs deviate more easily from cubic symmetry than do the structures of oxide AFMs. In addition, field cooling of metallic AFMs is risky since irreversible structural changes such as grain growth and inter-diffusion take place easily during the procedure.

Most work has been done in Mn alloys, such as Fe-Mn, Ni-Mn, Ir-Mn, Pt-Mn, and Rh-Mn. Table 1.1 shows the exchange field, blocking temperature, minimum thickness, and corrosion resistance of the Mn alloys coupled with 250 Å thick NiFe layer. The blocking temperature, above which the AFM anisotropy disappears, represents thermal stability of the AFM. The minimum thickness denotes the AFM thickness, which is required to obtain a saturated exchange field value.

Material	H_{eb} (Oe)	H_C (Oe)	t_{min} (Å)	T_B (°C)	Corrosion Resistance
NiFe / NiMn	185	136	300	240	Good
NiFe / FeMn	35	3	75	165	Poor
NiFe / IrMn	60	8	75	250	Moderate

Table 1.1 The exchange fields, blocking temperatures, minimum thicknesses, and corrosion resistance of the Mn alloy AFMs coupled with 250 Å thick NiFe layer [83].

Fe-Mn is one of the most studied AFM materials. The fcc γ-phase of Fe-Mn alloy is antiferromagnetic, and this phase extends from about 30 to 55 at% Mn at room temperature [84]. The Mn and Fe atoms occupy the lattice sites randomly. The atoms at the (0,0,0), (0, ½, ½), (½, 0, ½), and (½,½, 0) form a tetrahedron, and the spins on these atoms are directed along the four <111> directions towards the center of this tetrahedron.

Ni-Mn alloy has higher T_B and much better corrosion resistance compared with Fe-Mn. The ordered FCT Θ-phase of Ni-Mn extends from 43 to 53 at% Mn. The Mn atoms, with moments $\approx 3.8\ \mu_B$, and the Ni atoms, with virtually no moment ($< 0.2\ \mu_B$), are alternately placed in (002) planes. The nearest-neighbor Mn atoms are coupled antiferromagnetically, with the next-nearest-neighbors ferromagnetically. Annealed Ni-Mn shows higher H_{eb} than Fe-Mn. However, while Fe-Mn film usually has antiferromagnetic phase as deposited, Ni-Mn requires high temperature annealing to form the AFM FCT phase [83]. Ni-Mn also has much higher minimum thickness than Fe-Mn.

Ir-Mn has an AFM fcc γ-phase, in which spins on each (002) plane are aligned parallel along the c-axis with alternating signs on neighboring (002) planes [85]. Ir-Mn AFM films have many superior properties [83, 86]. They have AFM phase as deposited, high interfacial exchange energy, decent corrosion resistance, and, especially, very low minimum thickness.

1.3.8 Magnetic properties of exchange coupled thin film structures

1.3.8.1 Thickness dependence

The exchange bias field is inversely proportional to the FM thickness (Fig. 1.10(a)).

$$H_{eb} \propto \frac{1}{t_F}$$

This relationship indicates that exchange bias is an interface effect.

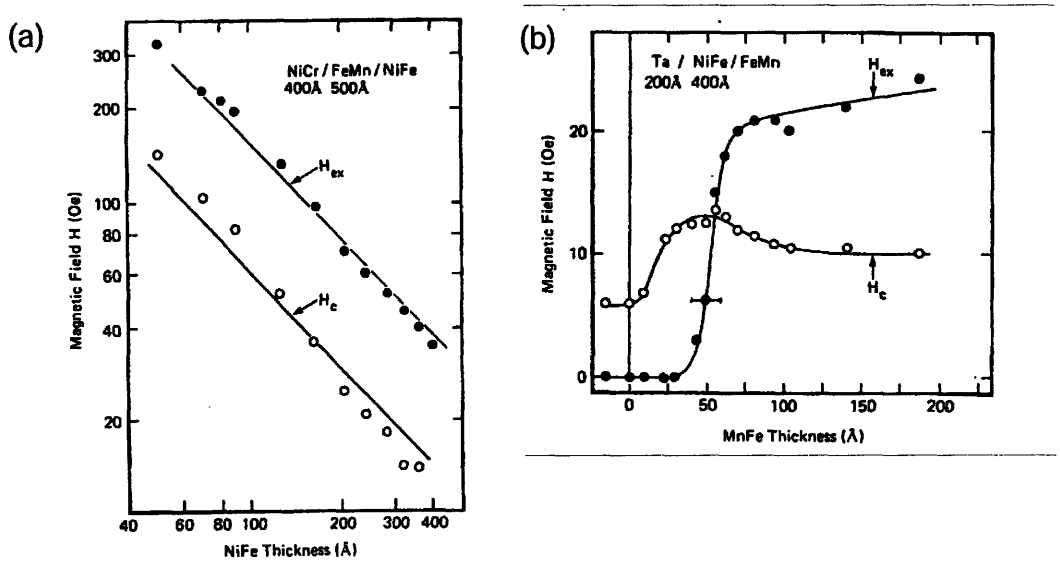

Figure 1.10 Thickness dependence on exchange bias of FM layer thickness (a), and of AFM layer thickness (b) [87].

The dependence of H_{eb} on the AFM thickness is shown in Figure 1.10(b). No exchange bias appears when the AFM is so thin that it cannot satisfy $K_{AF}t_{AF} \geq J_{INT}$ (Eq. 1.4), which is presented in Meiklejohn and Bean's model. However, the AFM thickness dependence of exchange bias is not usually as simple as the model suggests because thickness can affect the anisotropy energy K_{AF}, the blocking temperature T_B, and the microstructures of the FM-AFM system.

1.3.8.2 Effect of roughness

The role of roughness on the exchange bias remains unclear. Most investigations show that the magnitude of exchange bias decreases with increasing roughness [77, 88, 89] (Fig. 1.11(a)), while some indicates that it increases with increasing roughness [90] (Fig. 1.11(b)). This behavior appears to be independent of the interface spin structures, i.e. compensated or uncompensated. Roughness may affect the interface coupling J_{INT} or AFM domains.

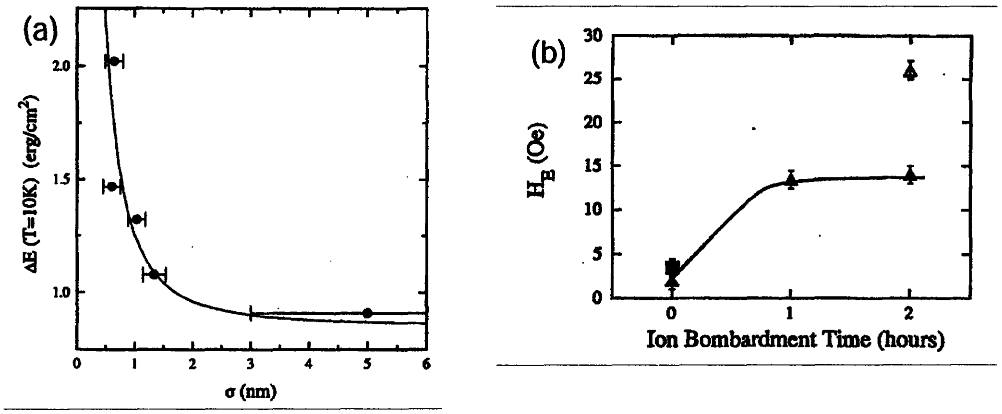

Figure 1.11 (a): Interface energy $\Delta E = M_F t_F H_{eb}$ vs. Fe-FeF$_2$ interface roughness σ obtained from grazing x-ray diffraction. ΔE is inversely proportional to σ [88]. (b): exchange field vs. ion bombardment time of NiFe / CoO, which indicates that exchange bias increases as the roughness of the sample increases [90].

1.3.8.3 Effect of impurities

Generally the presence of impurity layers (amorphous or oxidized layers and C, H or H_2O) at the interface tends to decrease the magnitude of exchange bias [91] (Fig. 1.12). Gökemeijer et el. carried out an interesting study about a metal layer inserted between the FM and AFM [92]. They found that the exchange bias decreases with the presence of the metal layer, but does not disappear until the thickness of the metal layer reaches several nm.

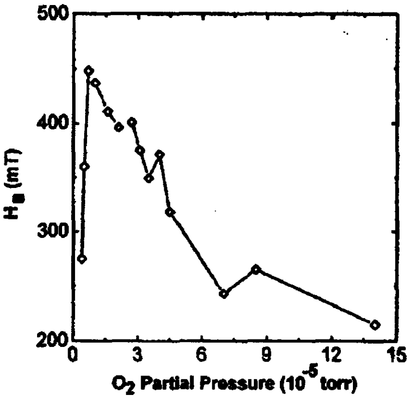

Figure 1.12 Effect of p(O_2) on the pinning strength, H_B, in NiO / Co / Cu based spin valves. The graph shows that the interface disorder caused at high p(O_2) deteriorates the exchange bias [91].

1.3.8.4 Effect of crystallinity

The degree of texture i.e. crystallinity of an AFM layer may affect the exchange bias. The crystallinity can be determined using X-ray diffraction [93]. Generally exchange bias increases as the texture increases (Fig. 1.13). Less crystallinity allows the grains to have a wider range of AFM / FM coupling angles, which results in a change in long-range AFM properties such as antiferromagnetic domains and anisotropies.

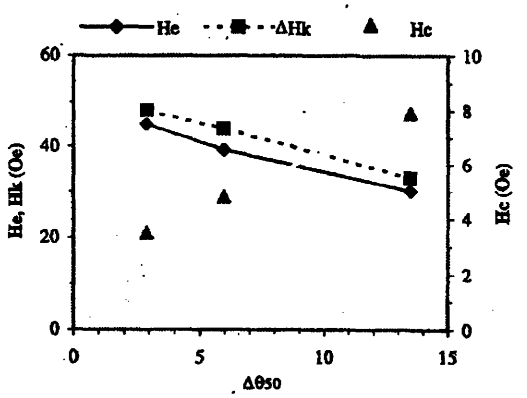

Figure 1.13 Exchange bias field H_e, coercivity H_c, and the anisotropy field H_k vs. preferred crystal orientation distribution ($\Delta\theta_{50}$) of FeMn / NiFe bilayers [93].

1.4 Magnetoresistance (MR)

In a thin film magnetic structure, the electrical resistance changes depending on the direction of magnetization. The magnitude of the relative resistance change is referred to as the magnetetoresistance (MR), which is defined as

$$MR = (R_m - R_0) / R_0$$

where R_m and R_o represent the highest and lowest resistance of the structure respectively. There are three types of magnetoresistance, the anisotropic magnetoresistance (AMR), the giant magnetoresistance (GMR), and the spin dependent tunneling (SDT).

1.4.1 AMR

In any materials, the resistance varies in the presence of an external field due to the Hall effect. The charge carriers are deflected from the current direction by the magnetic field. In magnetic materials the internal magnetic field, which is generally much stronger than the external field, enhances the magnitude of the resistance change. Since the resistance changes depend on the angle between the magnetization direction and the current direction, it is called the anisotropic magnetoresistance (AMR).

In a uniaxial single domain particle when a field is applied at the angle θ with respect to the current direction the AMR is described as

$$AMR = \frac{3}{2}\frac{R_{//} - R_{\perp}}{R_{\perp}}(\cos^2\theta - \frac{1}{3})$$

$R_{//}$ and $R_{\perp}$ are the resistance when the current is parallel and perpendicular to the magnetization direction, respectively. Usually the $R_{//}$ is the highest and $R_{\perp}$ is the lowest resistance.

1.4.2 GMR

In 1988, Baibich et al. [1] reported a 50% MR at 4.2 K in $(Fe/Cr)_n$ multilayer structures where a 3-6 nm thick Fe / 2-3 nm Cr bilayer stack is repeated n times. This MR was an order of magnitude higher than the largest MR value known to that time and was referred to as the giant magnetoresistance (GMR). Unlike AMR, GMR shows no dependency on the current direction relative to the magnetization direction. It is determined by the relative magnetization configuration of the two neighboring FM layers separated by a non-magnetic metal spacer. In the $(Fe/Cr)_n$ multilayer the Fe layers are magnetized in an antiparallel configuration throughout the structure at remanence. As a field is applied and the magnetization directions of the Fe layers start pointing the same direction the resistance is reduced by 50%. A parallel configuration of the magnetization of such multilayer structures results in a lower electric resistance. As θ is the angle between the magnetization directions of the two ferromagnetic layers, the GMR can be described as below.

$$GMR = \frac{R_a - R_p}{R_p}\frac{(1-\cos\theta)}{2}$$

where R_a and R_p are the resistances when the magnetization configuration is antiparallel and parallel, respectively. The mechanism of GMR can be understood in terms of the spin dependent scattering, which is more likely to occur when the spins of the carrier and the scattering site are opposite to each other. Spin dependent scattering occurs mostly at the interfaces between individual layers ("Interface" effect) rather than within the layers ("bulk" effect) [4].

1.4.3 GMR structures

1.4.3.1 Spin valve

GMR structures consisting of multiple ferromagnetic layer and spacer couples are not useful for applications in magnetoelectric devices since switching of such structures require a large field, typically above 10 kOe, due to strong coupling between the adjacent ferromagnetic layers. GMR can be obtained at low fields by using spin valve structures. The spin valve structure [7] has two ferromagnetic layer separated by a non magnetic metal layer (usually Cu). One of the ferromagnetic layers is in contact with an antiferromagnetic layer, which pins the FM layer by exchange coupling. The other FM layer is free so that it can switch with the application of a relatively low magnetic field. This makes spin valves an excellent magnetic sensor, which enables electrical detection of small amount of change in magnetic fields. It is widely used in read heads in computer hard disk drives and also can function as a hysteretic memory device.

1.4.3.2 Pseudo spin valve

The pseudo spin valve structure is the same as the spin valve structure except for the absence of the AFM layer. There are two FM layers usually of different materials. One is made of a magnetically hard material, which switches at a relatively high field, and the other is made of magnetically soft material switching at a smaller field. The difference in the switching fields allows the magnetization of each FM layer in a PSV structure to be modified separately, therefore controlling the MR of the structure. PSVs and SVs find uses in magnetic memory devices such as the magnetic random access memory (MRAM).

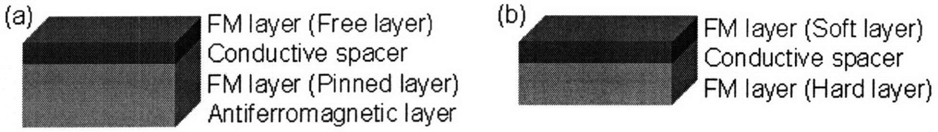

Figure 1.14 Thin film structures of the spin valve (a) and the pseudo spin valve (b).

1.4.4 Spin dependent tunneling

Good quality GMR structures show a maximum MR of 10 – 15% at room temperature, which is not enough for many applications in magnetic memory devices. Instead, MRAM devices are now made using magnetic tunnel junctions (MTJs). Instead of the diffusive scattering in GMR structures, MTJ structures implement spin dependent tunneling, which can lead to much higher MR with appropriate engineering and preparation of the materials. The MTJ structure is basically the same as the spin valve but a very thin (~ 2 – 3 nm) oxide layer is inserted instead of the non-magnetic metal spacer. Moodera et al. [94] reported > 10% MR at room temperature using an amorphous Al_2O_3 layer as a tunnel barrier. Recently several hundreds percent of MR have been reported in the MTJ structures with a MgO tunnel barrier [95, 96].

1.5 Contents

This thesis concerns ring-shaped multilayered structures such as exchange-biased rings or spin valve rings. The following chapters present fabrication, modeling, and characterization of such ring structures.

Chapter 2 covers experimental methods. Thin films were deposited using dc-triode sputtering or ion beam sputtering. Zone-plate-array lithography (ZPAL) or electron-beam lithography was used to define ring structures. An undercut profile created in a bilayer resist allowed successful liftoff of sputtered metal. The magnetic properties of the rings were measured by using alternative gradient magnetometer (AGM) and magnetic force microscope (MFM). Micromagnetic modeling was carried out using OOMMF software. The properties of unpatterned exchange biased films and spin valve films, from which the ring structures are made, are presented in Chapter 3. Exchange bias dependence on film thicknesses, field cooling, and layer sequence is described. Hysteresis loops and magnetoresistance (MR) measurements of pseudo spin valve (PSV) and spin valve (SV) films are also presented. In Chapter 4, magnetic states and magnetization reversal of sing-layer and exchange-biased elliptical rings were investigated. Angular hysteresis measurements carried out on arrays of exchange biased elliptical rings show that the formation of the vortex state is strongly dependent on the applied field direction and exchange biased direction with respect to the major axis of the ring. Chapter 5 demonstrates control of the vortex chirality in single-layer and exchange-biased elliptical rings. The vortex chirality of elliptical rings was predicted by an analytical model and that was confirmed by MFM measurements. A phase diagram of the vortex chirality in exchange-biased elliptical rings is presented, which was constructed by a series of calculations and measurements at different field angles and exchange bias angles relative to the major axis of the ring. Chapter 6 shows results on current-in-plane MR measurements on spin valve rings, which were carried out using four-point electric contacts and applying an external in-plane field. From those measurements, it was demonstrated that the chirality of each ferromagnetic layer in spin valve rings can be independently controlled by modifying the applied field direction and exchange bias direction with respect to the major axis. Finally, conclusions and future work are presented in Chpter 7.

Reference

[1] M. Baibich, J. Broto, A. Fert, *et al.*, Physical Review Letters 61, 2472 (1988).
[2] G. Binash, P. Grunberg, F. Saurenbach, *et al.*, Physical Review B 39, 4828 (1989).
[3] S. S. P. Parkin, Applied Physics Letters 61, 1358 (1992).
[4] S. S. P. Parkin, Physical Review Letters 71, 1641 (1993).
[5] S. S. P. Parkin, R. Bhadra, and K. P. Roche, Physical Review Letters 66, 2152 (1991).
[6] S. S. P. Parkin, Z. G. Li, and D. J. Smith, Applied Physics Letters 58, 2710 (1991).
[7] B. Dieny, V. S. Speriosu, S. S. P. Parkin, *et al.*, Physical Review B 43, 1297 (1991).
[8] H. Coufal, L. Dhar, and C. Denis Mee, MRS Bulletin 31, 374 (2006).
[9] J. G. Zhu, Y. F. Zheng, and G. A. Prinz, Journal of Applied Physics 87, 6668 (2000).
[10] B. N. Engel, J. Akerman, B. Butcher, *et al.*, IEEE Transactions on Magnetics 41, 132 (2005).
[11] W. J. Gallagher and S. S. P. Parkin, IBM Journal of Research and Development 50, 5 (2006).
[12] S. Tehrani, B. Engel, J. M. Slaughter, *et al.*, IEEE Transactions on Magnetics 36, 2752 (2000).
[13] S. Tehrani, J. M. Slaughter, E. Chen, *et al.*, IEEE Transactions on Magnetics 35, 2814 (1999).
[14] R. P. Cowburn and M. E. Welland, Science 287, 1466 (2000).
[15] A. Imre, G. Csaba, L. Ji, *et al.*, Science 311, 205 (2006).
[16] D. A. Allwood, G. Xiong, C. C. Faulkner, *et al.*, Science 309, 1688 (2005).
[17] D. A. Allwood, G. Xiong, M. D. Cooke, *et al.*, Science 296, 2003 (2002).
[18] R. Richter, L. Bar, J. Wecker, *et al.*, Applied Physics Letters 80, 1291 (2002).
[19] M. M. Miller, G. A. Prinz, S. F. Cheng, *et al.*, Applied Physics Letters 81, 2211 (2002).
[20] R. P. Cowburn, D. K. Koltsov, A. O. Adeyeye, *et al.*, Physical Review Letters 83, 1042 (1999).
[21] J. Eisenmenger, Z. P. Li, W. A. A. Macedo, *et al.*, Physical Review Letters 94, 057203 (2005).
[22] E. Girgis, R. D. Portugal, H. Loosvelt, *et al.*, Physical Review Letters 91, 187202 (2003).
[23] M. Grimsditch, P. Vavassori, V. Novosad, *et al.*, Physical Review B 65, 172419 (2002).
[24] H. Hoffmann and F. Steinbauer, Journal of Applied Physics 92, 5463 (2002).
[25] P. O. Jubert and R. Allenspach, Physical Review B 70, 144402 (2004).
[26] Z. P. Li, O. Petracic, J. Eisenmenger, *et al.*, Applied Physics Letters 86, 072501 (2005).
[27] M. Natali, A. Popa, U. Ebels, *et al.*, Journal of Applied Physics 96, 4334 (2004).

[28] E. Popova, H. Loosvelt, M. Gierlings, *et al.*, European Physical Journal B 44, 491 (2005).
[29] J. Raabe, R. Pulwey, R. Sattler, *et al.*, Journal of Applied Physics 88, 4437 (2000).
[30] M. Schneider, H. Hoffmann, and J. Zweck, Applied Physics Letters 79, 3113 (2001).
[31] T. Shinjo, T. Okuno, R. Hassdorf, *et al.*, Science 289, 930 (2000).
[32] J. Sort, A. Hoffmann, S. H. Chung, *et al.*, Physical Review Letters 95, 067201 (2005).
[33] C. A. Ross, F. J. Castano, D. Morecroft, *et al.*, Journal of Applied Physics 99, 08S501 (2006).
[34] M. Klaui, C. A. F. Vaz, L. J. Heyderman, *et al.*, Journal of Magnetism and Magnetic Materials 290, 61 (2005).
[35] M. Klaui, C. A. F. Vaz, L. Lopez-Diaz, *et al.*, Journal of Physics-Condensed Matter 15, R985 (2003).
[36] S. P. Li, W. S. Lew, J. A. C. Bland, *et al.*, Journal of Applied Physics 92, 7397 (2002).
[37] A. Libal, M. Grimsditch, V. Metlushko, *et al.*, Journal of Applied Physics 98, 083904 (2005).
[38] L. Lopez-Diaz, J. Rothman, M. Klaui, *et al.*, IEEE Transactions on Magnetics 36, 3155 (2000).
[39] L. Lopez-Diaz, J. Rothman, M. Klaui, *et al.*, Journal of Applied Physics 89, 7579 (2001).
[40] R. Nakatani, T. Yoshida, Y. Endo, *et al.*, Journal of Applied Physics 95, 6714 (2004).
[41] R. Nakatani, T. Yoshida, Y. Endo, *et al.*, Journal of Magnetism and Magnetic Materials 286, 31 (2005).
[42] J. Rothman, M. Klaui, L. Lopez-Diaz, *et al.*, Physical Review Letters 86, 1098 (2001).
[43] E. Saitoh, M. Kawabata, K. Harii, *et al.*, Journal of Applied Physics 95, 1986 (2004).
[44] C. A. F. Vaz, M. Klaui, J. A. C. Bland, *et al.*, Journal of Applied Physics 95, 6732 (2004).
[45] U. Welp, V. K. Vlasko-Vlasov, J. M. Hiller, *et al.*, Physical Review B 68, 054408 (2003).
[46] Y. G. Yoo, M. Klaui, C. A. F. Vaz, *et al.*, Applied Physics Letters 82, 2470 (2003).
[47] F. Q. Zhu, G. W. Chern, O. Tchernyshyov, *et al.*, Physical Review Letters 96, 027205 (2006).
[48] X. B. Zhu, P. Grutter, V. Metlushko, *et al.*, Journal of Applied Physics 93, 8540 (2003).
[49] F. J. Castano, C. A. Ross, A. Eilez, *et al.*, Physical Review B 69, 144421 (2004).
[50] F. J. Castano, C. A. Ross, C. Frandsen, *et al.*, Physical Review B 67, 184425 (2003).
[51] C. A. F. Vaz, C. Athanasiou, J. A. C. Bland, *et al.*, Physical Review B 73, (2006).

[52] R. D. McMichael and M. J. Donahue, IEEE Transactions on Magnetics 33, 4167 (1997).
[53] M. Klaui, C. A. F. Vaz, J. A. C. Bland, *et al.*, Applied Physics Letters 85, 5637 (2004).
[54] M. Klaui, J. Rothman, L. Lopez-Diaz, *et al.*, Applied Physics Letters 78, 3268 (2001).
[55] M. Klaui, C. A. F. Vaz, J. A. C. Bland, *et al.*, Applied Physics Letters 81, 108 (2002).
[56] P. Vavassori, R. Bovolenta, V. Metlushko, *et al.*, Journal of Applied Physics 99, 053902 (2006).
[57] W. Jung, F. J. Castano, and C. A. Ross, Physical Review Letters 97, (2006).
[58] F. J. Castano, C. A. Ross, and A. Eilez, Journal of Physics D-Applied Physics 36, 2031 (2003).
[59] W. Jung, F. J. Castano, C. A. Ross, *et al.*, Journal of Vacuum Science & Technology B 22, 3335 (2004).
[60] Z. B. Guo, Y. K. Zheng, K. B. Li, *et al.*, Journal of Applied Physics 93, 7435 (2003).
[61] Z. B. Guo, Y. K. Zheng, K. B. Li, *et al.*, Journal of Applied Physics 95, 4918 (2004).
[62] W. Jung, F. J. Castano, D. Morecroft, *et al.*, Journal of Applied Physics 97, 10K113 (2005).
[63] F. J. Castano, D. Morecroft, W. Jung, *et al.*, Physical Review Letters 95, (2005).
[64] F. J. Castano, D. Morecroft, and C. A. Ross, Physical Review B 74, (2006).
[65] T. J. Hayward, J. Llandro, R. B. Balsod, *et al.*, Applied Physics Letters 89, (2006).
[66] T. J. Hayward, J. Llandro, R. B. Balsod, *et al.*, Physical Review B 74, (2006).
[67] D. Morecroft, F. J. Castano, W. Jung, *et al.*, Applied Physics Letters 88, (2006).
[68] D. Morecroft, F. J. Castano, W. Jung, *et al.*, Journal of Applied Physics 99, (2006).
[69] N. Dao and S. L. Whittenburg, IEEE Transactions on Magnetics 39, 2525 (2003).
[70] J. Guo and M. B. A. Jalil, IEEE Transactions on Magnetics 40, 2122 (2004).
[71] R. C. O'Handley, *Modern magnetic materials,* p. 437 John Wiley & Sons, Inc. (2000).
[72] J. Nogues and I. K. Schuller, Journal of Magnetism and Magnetic Materials 192, 203 (1999).
[73] J. Nogues, J. Sort, V. Langlais, *et al.*, Physics Reports-Review Section of Physics Letters 422, 65 (2005).
[74] W. H. Meiklejohn and C. P. Bean, Physical review 102, 1413 (1956).
[75] W. H. Meiklejohn and C. P. Bean, Physical review 105, 904 (1957).
[76] R. P. Michel, A. Chaiken, C. T. Wang, *et al.*, Physical Review B 58, 8566 (1998).
[77] J. Nogues, D. Lederman, T. J. Moran, *et al.*, Applied Physics Letters 68, 3186 (1996).
[78] D. Mauri, H. C. Siegmann, P. S. Bagus, *et al.*, Journal of Applied Physics 62, 3047 (1987).
[79] A. P. Malozemoff, Journal of Applied Physics 63, 3874 (1988).
[80] N. C. Koon, Physical Review Letters 78, 4865 (1997).

[81] T. C. Schulthess and W. H. Butler, Physical Review Letters 81, 4516 (1998).

[82] K. Takano, R. H. Kodama, A. E. Berkowitz, *et al.*, Physical Review Letters 79, 1130 (1997).

[83] A. J. Devasahayam and M. H. Kryder, IEEE Transactions on Magnetics 35, 649 (1999).

[84] R. D. Hempstead, S. Krongelb, and D. A. Thompson, IEEE Transactions on Magnetics 14, 521 (1978).

[85] A. E. Berkowitz and K. Takano, Journal of Magnetism and Magnetic Materials 200, 552 (1999).

[86] H. N. Fuke, K. Saito, Y. Kamiguchi, *et al.*, Journal of Applied Physics 81, 4004 (1997).

[87] D. Mauri, E. Kay, D. Scholl, *et al.*, Journal of Applied Physics 62, 2929 (1987).

[88] D. Lederman, J. Nogues, and I. K. Schuller, Physical Review B 56, 2332 (1997).

[89] W. F. Egelhoff, P. J. Chen, C. J. Powell, *et al.*, Journal of Applied Physics 79, 2491 (1996).

[90] T. J. Moran, J. M. Gallego, and I. K. Schuller, Journal of Applied Physics 78, 1887 (1995).

[91] H. D. Chopra, B. J. Hockey, P. J. Chen, *et al.*, Journal of Applied Physics 81, 4017 (1997).

[92] N. J. Gokemeijer, T. Ambrose, and C. L. Chien, Physical Review Letters 79, 4270 (1997).

[93] G. Wang, T. Yeh, C. L. Lin, *et al.*, IEEE Transactions on Magnetics 32, 4660 (1996).

[94] J. S. Moodera, L. R. Kinder, T. M. Wong, *et al.*, Physical Review Letters 74, 3273 (1995).

[95] S. S. P. Parkin, C. Kaiser, A. Panchula, *et al.*, Nature Materials 3, 862 (2004).

[96] W. H. Butler and A. Gupta, Nature Materials 3, 845 (2004).

Chapter 2

Experimental methods

This chapter covers basic principles, background information, and detailed parameters of experimental methods that were used in this thesis. The first section describes thin film deposition and lithography techniques for fabrication of multi-layered ring structures. In the second section, magnetic characterization methods, such as alternative gradient magnetometry (AGM) and magnetic force microscopy (MFM), are described. Principles and parameters of OOMMF micromagnetic simulations are also introduced at the end of the chapter.

2.1 Fabrication

2.1.1 Film deposition

Magnetic films were prepared using an ultra high vacuum (UHV) sputter system. The pressure of the main chamber was kept below low 10^{-9} Torr while the substrates were transferred using a loadlock without breaking the vacuum. The system possesses 5 dc-triode magnetron sputtering guns and an ion beam sputtering module with 4 different target materials. Figure 2.1 shows a schematic overview of the system. A schematic illustration of the dc-triode magnetron sputter gun is provided in Fig. 2.2. Triode sputtering utilizes the biased target as a third electrode in addition to the cathode filament and anode pair to generate a plasma discharge. This triode configuration enhances the ionization of the working gas and therefore can support the discharge at lower pressure (< 1 mTorr) than conventional sputtering [1-4]. Because such a low pressure significantly reduces the chance for sputtered atoms to be scattered prior to deposition, the incident atoms have high energy and directionality. That would result in better microstructure of the film and make pattering processes such as lift-off processing much more convenient. In addition, triode sputtering offers independent control of the parameters that govern the discharge process, and film properties and microstructures can be tailored by modifying those parameters. For example, the magnetic coercivity, stress, and texture of NiFe films are dependent on the bias voltage and Ar pressure in triode sputtering [2].

The film growths were carried out with a plasma voltage of 60 V, plasma current of 2 A, and bias power of 100 W at an Ar pressure of 1 mTorr. Metal targets of 3" diameter were used including Cu, Ta, Au and various alloys such as 80Ni-20Fe (wt%), 84Co-16Fe (at%), 50Fe-50Mn (at%) and 20Ir-80Mn (at%). The growth rate of the films was determined by measuring the step height, which was created in a 30 minute long deposition with a shadow mask, using a Tencor P-10 surface profilometer. The rates were

2.07 Å/sec for Cu, 1.31 Å/sec for Ta, 5.41 Å/sec for Au, 1.25 Å/sec for NiFe, 1.29 Å/sec for CoFe, 0.26 Å/sec for FeMn, and 1.02 Å/sec for IrMn.

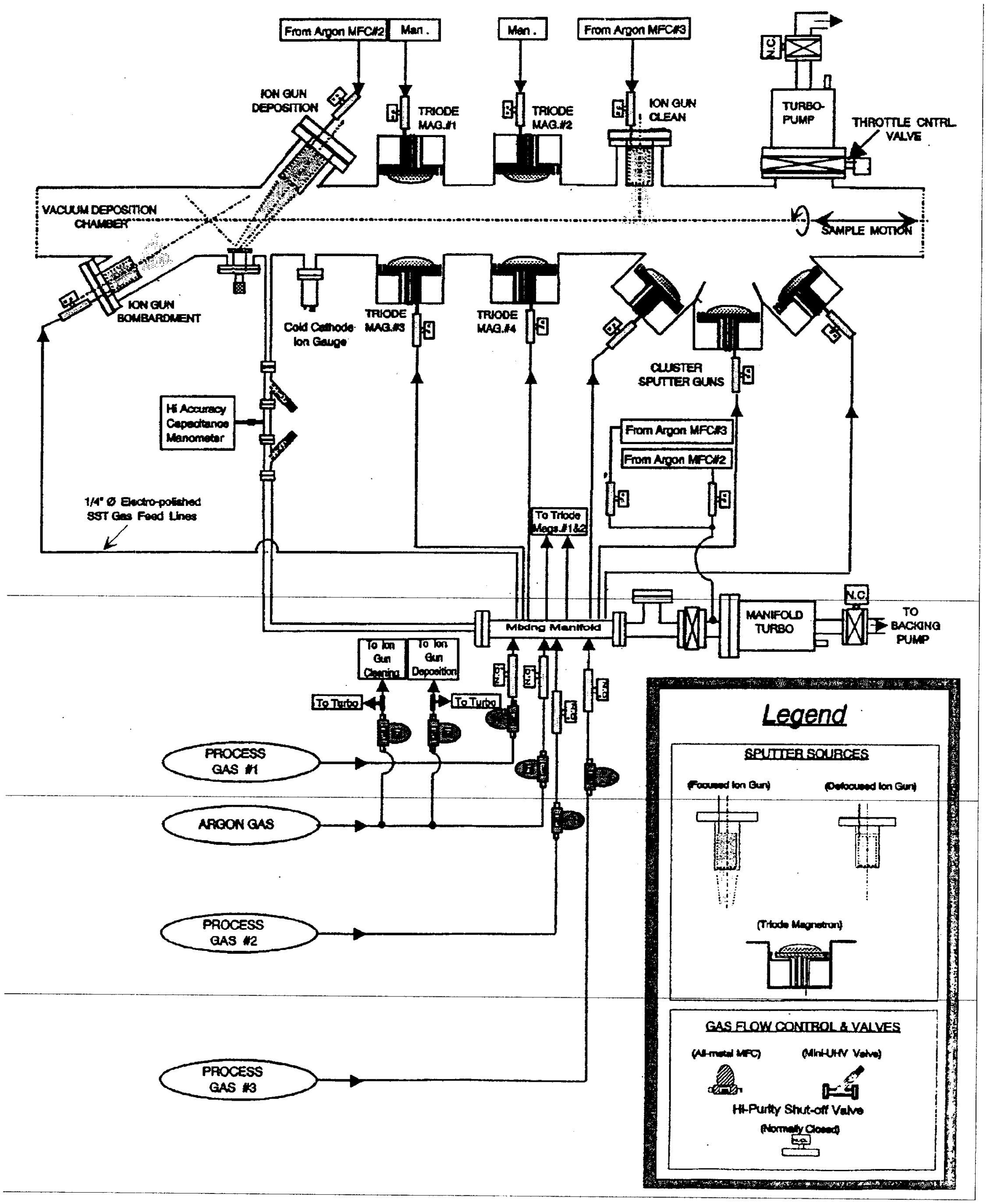

Figure 2.1 Schematic diagram of the UHV sputter system [5].

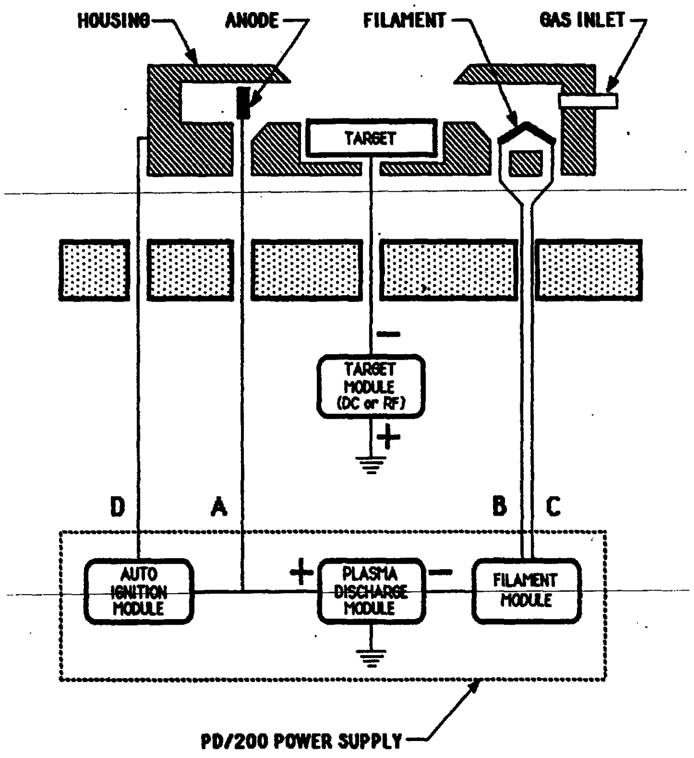

Figure 2.2 Schematic diagram of the triode sputter gun [5].

In addition to dc-triode sputtering, ion beam sputtering was used for thin film deposition. In ion beam sputtering, ions are generated in a separate ion source, extracted from the source, and driven into the target. A Kaufmann type ion source [6, 7] was used, in which electrons emitted from a thermionic cathode filament support a magnetically confined plasma discharge (Fig. 2.3). Argon is introduced as a working gas and negatively biased accelerator grids extract the argon ions out of the source. Separate generation of the ions allows the ion beam sputtering to be more controllable and the resulting films to be free from damage or contamination caused by the plasma [8-12]. Also the deposition pressure is even lower than that of the triode sputtering, which makes ion beam sputtering an excellent film deposition method for fabrication of patterned structures by lift-off.

The deposition pressure was typically 4.0×10^{-5} Torr and the Argon flow rate was 5 sccm (standard cubic centimeter per minute). A beam voltage of 1000 V and beam current of 35 mA were used. The growth rate was very low due to the low ion energy and a long distance between the target and the substrate. The rates were respectively 0.3 Å/sec for Co, 0.24 Å/sec for Ni, 0.27 Å/sec for NiFe, and 0.3 Å/sec for Cu.

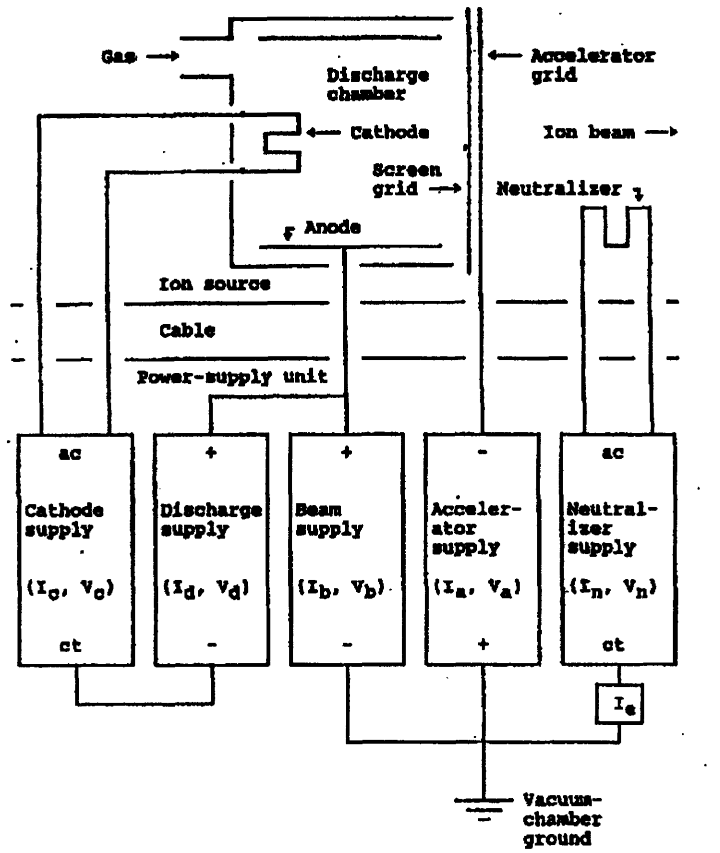

Figure 2.3 Schematic diagram of the ion gun for ion beam sputtering [5].

2.1.2 Lift-off process

The lift-off process is a method for thin film patterning in which the desired structure is created by a film deposition over a prepatterned photoresist and the subsequent removal of the photoresist (Fig. 2.4 (a)-(c)). The selected area of the photoresist (PR) is exposed and cleared prior to the film deposition. After deposition of the film, the PR is stripped off in a solvent leaving patterned film on the substrate while the film deposited on the PR is “lifted off”. The lift-off is a simple and easy patterning process compared with other processes such as ion milling or reactive ion etching (RIE). However, there is possibility for the film to be contaminated by out-gassing from the PR [13]. Also the thickness of the film is limited depending on the lateral dimension of the patterns. For a successful lift-off the deposition should have a strong directionality normal to the substrate. Otherwise materials coated on the PR sidewall lead to roughness in the edge of the patterned structures. Conventional sputtering deposition is normally too conformal for lift-off processing. In this work, however, low-pressure sputtering deposition using triode or ion beam allowed successful lift-off of the sputtered metal.

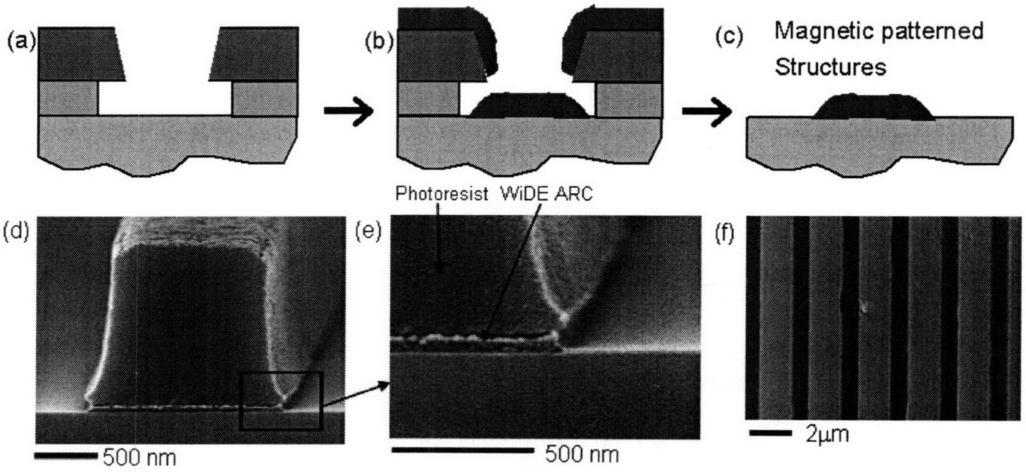

Figure 2.4 Schematic diagrams of a bilayer Lift-off process (a) – (c). Two resist layers are spincoated, exposed, and developed (a). Magnetic film is deposited (b) and patterned structures are left after removal of the resist (c). Scanning electron micrographs (SEM) of undercuts created by the bilayer process and the lift-off result (d) – (f). An undercut profile in a S1813 / WiDE ARC bilyer (d), its magnified image (e), and the lift-off result (f). The wires show clear edges.

In addition to non-conformal deposition, an undercut profile in the photoresist is desirable for lift-off processing. The undercut profile was created using a bilayer resist. For instance, a 90 nm of WiDE-antireflection coating (WiDE-ARC, Brewer Science, Inc.) and 2 μm of Shipley 1813 resist were spin coated on Si (100) wafers, and after exposure the substrates were developed in CD-26 developer (Shipley) for 150 s. The WiDE-ARC dissolves in CD-26 even without being exposed and has a broad etch rate variation depending on the baking temperature. An optimum undercut in the WiDE-ARC was obtained using a two-step prebake, one at 100 °C for 30 s, followed by another at 170 °C for 60 s. Figure 2.4 (d) and (e) show examples of the undercut profiles after development. The liftoff step was undertaken by submerging the sample in 1methyl-2pyrrolodinone (NMP) at 120 °C, followed by an ultrasonic bath.

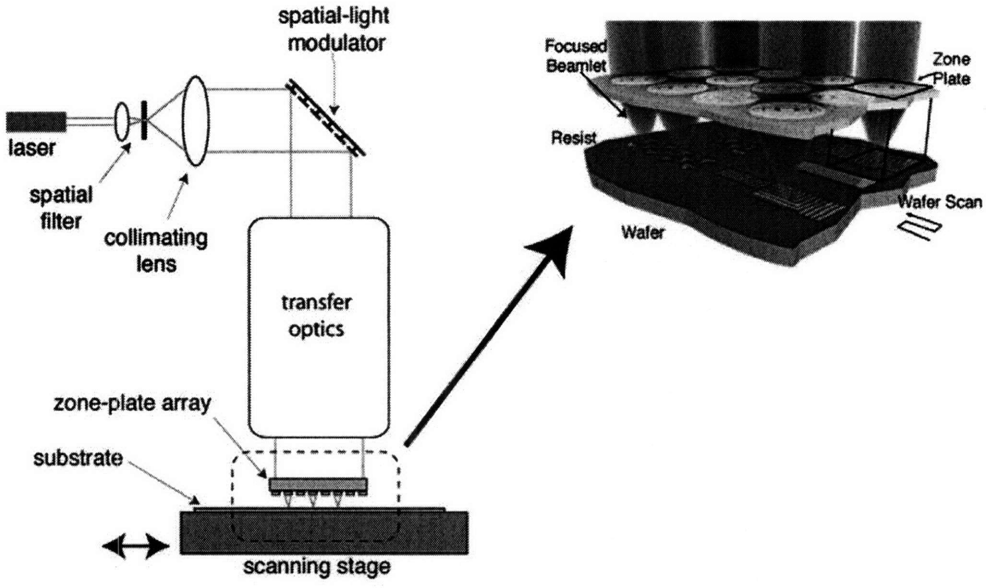

Figure 2.5 Illustration of a patterning process carried out by using the zone-plate-array lithography (ZPAL) system [14].

2.1.3 Zone-plate array lithography (ZPAL)

From the fabrication point of view, magnetic memory devices require large arrays of thin film magnets with excellent shape uniformity over the entire array. Therefore fast and inexpensive patterning techniques to fabricate these arrays are highly desirable. Zone-plate-array lithography (ZPAL) [14-19] and lift off processing were used to fabricate large arrays of thin film elliptical-ring magnets, as well as current in-plane MRAM prototypes. ZPAL is an optical-maskless lithography technique, where an array of high-numerical-aperture-diffractive lenses creates an array of tightly focused spots on the surface of a photoresist-coated substrate (Fig. 2.5). The light intensity in each spot is controlled by one pixel on a spatial-light modulator. The substrate is scanned by a high-precision stage, whereby patterns of arbitrary geometry are printed in a “dot-matrix” fashion. Since ZPAL utilizes several thousand spots in parallel, the writing speed is significantly higher than single-beam systems such as electron-beam lithography. 150 nm minimum feature size can be achieved with ZPAL operating at a wavelength of 400 nm [16].

Elliptical-ring arrays were fabricated using liftoff from ring-shaped patterns written on resist by ZPAL. An array of over 1000 zone plates with a numerical aperture of 0.7 and focal length of 40 μm was used. The exposing wavelength was 400 nm. The patterns were printed on a 90 nm WiDE-ARC / 200 nm PFI-88 (Sumitomo) bilayer resist to create an undercut profile. Magnetic thin film multilayer stacks were deposited onto these patterns by means of dc-triode magnetron sputtering. A lift-off step using hot NMP and ultrasonic bath was followed. Arrays of elliptical rings with a long axis of 3 μm, short axis of 1.7 μm, and widths of 600 nm and above were fabricated (see Fig 2.6). The arrays had a total area of 5×2.5 mm^2, containing on the order of 2×10^5 rings. These large arrays provide sufficient magnetic signals that can be measured with the sensitivity of the conventional magnetometries and polarized neutron reflection (PNR) measurement.

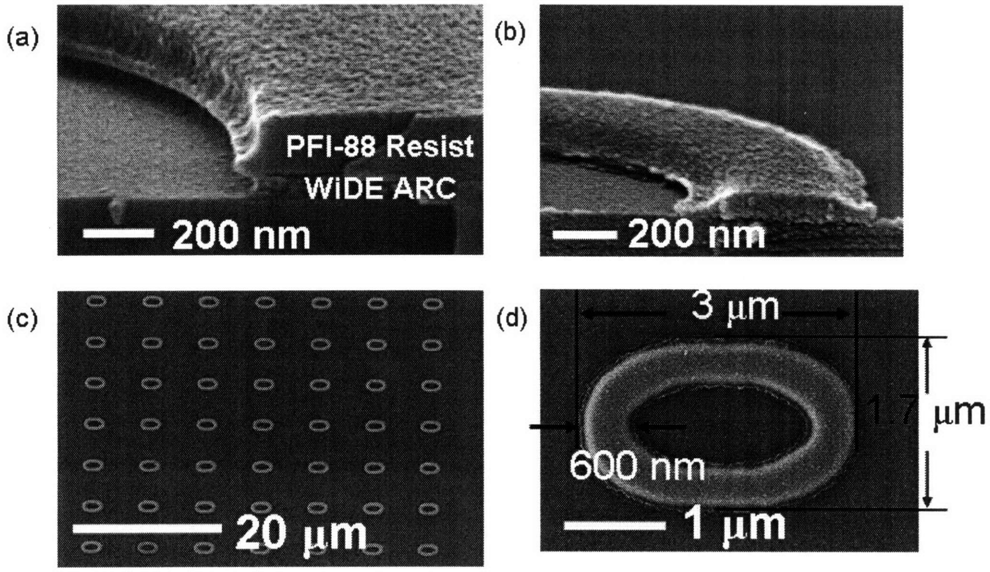

Figure 2.6 Cross-section scanning electron micrographs (SEM) of an undercut profile created using a PFI-88 / WiDE-ARC (a) and an arm of a CoFe (40 nm) / Cu (3 nm) elliptical ring structure. Plan view SEMs of a 5×2.5 mm^2 elliptical ring array created by using ZPAL (c) and an elliptical ring with long axis of 3 μm, short axis of 1.7 μm, and width of 600 nm (d).

2.1.4 Structures made by ZPAL

Fabricating contacts to rings made with ZPAL and liftoff processing entailed a two-level process requiring alignment. The substrates were 4 in. Si(100) wafers with 50 nm of thermal oxide. This oxide layer is required to isolate electrically the devices from the silicon substrate. Alignment marks, consisting of gratings of 8.33 μm period, 50 μm wide, and 200 μm long, were written in a resist layer using a VS26 electron-beam system and etched 50 nm into the thermal oxide. Three gratings were illuminated with a HeNe laser and defined to match the positions of zone plates used in the Zone-plate-array confocal microscope (ZPAM) [19]. In the alignment procedure, the gratings were scanned using the ZPAM at a step size of 60 nm to record the initial stage position relative to the zone plates. The first lithography level consisted of elliptical ring patterns and was written in a PFI-88 / WiDE-ARC bilayer. After the patterns were developed, a NiFe (6 nm) / Cu (5 nm) / CoFe (3 nm) / Cu (3 nm) multilayer PSV stack was sputter deposited followed by a liftoff step in hot NMP. To remove any residue from the WiDE-ARC, the wafer with the ring array was cleaned in a 5:1:1 H_2O:NH_4OH:H_2O_2 solution at

80 °C for 5 minutes. For the second level pattern, we scanned the marks and performed a frequency-domain analysis between the two scanned images to determine the relative spatial-phase disparity, from which we extracted the current position of the sample. From this information the appropriate alignment correction was performed before writing the second level pattern. This second layer defined the contact grid in a 200 nm thick PFI-88 resist layer. Finally a Ti (5 nm) / Au (20 nm) bilayer was electron-beam evaporated and a final liftoff in hot NMP was used to define the devices. Figure 2.7 shows scanning electron micrographs corresponding to the fabrication process of these prototypes. As reported elsewhere [19] this alignment method was satisfactory for sub-80 nm overlay, and improvement is expected when stage drift is reduced by faster scan rates.

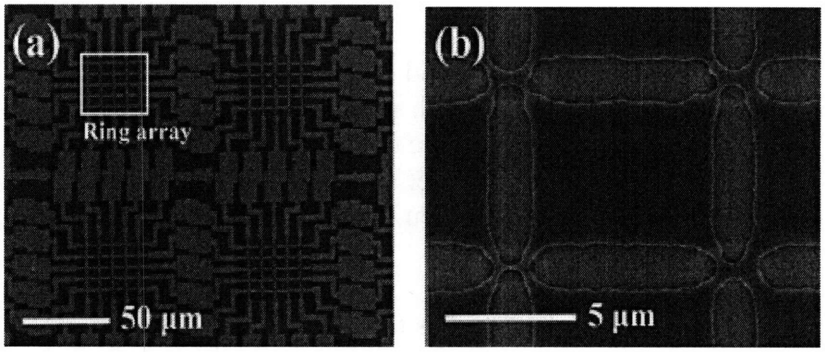

Figure 2.7 (a) Scanning electron micrographs of the multilayered elliptical ring arrays with the contact grid patterns defined in a PFI-88 resist layer. (b) Contact wire patterns with the multilayered magnetic rings underneath. The reduced thickness of the rings causes a low contrast image of their shape.

2.1.5 Electron-beam lithography

Electron-beam (e-beam) lithography (EBL) offers higher resolution than optical lithography due to the short wavelength of the electrons. It is a maskless technique so that arbitrary features in the sub-micrometer or nanometer regime can be fabricated. Since EBL pattern generation is serial, not parallel as in ZPAL, writing takes much longer. Therefore EBL was utilized for fabricating small size ring arrays with a high degree of shape variation while ZPAL was used to make large uniform arrays.

Arrays of elliptical rings with variation in the width, aspect ratio (ellipticity), and with different major axis angles were fabricated using EBL (Fig 2.8 (a)). Also pseudo spin valve (PSV) or spin valve (SV) structured ring devices with electric contacts were fabricated with a multi-level EBL process (Fig. 2.8 (b)). Poly-methylmethacrylate (PMMA) was spun on Si or oxidized Si wafer and exposed using a Raith 150 EBL system with an electron energy of 10 kV. The PMMA was developed in a 3:1 isopropanol: methylisobutylketone (IPA:MIBK) solution, and after film deposition a lift-off processing was carried out.

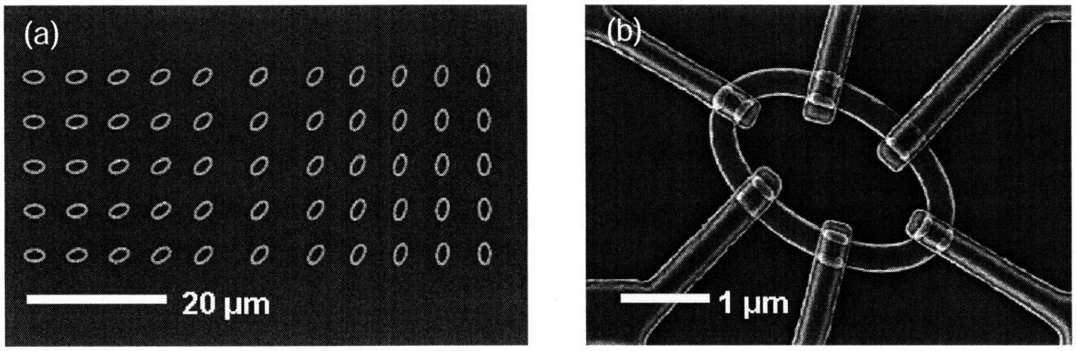

Figure 2.8 Scanning electron micrograph of an array of Co (12 nm) elliptical rings with major diameter 3.2 μm, minor diameter 2 μm, and width 400 nm (a). Rings in each column have a different major axis angle with respect to the row of the array.; (b) Conducting wires (2nm Ta / 140 nm Cu) are connected to a spin valve elliptical ring with 3.1 / 1.9 μm major / minor diameter and a 300 nm width. The film structure of the ring is Ta (5nm) / NiFe (6nm) / Cu (6nm) / Co (4nm) / IrMn (5nm) / Cu (2nm).

For most samples, the single PMMA layer was used as the resist, which results in decent lift-off of sputtered metal. Bilayer lift-off processes were also conducted. A PMMA bilayer with two different molecular weights was utilized to create undercut. A PMMA with a molecular weight of 495 kg/mol dissolves faster than 950k PMMA in the 3:1 IPA:MIBK solution. Figure 2.9(a) shows the undercut profile in the bilayer consisting of 495k / 950k PMMA. The undercut was also created by using Poly-dimethylglutarimide (PMGI) as an underlayer in a PMGI / PMMA structure [20]. PMGI dissolves in standard alkaline developers even without being exposed and the etch rate can be controlled by modifying the bake temperature. PMGI is insoluble in the organic solvents used to develop PMMA, and the PMMA is not affected by the base solvents for PMGI. This enables independent developments of the two layers and leads for the undercut profile to be created in the PMGI / PMMA bilayer. Fig 2.9(b) shows elliptical rings fabricated using the PMGI / PMMA bilayer lift-off.

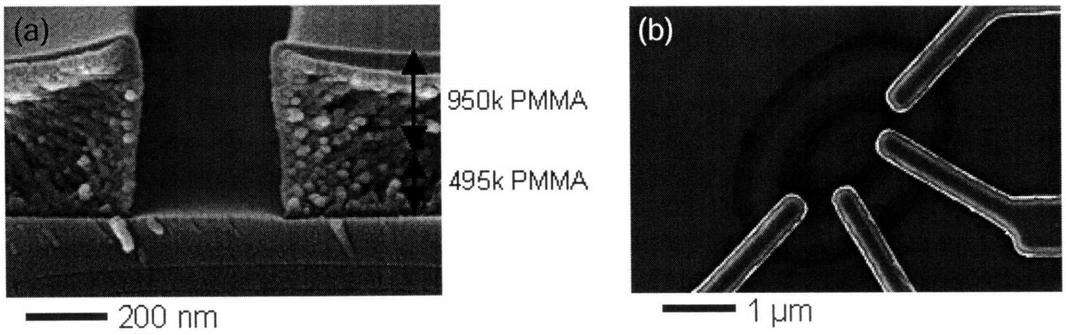

Figure 2.9 SEM picture of an undercut profile created using 495k / 950k PMMA bilayer (a).; A spin valve ring device fabricated using PMGI / PMMA bilayer lift-off (b). The side of the ring is smooth and spreads out due to the undercut.

2.2 Characterization

2.2.1 Alternating gradient magnetometer (AGM)

A Princeton Measurements Corp. MicroMag 2900 alternating gradient magnetometer (AGM) was used to measure the collective magnetic moment of small elements. In the AGM, a magnetic sample is mounted on the tip of an extension rod that incorporates a piezoelectric element (Fig. 9).

The sample is subjected to both of a static magnetic field and a small alternating field gradient. The static field magnetizes the sample and the field gradient produces a force on the sample, which is proportional to the magnetic moment of the sample. The piezoelectric elements detect the force by deflection of the extension rod. The frequency of the field gradient is tuned to the mechanical resonance frequency of the assembly. Therefore the signal can be greatly enhanced and AGM could have a very high sensitivity and signal-to-noise ratio, which allows quick measurements on low moment samples. However, AGM measurement is sensitive to acoustic noise and the sample position relative to the coils. Sometimes quantification of the magnetic moment is less reliable compared to other magnetometers such as a vibrating sample magnetometer (VSM). There is a limitation in the sample size and mass. AGM is not effective in measuring samples with a low coercivity since for such samples the magnitude of the field gradient should be reduced, which incurs reduction of the signal. The sensitivity of our system was $10^{-5} \sim 10^{-6}$ emu.

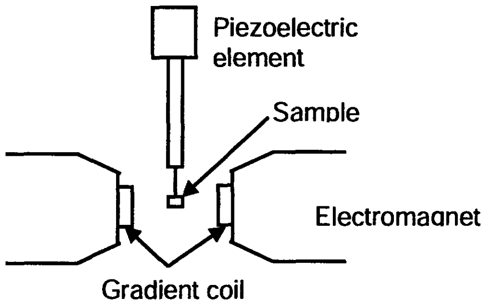

Figure 2.10 Schematic diagram of the alternating gradient magnetometer (AGM).

2.2.2 Magnetic force microscopy (MFM)

The magnetic force microscope is a variant of scanning probe microscope (SPM) that can image the spatial distribution of magnetic flux of the sample (Fig 2.11). A flexible cantilever with a sharp magnetic tip at the end is oscillated at its resonance frequency. The amplitude and frequency of the oscillation are monitored by a photodetector which detects laser beam reflected from the end of the cantilever. Magnetic interaction between the sample and the tip gives rise to a frequency shift Δf, which is proportional to vertical gradients in the magnetic forces on the tip. Detection of such shifts along with a raster scanning across the sample generates a two-dimensional magnetic image.

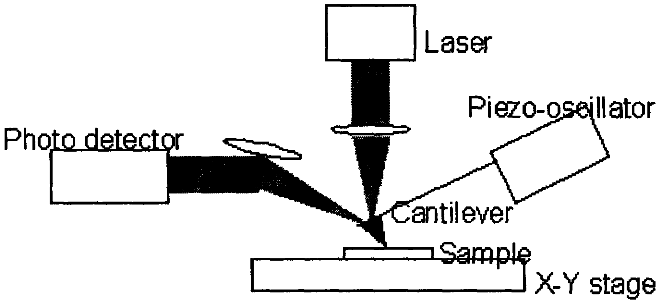

Figure 2.11 Schematic illustration of the magnetic force microscope (MFM).

MFM was carried out using a Digital Instruments 3100 SPM system in its tapping / lift mode (Fig. 2.12). In the tapping / lift mode, a sample is scanned twice. The tapping mode scan obtains topographic information of the sample using the oscillation amplitude of the tip as feedback. This information is stored and used in the following lift mode scan to provide a fixed height offset to the surface. By monitoring the frequency shift Δf, a magnetic image separated from the topography is obtained.

MFM allows the observation of the domain structures in a small magnetic element. As illustrated in Figure 2.13(a) 180° domain walls of the magnetic rings can be read from the bright or dark contrasts in the MFM image, which represent the stray fields emanating from the domain walls. The vortex state, in that sense, shows no contrast due to the absence of domain walls (Fig. 2.13(b)).

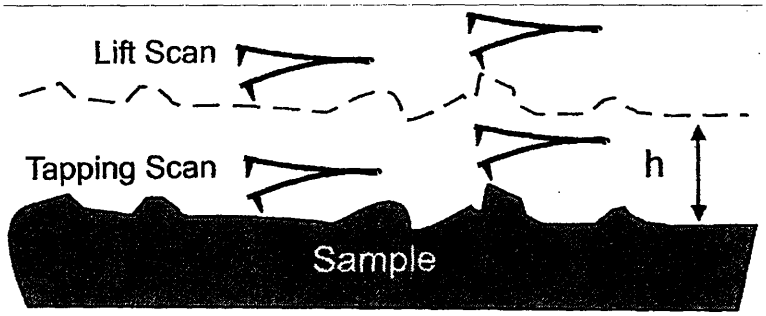

Figure 2.12 Schematic illustration of the Tapping / Lift mode. *h* denotes the lift height [21].

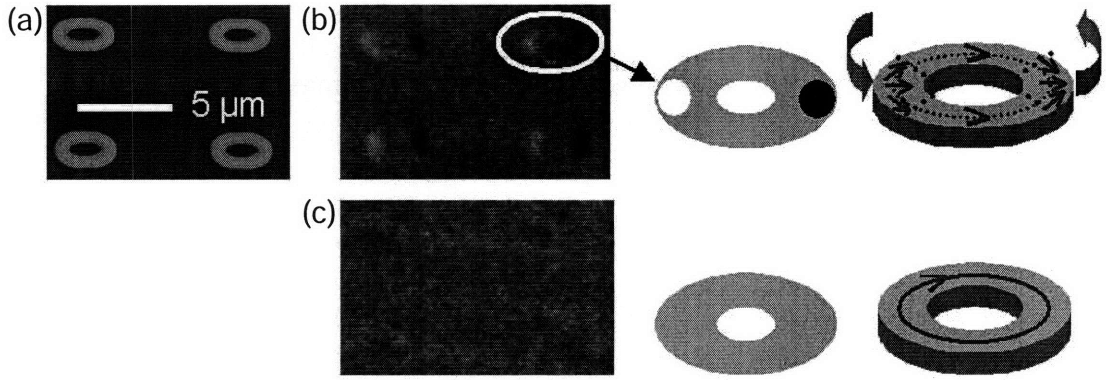

Figure 2.13 (a) Topographic image of a 20 nm NiFe elliptical ring array obtained from the tapping mode of MFM.; MFM images of the onion state (b) and the vortex state (c) of the same ring array. Schematics of the corresponding MFM contrast and magnetization configuration of the onion and vortex state are presented in the right side of each MFM image. The arrows on the ring represent magnetic moments and the wide arrows outside of the ring represent the stray fields.

2.3 Micromagnetic simulation

The configuration of the magnetic moments in a magnetic element can be calculated using micromagnetic simulations. A magnetic element is discretetized into tiny cells on nanometer length scales and the time dependent magnetization of the cells is calculated by solving the Landau-Lifshitz Gilbert (LLG) equation, which is described below.

$$\frac{dM}{dt} = -|\gamma| M \times H_{eff} + \frac{\alpha}{M_s}\left(M \times \frac{dM}{dt} \right) \qquad (2.1)$$

Here M is the magnetization, H_{eff} the effective field, γ the Landau-Lifshitz gyromagnetic ratio, and α the damping constant. The damping term eventually leads to the magnetization to be aligned along the effective field, that is, the system converges into equilibrium. The effective field is given by $H_{eff} = -\left(\delta E / \delta M \right)_T$ where the E denotes the total free energy, which includes contributions from anisotropy, exchange, magnetostatic, and applied field. Those terms are responsible for the overall behavior of a magnetic system, and, therefore, the LLG equation is capable of yielding the lowest energy magnetization configuration of the system.

Micromagnetic simulations were carried out using NIST object oriented micromagnetic framework (OOMMF) software [22]. The parameters appropriate for NiFe (exchange constant $A = 1.3 \times 10^{-11}$ J/m, saturation magnetization $M_S = 860 \times 10^3$ A/m, anisotropy constant $K_1 = 0$) and Co ($A = 3 \times 10^{-11}$ J/m, $M_S = 1400 \times 10^3$ A/m, $K_1 = 5.2 \times 10^5$ J/m^3), with a damping coefficient $\alpha = 0.5$, were used. The cell size for NiFe and Co was 10 and 5 nm, respectively, and the anisotropy direction for each cell was randomly oriented across the structure in order to simulate the polycrystalline nature of the films.

Reference

[1] A. P. M. Kentgens, A. H. Carim, and B. Dam, Journal of Crystal Growth **91**, 355 (1988).

[2] R. Minakata, IEEE Transactions on Magnetics **24**, 2020 (1988).

[3] P. Ziemann and E. Kay, Journal of Vacuum Science & Technology **21**, 828 (1982).

[4] D. S. Rickerby and A. Mattews, *Advanced surface coatings: a handbook of surface engineering,* p.101 Chapman and Hall (1991).

[5] UHV sputter deposition system operation manual, Superior Vacuum Technology, Inc.

[6] H. R. Kaufman, J. J. Cuomo, and J. M. E. Harper, Journal of Vacuum Science & Technology **21**, 725 (1982).

[7] J. M. E. Harper, J. J. Cuomo, and H. R. Kaufman, Journal of Vacuum Science & Technology **21**, 737 (1982).

[8] L. A. Stelmack, *Ion beam techniques for thin film depositon,* MIT IAP course notes (2006).

[9] W. Y. Lee, M. Carey, M. F. Toney, *et al.*, Journal of Applied Physics **89**, 6925 (2001).

[10] S. N. Mao, N. Amin, and E. Murdock, Journal of Applied Physics **83**, 6807 (1998).

[11] J. M. Slaughter, E. Y. Chen, and S. Tehrani, Journal of Applied Physics **85**, 4451 (1999).

[12] Y. Miyamoto, T. Yoshitani, S. Nakagawa, *et al.*, IEEE Transactions on Magnetics **32**, 4719 (1996).

[13] M. J. Biercuk, D. J. Monsma, C. M. Marcus, *et al.*, Applied Physics Letters **83**, 2405 (2003).

[14] D. J. D. Carter, D. Gil, R. Menon, *et al.*, Journal of Vacuum Science & Technology B **17**, 3449 (1999).

[15] D. Gil, R. Menon, D. J. D. Carter, *et al.*, Journal of Vacuum Science & Technology B **18**, 2881 (2000).

[16] D. Gil, R. Menon, and H. I. Smith, Journal of Vacuum Science & Technology B **21**, 2810 (2003).

[17] D. Gil, R. Menon, X. D. Tang, *et al.*, Journal of Vacuum Science & Technology B **20**, 2597 (2002).

[18] W. Jung, F. J. Castano, C. A. Ross, *et al.*, Journal of Vacuum Science & Technology B **22**, 3335 (2004).

[19] R. Menon, E. E. Moon, M. K. Mondol, *et al.*, Journal of Vacuum Science & Technology B **22**, 3382 (2004).

[20] B. Cord, C. Dames, and K. K. Berggren, Journal of Vacuum Science & Technology B **24**, 3139 (2006).

[21] X. B. Zhu, *Ph.D. thesis,* McGill university (2002).

[22] OOMMF is available at http://math.nist.gov.

Chapter 3

Results on unpatterned films

This thesis concerns how the magnetic multilayers, such as exchange biased structures or spin valve structures, affect characteristics of ring magnets. Therefore it is important to study magnetic multilayered structures as in thin film forms prior to the investigation of ring structures in Chapter 4 – 6. This chapter concerns the properties of unpatterned exchange biased films and spin valve films, from which the ring structures are made, in order to provide context for behavior of rings in later chapters. Exchange bias dependence on film thicknesses, field cooling, and layer sequence is described. Hysteresis loops and magnetoresistance (MR) measurements of pseudo spin valve (PSV) and spin valve (SV) films are also presented.

3.1 Exchange bias film

A series of exchange bias films were made and characterized. Deposition of the exchange bias structures was carried out while applying a field of 350 Oe in order to impose an anisotropy on the AFM along the field direction. FeMn or IrMn was employed as the antiferromagnetic material. γ-FeMn is one of the most widely used antiferromagnetic materials [1]. FeMn has relatively high Néel temperature (490 °K) [2], which means a reasonable high temperature stability, and shows quite strong exchange field even when the film is thin [1]. The film shows an exchange bias as deposited, without any further magnetic annealing. FeMn is known to show exchange bias only in fcc γ-phase with (111) crystallographic orientation. The γ-phase exists only near 50% Mn composition [3].

The properties of IrMn are overall superior to those of FeMn [4]. IrMn has strong interfacial exchange energy and a very low minimum thickness at which the exchange bias of the FM / AFM couple is saturated. The corrosion resistance is not as good as NiMn, but nevertheless better than FeMn. The blocking temperature of IrMn, above which the AFM anisotropy is lost, is known to be 500 °K [1], however, it is lower in the thin film form [5].

The exchange field H_E and coercivity H_C of the exchange bias film structures were measured from the hysteresis loops obtained using AGM as shown in Figure 3.1.

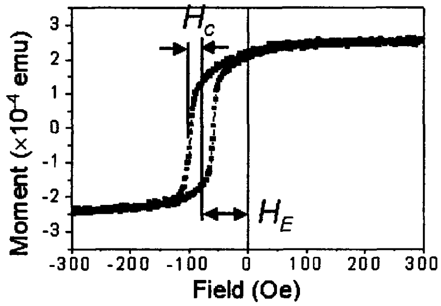

Figure 3.1 Hysteresis loop of Cu (10nm) / NiFe (5nm) / FeMn (10nm) / Cu (3nm) exchange bias film. Exchange bias H_E and coercivity H_C are 78.8 Oe and 20.6 Oe, respectively.

A series of film structures of 10 nm NiFe coupled with FeMn or IrMn of different thicknesses was deposited on a 10nm Cu under-layer. The exchange bias and coercivity of such films were shown in Figure 3.2. The exchange field is increased and saturated as the AFM thickness increases, which is consistent with the literature that was discussed in chapter 1.3.8.1.

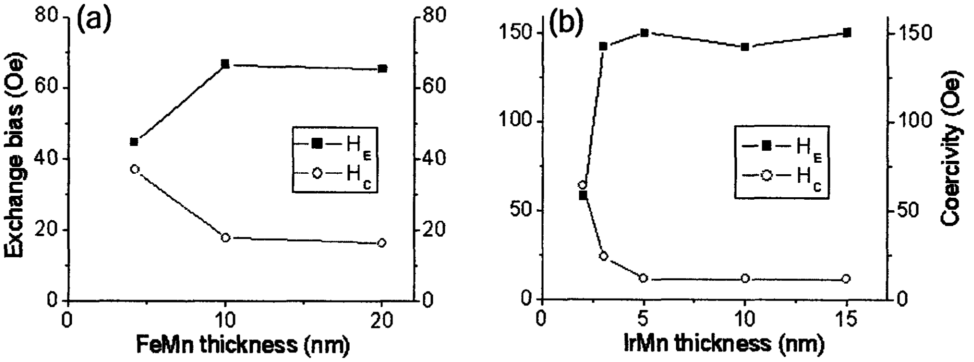

Figure 3.2 AFM thickness dependence on exchange bias and coercivity of NiFe (10nm) / FeMn (x nm) (a) and NiFe (10 nm) / IrMn (x nm) (b) exchange coupling systems.

Dependence of exchange bias H_E on the ferromagnetic layer thickness was also investigated. Figure 3.3 shows H_E and H_C of a variety of exchange bias couples such as NiFe (x nm) / FeMn (10 nm), CoFe (x nm) / FeMn (10 nm), NiFe (x nm) / IrMn (5 nm), and Co (x nm) / IrMn (5 nm). Figure 3.3 includes exchange fields of spin valve structures while most of the data belong to FM / AFM bilayers. The underlayer in the FM / AFM bilayers is Cu (10 nm) or Ta (5nm) / Cu (5nm), which behave similarly. The exchange bias decreases as the FM thickness increases, which agrees well with classical models of exchange bias (Chapter 1.3.8.1). NiFe exchange biased structures exhibit higher exchange field than CoFe or Co regardless of the AFM material, because the AFM γ-fcc phase of FeMn or IrMn tends to grow best on an fcc seed layer such as NiFe or Cu [6, 7]. Due to the strong exchange energy of IrMn, the magnitude of exchange bias in IrMn structures is higher than FeMn even with a smaller thickness.

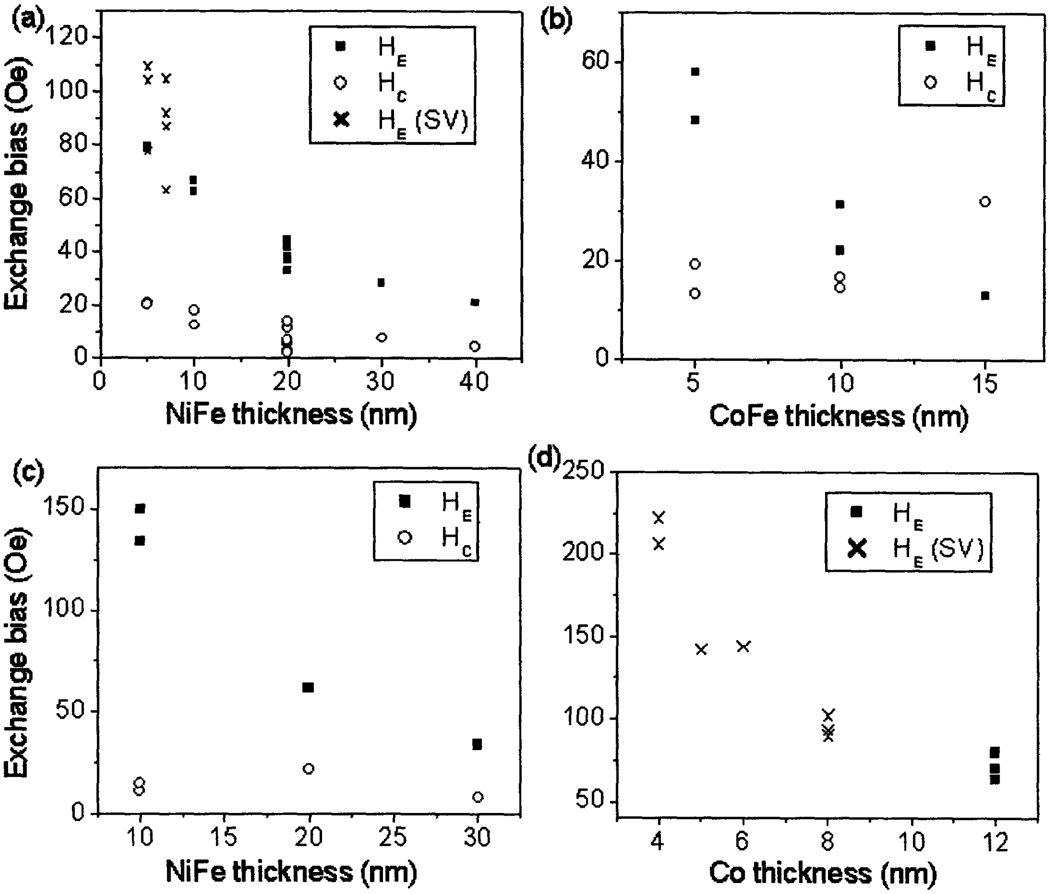

Figure 3.3 FM thickness dependence on exchange bias and coercivity in 10 nm FeMn (a), (b) and 5 nm IrMn (c), (d) exchange coupling systems. Film structures are NiFe (x nm) / FeMn (10 nm) (a), CoFe (x nm) / FeMn (10 nm) (b), NiFe (x nm) / IrMn (5nm) (c), and Co (x nm) / IrMn (5 nm).

3.2 Field cooling

The pinning direction of exchange bias structures can be modified by field cooling. Zero field cooling of an AFM layer leads to formation of AFM domains of random anisotropy orientation, which creates no net exchange pinning. However, cooling down with an applied field orients the AFM anisotropy along the field direction (Fig. 3.4).

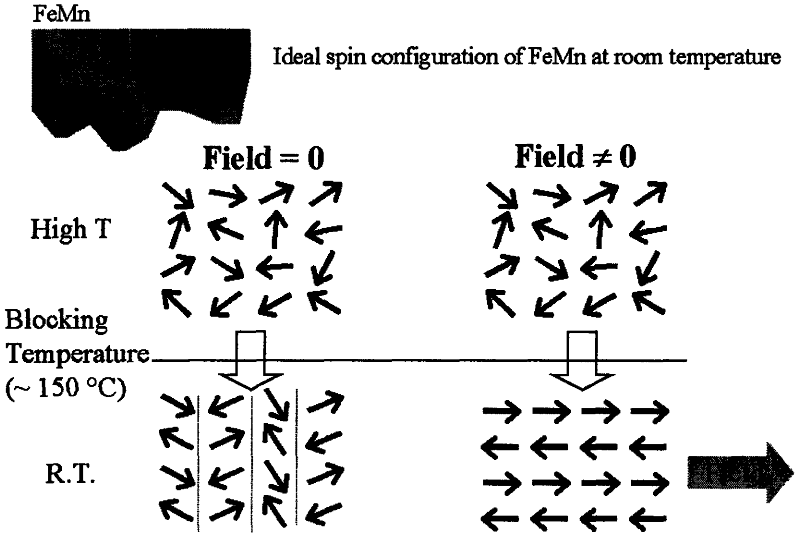

Figure 3.4 Schematic illustration of change in the spin configuration of FeMn as it goes through zero-field cooling and field cooling.

FeMn samples and IrMn samples were heated up to 160 °C and 200 °C, respectively, and cooled down as a field of 1 Tesla was applied. Figure 3.5 shows that the easy and hard magnetization direction of a spin valve film change by 90° from those as deposited, after field cooling with a field perpendicular to the initial easy axis. The magnitude of exchange bias was reduced after the field cooling from 124 Oe to 92 Oe.

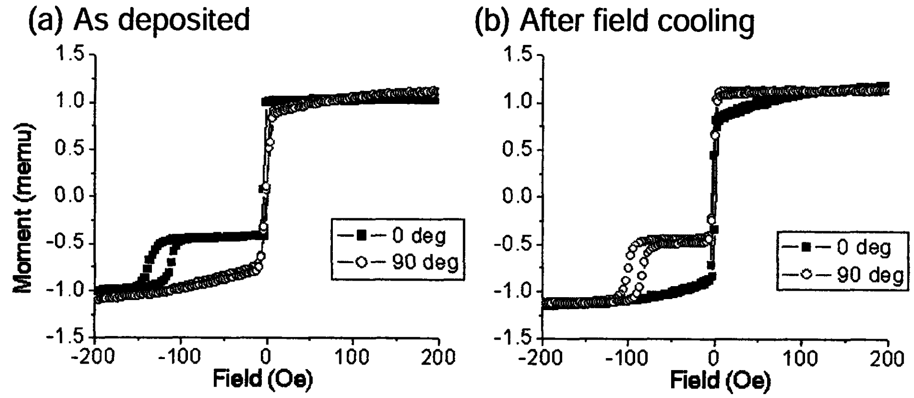

Figure 3.5 Hysteresis loops at different field angle 0° and 90° of Ta (5nm) / Cu (5) / NiFe (18) / Cu (6) / NiFe (7) / FeMn (10) / Cu (3) SV film before (a) and after field cooling (b).

Figure 3.6 shows the results of a series of field cooling on a spin valve structure with applying different magnitude of fields. After field cooling with a field of 800 Oe, the exchange bias drops from 123 Oe to 36 Oe. As the field cooling is repeated with a larger field, the bias field increases and the pinned layer switches more sharply, that is, the switching field distribution becomes smaller.

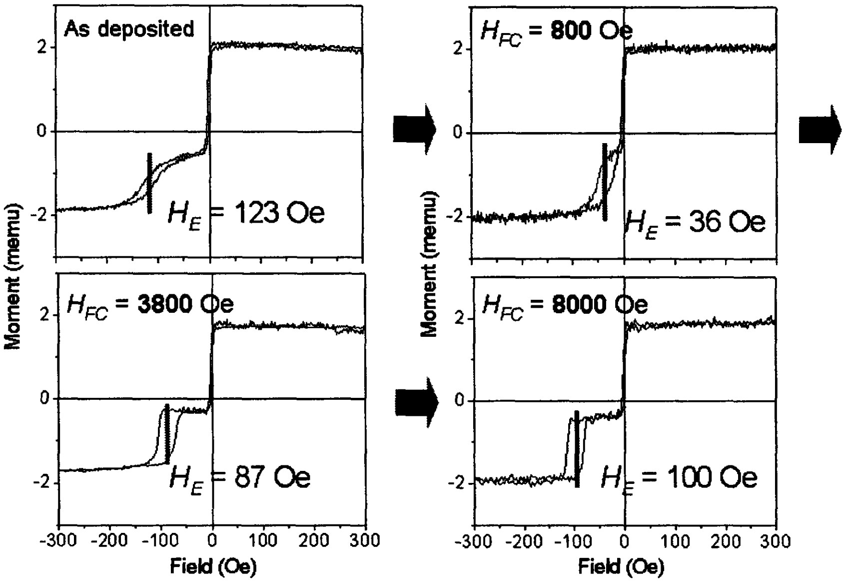

Figure 3.6 Hysteresis loop of Ta (5nm) / Cu (5) / NiFe (20) / Cu (6) / NiFe (7.1) / FeMn (10) / Cu (3) SV film after the field cooling is carried out with a different magnitude of applied field, H_{FC}. The sample was heated to 160° for 90 sec prior to each field cooling.

3.3 Layer sequence in exchange bias structures

The order of deposition influences the properties of exchange biased films. When FeMn is deposited on NiFe, a lower coercivity is obtained than when the order is reversed [6, 7]. For most of our exchange bias samples, deposition of the FM layer was carried out prior to that of the AFM. With a reversed deposition order, no exchange bias appeared unless a thick Cu seed layer is placed under the exchange bias structure (Table 3.1). FeMn / NiFe or FeMn / CoFe couples with a 50 nm thick Cu underlayer show exchange bias of less magnitude compared with the reverse order stacks of corresponding layer thicknesses. However, comparably thick Ta layers prevent exchange coupling. An IrMn / NiFe sample having a 30 nm thick Cu underlayer shows exchange bias, and it was enhanced after field cooling.

Film structure	H_E (Oe)	H_C (Oe)
Cu (50 nm) / FeMn (10) / CoFe (5) / Cu (3)	34	84
Cu (50) / FeMn (10) / NiFe (20) / Cu (3)	12	4
Ta (40) / FeMn (10) / NiFe (5) / Cu (3)	No exchange bias	
Ta (50) / FeMn (10) / NiFe (5) / Cu (3)	No exchange bias	
Ta (5) / Cu (30) / IrMn (5) / NiFe (10) / Cu (2)	28 (68)*	10 (13)*

( )*: H_E and H_C after field cooling.

Table 3.1 Exchange bias H_E and coercivity H_C of the film structures with the AFM layer placed under the FM layer.

Figure 3.7 shows the x-ray diffraction pattern of two exchange bias films deposited with reverse orders, Sample 1: Cu (50 nm) / FeMn (10) / NiFe (20) / Cu (3) and Sample 2: Ta (50 nm) / FeMn (10) / NiFe (5) / Cu (3). The x-ray diffraction (XRD) was carried out using Rigaku RU300 x-ray diffractometer with a Cu $K\alpha$ (λ = 1.542Å) source. Since the lattice constant of fcc FeMn (a = 3.63 Å), NiFe (3.55 Å), and Cu (3.61 Å) are very close to each other, the γ FeMn grows coherently on the top of fcc Cu or NiFe. The XRD pattern of Sample 1 shows much stronger fcc texture than that of Sample 2, where the peak intensity mostly originates from the Cu underlayer. The presence of such fcc (111) Cu promotes formation of AFM γ phase in FeMn in Sample 1, which gives rise to the exchange bias.

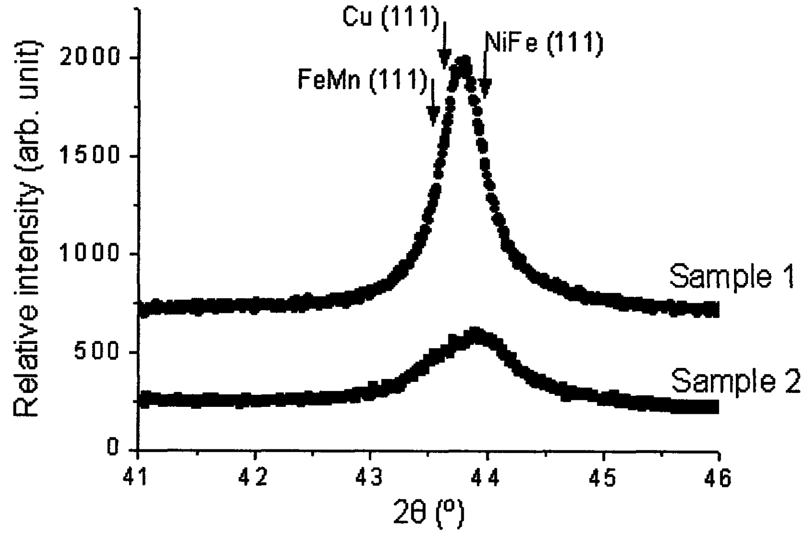

Figure 3.7 XRD patterns of FeMn / NiFe exchange couples with different seed layer materials. Sample 1: Cu (50 nm) / FeMn (10) / NiFe (20) / Cu (3) and Sample 2: Ta (50 nm) / FeMn (10) / NiFe (5) / Cu (3).

3.4 Pseudo spin valve and spin valve film

Pseudo spin valve (PSV) is a multilayer thin film structure that consists of a non-magnetic metal spacer sandwiched by two ferromagnetic (FM) layers, one is magnetically hard and the other is magnetically soft. It shows giant magnetoresistance (GMR) depending on the relative magnetization direction of FM layers.

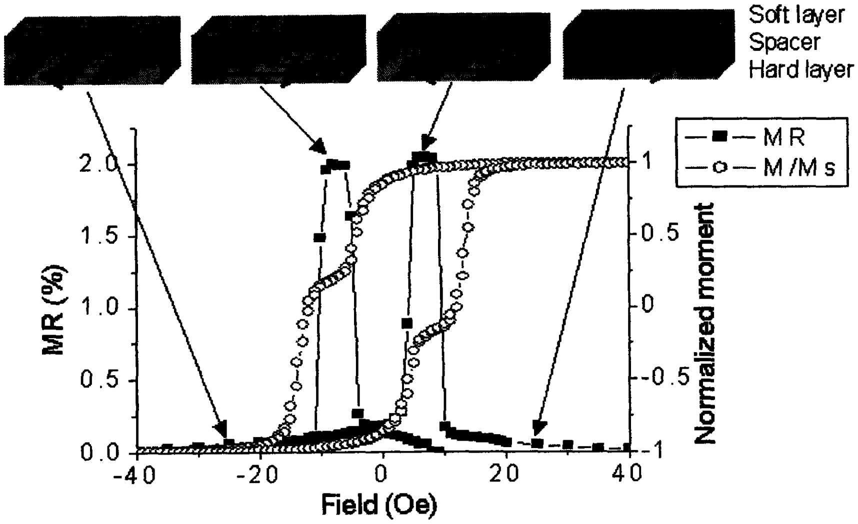

Figure 3.8 Hysteresis and MR curve of NiFe (53 Å) / Co (7 Å) / Cu (60 Å) / Co (7 Å) / CoFe (48 Å) / Cu (40 Å) pseudo spin valve thin film structure. The magnetization configurations corresponding to each MR state are illustrated on the top.

A series of pseudo spin valve (PSV) films were deposited by dc-triode magnetron sputtering, and their hysteresis loop and magnetoresistance (MR) were measured using the alternating gradient magnetometer (AGM) and a conventional four point probe setup. For the MR measurement, the film structure was electrically isolated from the wafer by employing an oxidized Si wafer as a substrate. In the PSV structures, when the magnetization directions of neighboring ferromagnetic layers are parallel, the film shows lower resistance than when they are anti-parallel (Fig. 3.8). Figure 3.8 shows that the MR characteristic of a film structure is intimately related to its switching behavior.

Figure 3.9 displays the hysteresis and MR curves of two different film structures with different Cu thicknesses while the thicknesses of all other layers are the same. The change in the Cu thickness affects the MR and switching behavior of the PSV films. A thicker Cu spacer results in a smaller maximum MR because more current is shunted through the Cu layer. Also the switching field difference between the soft and hard layer, i.e. the width of the plateau in the loop, is decreased as the Cu thickness is decreased due to the enhanced exchange coupling between the two layers. Most of the pseudo spin valve films show a reasonable GMR of over 1 %. In order to increase the GMR of samples, more complicated structures, such as NiFe (53 Å) / Co (7 Å) / Cu (60 Å) / Co (7 Å) / CoFe (48 Å) / Cu (40 Å), were made on a pre-annealed substrate, which result in maximum MR higher than 2 % (Fig 3.8). It has been reported that insertion of a thin Co layer between the ferromagnetic layer and the spacer enhances GMR in the spin valve structures [8].

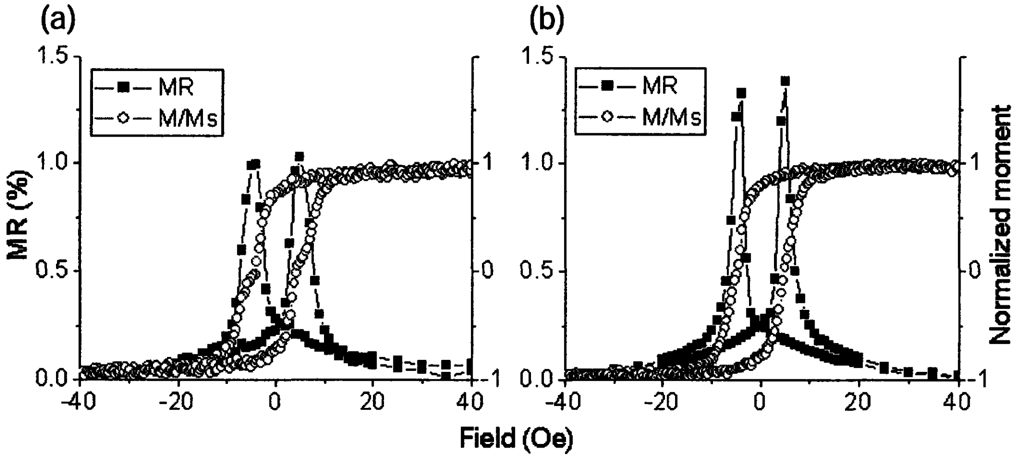

Figure 3.9 Hysteresis loop and MR curve of NiFe (60 Å) / Cu (60 Å) / CoFe (30 Å) / Cu (40 Å) PSV film (a) and NiFe (60 Å) / Cu (40 Å) / CoFe (30 Å) / Cu (40 Å) (b). The maximum MR value of the films is 1.03% and 1.39%, respectively.

Spin valve films were also deposited, and the hysteresis and MR of the films were measured (see an example in Fig 3.10). The spin valve has the same structure as the pseudo spin valve, but one of the ferromagnetic layer is pinned by exchange coupling with an antiferromagnetic (AFM) layer. Switching of the pinned layer takes place in a higher field range separated from that of the free layer.

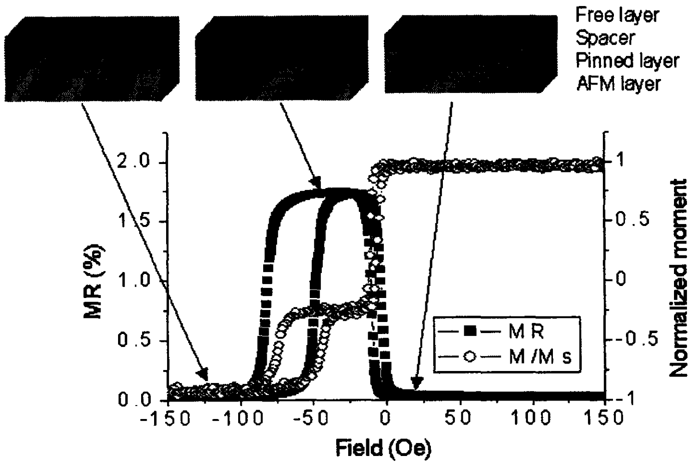

Figure 3.10 Hysteresis loop and MR curve of a spin valve structure, Si / SiO$_2$ / Cu (50 Å) / NiFe (100 Å) / Cu (30 Å) / NiFe (50 Å) / FeMn (100 Å) / Cu (30 Å). The maximum MR is 1.74%

3.5 Conclusions

Exchange-biased films exhibited shifted hysteresis loops, and the magnitude of the shift, which corresponds to the exchange bias, was determined by materials and layer thicknesses. Generally the exchange bias was inversely proportional to the ferromagnetic (FM) layer thickness. The bias direction was tailored by applying an in-situ field during film deposition or by field cooling carried out after the deposition. In FeMn / NiFe bilayers, no exchange bias appeared without an underlayer that promotes formation of AFM γ phase in FeMn. Magnetization reversal of pseudo spin valve films and spin valve films was affected by layer thicknesses and MR measurements of the films showed strong dependence of MR on the magnetization states of the FM layers in spin valve structures.

Reference

[1] M. Lederman, IEEE Transactions on Magnetics **35**, 794 (1999).

[2] J. Nogues and I. K. Schuller, Journal of Magnetism and Magnetic Materials **192**, 203 (1999).

[3] A. E. Berkowitz and K. Takano, Journal of Magnetism and Magnetic Materials **200**, 552 (1999).

[4] A. J. Devasahayam and M. H. Kryder, IEEE Transactions on Magnetics **35**, 649 (1999).

[5] J. Sort, K. S. Buchanan, V. Novosad, *et al.*, Physical Review Letters **97**, 067201 (2006).

[6] R. D. Hempstead, S. Krongelb, and D. A. Thompson, IEEE Transactions on Magnetics **14**, 521 (1978).

[7] K. T. Y. Kung, L. K. Louie, and G. L. Gorman, Journal of Applied Physics **69**, 5634 (1991).

[8] S. S. P. Parkin, Applied Physics Letters **61**, 1358 (1992).

Chapter 4

Results on single-layer and exchange-biased elliptical rings

4.1 Introduction

Arrays of lithographically defined small magnetic thin film elements have received considerable attention during the last decade due to their application in nonvolatile magnetic random access memories (MRAMs) [1] as well as other magnetoelectronic device [2]. MRAM devices consist of an array of multilayered thin film magnets that are connected with conductor lines. Each magnet stores one bit of information and should exhibit at least two different magnetic states which are assigned as "0" or "1". Most MRAM prototypes rely on tapered elongated magnets fabricated from multilayered thin film structures. Recently, ring-shaped magnetic elements [3-5] have been proposed as an alternative to achieve high-density MRAMs. Among the advantages of ring shaped magnets are the existence of several different stable magnetic states [6,7], which could allow for more than one bit to be stored in each element.

For device applications, consistent and controlled magnetization switching is desirable, and, therefore, it is important to explore the magnetization reversal of magnetic ring structures and understand the physics behind it.

A considerable amount of study has been conducted on the magnetization switching of single-layer ring magnets with various dimensions ranging from deep sub-micron to micron-size [4,7-10]. For example, the stability of the vortex state of the rings depends on the width, thickness, and shape of the ring structures [8,10], and, for the wider, thinner rings, a direct transition from onion to reverse onion state is favored [10]. In considerably wider rings, more complex multi-step switching occurs, which is involved with generation of complicated magnetization states such as the 'vortex core' state [11]. If the rings are elliptical instead of circular, in-plane anisotropy is observed with the long axis as an easy axis [8] (Fig. 4.1). On applying a field parallel to the long axis, the collective magnetization reversal of the array displays an easy-axis behavior, while on applying the field parallel to the short axis a hard-axis behavior is observed. These results indicate that the shape anisotropy induced by the elliptical shape of the rings dominates the room temperature magnetization reversal of these structures.

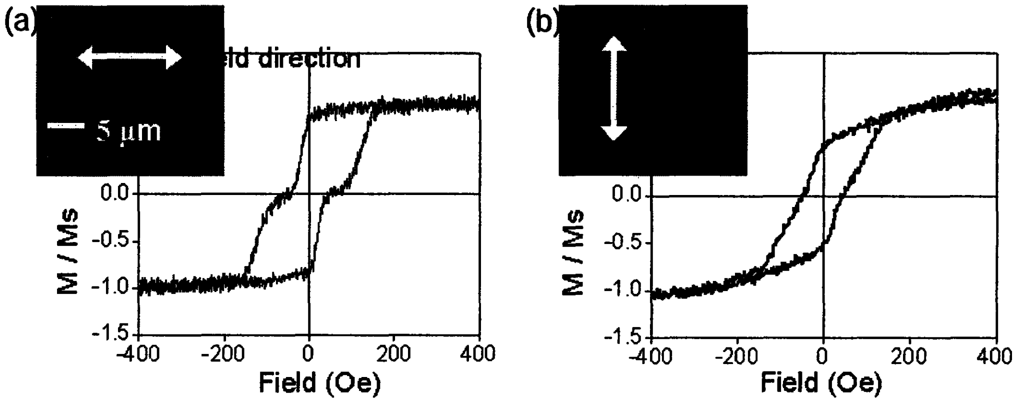

Figure 4.1 Room temperature hysteresis loop measurements applying a magnetic field parallel (a) and perpendicular (b) to the long axis of a CoFe (40 nm) / Cu (3 nm) elliptical-ring array.

There has been little reported work on multilayer rings, especially exchange biased rings. Guo et al. reported that asymmetrically kinked hysteresis loops were observed in NiFe / IrMn rings [12,13]. The kinks, which correspond to the presence of a flux closure state, were found only in the increasing field branch of the hysteresis loops. The origin of the kink was attributed to the formation of antiferromagnetic domain walls.

In this chapter, results on the magnetic characterization of elliptical-ring arrays with different thin film structures and ring widths are presented. A single-NiFe-layer and NiFe / FeMn exchange-biased structure were employed as thin film structures. In the exchange bias rings, the exchange anisotropy is expected to affect the switching behavior and remanent states of the rings. This chapter describes the influence of exchange bias on magnetization reversal in the elliptical-ring arrays.

4.2 Experiment

Arrays of 3 µm major diameter, 1.8 µm minor diameter, and 400 nm and above wide elliptical-rings were fabricated with Zone-plate-array lithography (ZPAL) and lift-off processing. Magnetic thin film multi-layer stacks, Ta (20 nm)/ NiFe (20 nm)/ Cu (3 nm) and Ta (20 nm) / NiFe (20nm) / FeMn (10 nm) / Cu (3nm), were deposited by dc-triode magnetron sputtering on developed resist substrates, previously printed with elliptical-ring patterns with varied widths. During growth of the exchange-biased thin film stacks, an in-situ field of 350 Oe was applied, which imposed an exchange pinning axis along the field direction. This fabrication process was used to create elliptical-ring arrays with a total area of 5×2.5 mm^2 containing $\sim 2 \times 10^5$ rings. The lithography and lift-off process employed to fabricate these elliptical-ring arrays are described in detail in chapter 2. The hysteresis loops of the arrays were measured using a MicroMag^{TM} 2900 alternating gradient magnetometer (AGM). Magnetic imaging of rings was performed with a Digital instruments Nanoscope magnetic force microscope (MFM) using interleave scanning and LiftMode^{TM}.

Micromagnetic simulations for a single-NiFe-layer elliptical-ring were carried out using two-dimensional OOMMF software [14]. Elliptical-ring structures with dimensions corresponding to the experimental results were discretized into 10 by 10 nm square elements. The equilibrium magnetization distribution was calculated using standard parameters for NiFe (saturation moment $M_s = 860 \times 10^3$ A/m, exchange constant $A = 13 \times 10^{-12}$ J/m, anisotropy $K = 100$ J/m^3), with a damping coefficient of 0.5 to allow sufficient time for convergence. To simulate the polycrystalline nature of the films, the anisotropy direction for each cell was randomly oriented across the structure.

4.3 Results and discussion

4.3.1 Single layer elliptical rings

Figure 4.2(a) shows hysteresis loops of arrays of NiFe elliptical-rings with different ring widths. The samples were magnetized parallel to the long axis of the ellipses. The loops suggest that switching in the rings, especially in the wider ring, is a two-step process with some complexity in the spin configuration. The slope of the transitions is not steep, and the plateau between the transitions, where the rings are supposed to exhibit the vortex state, is not flat. The gentle transition slope and slanted plateau are attributed partially to a broad switching field distribution in the arrays and partially to the presence of complex magnetic states. The wide distribution of the switching fields might be due to differences in the dimensions and shape of the rings, introduced during fabrication. In addition, it is worth mentioning that the saturation moment of the NiFe elliptical-ring arrays was on the order of 10 μemu, which is near the sensitivity limit of the AGM, and that might contribute to noise in the transition. The hysteresis loops also display a width dependence of the vortex state stability. The vortex-to-reverse onion transition occurs at a higher field for the narrower elliptical rings.

Figure 4.2(b) shows the simulated hysteresis loops from the 750 and 400 nm wide NiFe ring calculations. Only half the hysteresis loop was calculated to minimize the simulation time, since the loops are symmetrical about the y-axis. The simulations show good agreement with the experimental measurements, displaying a larger plateau for the narrower ring.

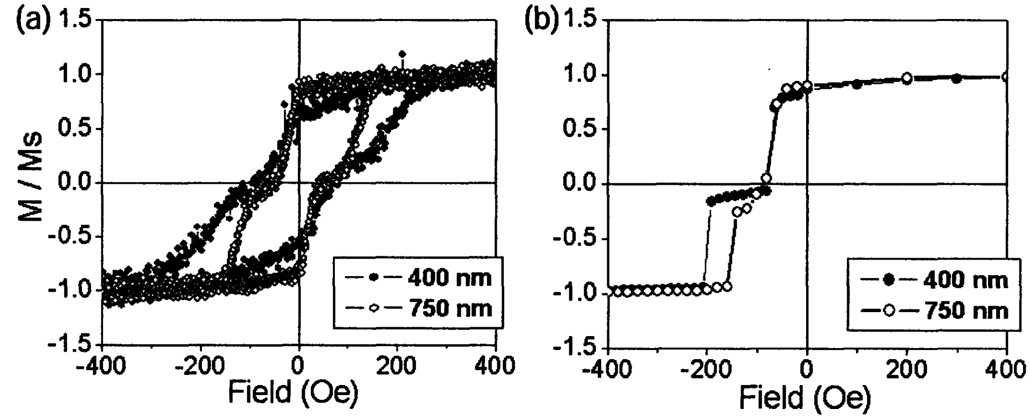

Figure 4.2 (a) Room temperature hysteresis loop measurements on applying a magnetic field parallel to the long axis of Ta(20 nm) / NiFe(20 nm) / Cu(3 nm) elliptical-ring arrays with widths of 400 nm (solid circles) and 750 nm (open circles). (b) Half the hysteresis loops derived from micromagnetic simulations for a 20 nm thick NiFe elliptical-ring with a width of 400 nm (open circles) and 750 nm (solid circles). Solid lines are shown as a guide to the eye.

Spin configurations shown in Figure 4.3 suggests that the onion state domain walls are transformed from the transverse wall to the vortex walls right before the transition to the vortex state. The onion state with a vortex wall resembles the vortex core state, even though the vortex core state usually appears during the vortex to reverse onion transition. The simulations also indicate that the wider ring attains the vortex state via a more complicated sequence, compared with the narrower ring. In the 750 nm wide rings, while the inner rim is switched into the vortex state, the outer rim of the ring remains unchanged. This complex magnetization configuration in the wider ring is attributed to the weaker local shape anisotropy, which allows the magnetization direction to deviate from the circumference of the ring, and that causes the vortex state in the wider ring to be more unstable. Experiments and simulation results of 470 nm wide elliptical-ring arrays, not shown here, confirm the width dependence of the vortex state stability. The second switching field of the 470 nm wide rings falls in between that of the 400 nm and the 750 nm wide rings. This trend is also in agreement with the literature on magnetization reversal in sub-micron size elliptical rings [8].

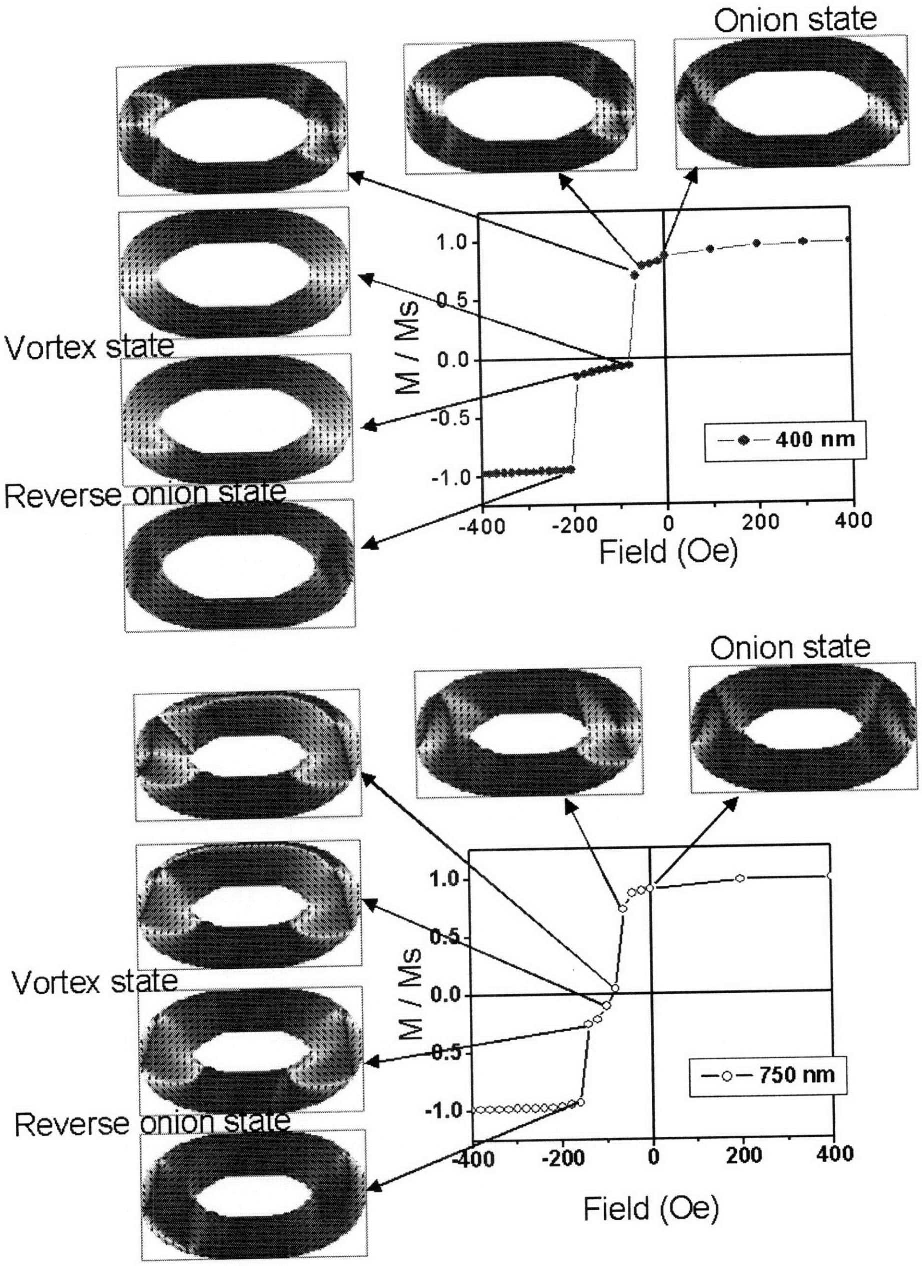

Figure 4.3 Calculated equilibrium magnetization configurations of a 400 nm wide NiFe (20 nm) elliptical-ring (top) and 750 nm wide elliptical-ring (bottom).

4.3.2 Exchange-biased elliptical rings

The hysteresis loops of arrays of elliptical-rings fabricated from a NiFe / FeMn bilayer with different widths are shown in Figure 4.4. The loops resemble those of single layer NiFe rings but are shifted by about 40 Oe, which corresponds to the exchange bias observed in the unpatterned thin film stack. Unlike previous work on exchange-biased circular rings [12,13] two-step transitions were seen in each branch of the loop.

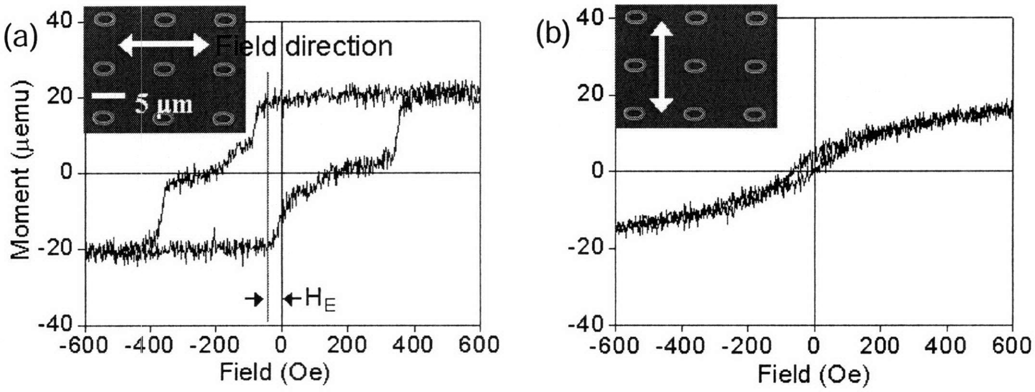

Figure 4.4 Room temperature hysteresis loop measurements applying a magnetic field parallel (a) and perpendicular (b) to the long axis of Ta (20 nm) / NiFe (20 nm) / FeMn (10 nm) / Cu (3 nm) elliptical-ring arrays with 3 μm major diameter, 1.8 μm minor diameter, and widths of 470 nm.

MFM scans on those exchange biased rings were carried out at remanence. Saturating the elliptical-rings in a field along the pinning direction results in the occurrence of the onion state. However, after saturation of the rings opposite to the pinning direction, the reverse onion state, which is not favored by exchange bias, was never observed in the MFM images at remanence. This indicates that the exchange pinning prevents the reverse onion state from forming at remanence, so that the only stable states are the onion and vortex states.

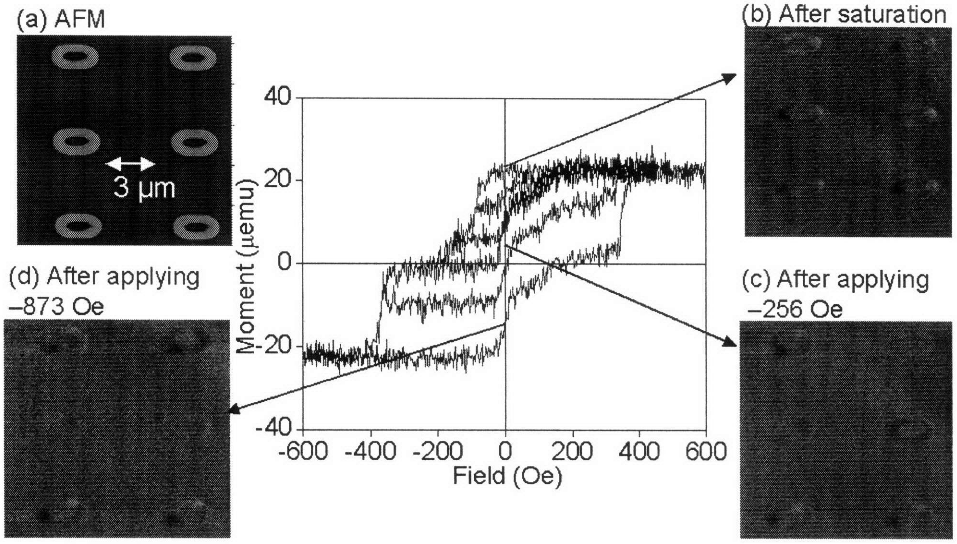

Figure 4.5 MFM images of an array of 470 nm wide Ta (20 nm) / NiFe (20 nm) / FeMn (10 nm) / Cu (3 nm) exchange-biased elliptical-rings. (a) shows the topography of the array obtained from the tapping mode AFM scan. MFM scanning was carried out at remanence after saturating the ring arrays with a field of 1T parallel to the pinning direction (b), after applying –256 Oe (c), and after applying –873 Oe (d), which is enough to saturate the rings opposite to the pinning direction. The minor loops in the center shows what would be the magnetic state of the rings at remanence after applying a certain magnitude of field. For example, after applying –256 Oe the minor loop goes up to around half of the saturated moment at remanence, which is consistent with the MFM image containing half of rings in the onion state and half in the vortex state.

The width dependence of the vortex state stability of the exchange-biased ring structures was found to be consistent with that of the single-NiFe-layer ring arrays. Figure 4.6 shows that the onion-to-vortex and vortex-to-reverse onion transition in 600 nm wide exchange biased rings occurs at lower field than that of 470 nm rings. The MFM image taken after applying –93 Oe (Fig. 4.6(ii)) shows that 600 nm rings are in the vortex state at remanence because the rings are completely switched into the vortex at that field (Fig. 4.6(a)), while 470 nm rings are still in the onion state at remanence. After saturating the rings opposite to the pinning direction, Figure 4.6(c - ii) exhibit the forward onion state in one of the rings, which indicates that some of the 600 nm rings are switched back to the forward onion even at remanence.

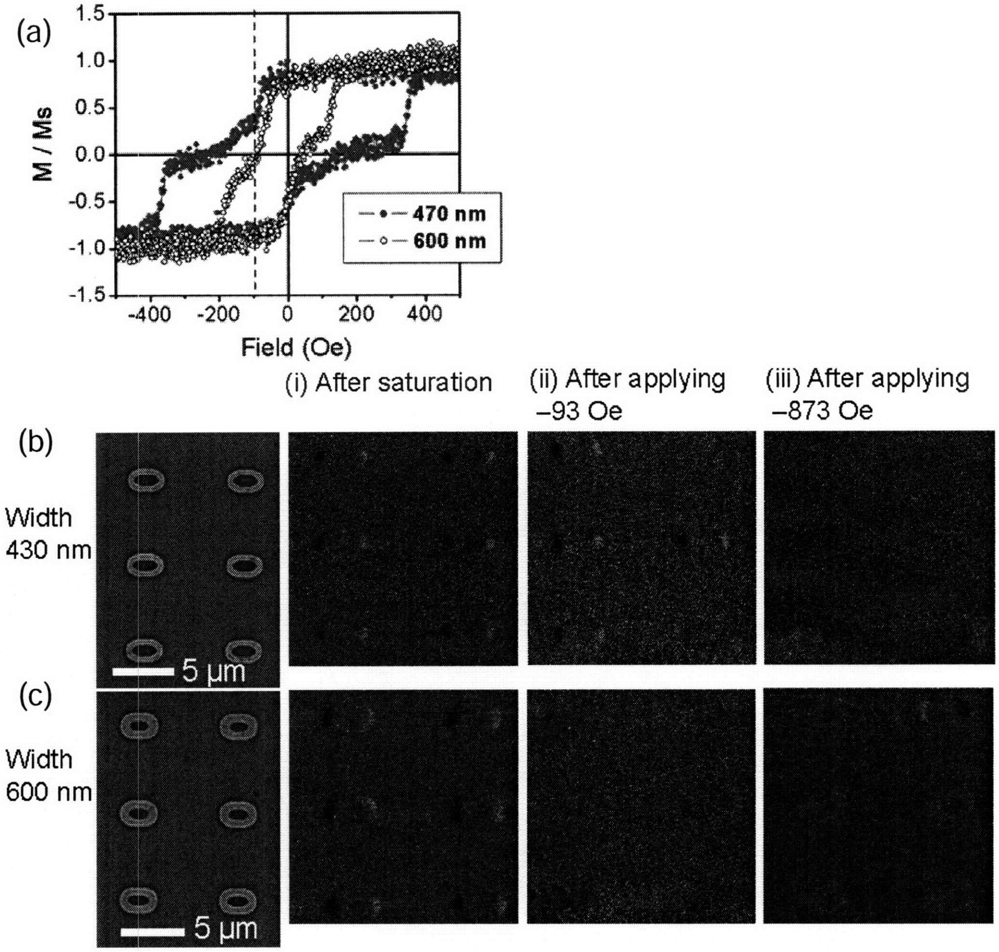

Figure 4.6 (a) Room temperature hysteresis loop measurements applying a magnetic field parallel to the long axis of Ta (20 nm) / NiFe (20 nm) / FeMn (10 nm) / Cu (3 nm) elliptical-ring arrays with widths of 470 nm (solid circles) and 600 nm (open circles).; (b), (c) SEMs and MFMs of the rings with widths of 470 nm and 600 nm, respectively. The rings were imaged after applying a certain magnitude of field. The dashed line in (a) indicates –93 Oe, which was applied prior to taking the images in (ii).

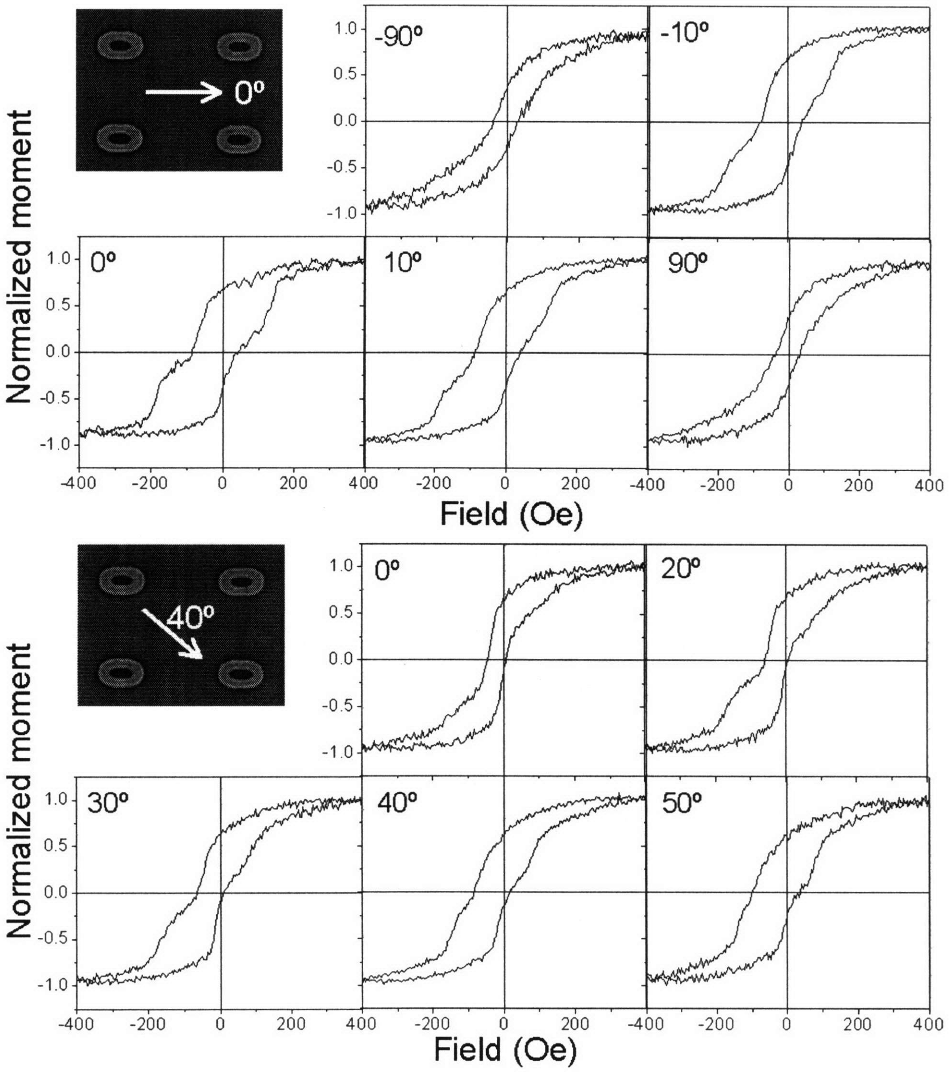

Figure 4.7 Hysteresis loops of an array of 600nm wide NiFe / FeMn exchange bias elliptical rings shown in the inset SEM image. The pinning direction was 0° (top) and 40° (bottom). The field direction, at which the hysteresis was measured, is written in each hysteresis loop. 0° is along the major axis of the ellipse and negative angles represent the direction rotated counterclockwise by the angle.

4.4 Anisotropies in exchange-biased elliptical rings

In an exchange bias elliptical ring, two types of anisotropy caused by the elliptical shape and FM / AFM exchange coupling coexist and interact. The shape anisotropy is uniaxial and the exchange anisotropy is unidirectional. It is of a great deal of interest to understand how these anisotropies influence the magnetization reversal of ring magnets. Hysteresis measurements were carried out using AGM on the arrays of NiFe / FeMn elliptical rings varying the applied field angles with respect to the pinning direction, and the effect of the shape and exchange anisotropy on the vortex state formation was investigated. Large area arrays of NiFe (20nm) / FeMn (10nm) rings with the major diameter of 3 µm, minor diameter of 1.8 µm, and widths of 600 - 700 nm was fabricated using ZPAL and the bias direction of the arrays was modified by means of field cooling. Figure 4.7 shows results of the angular hysteresis measurement on a sample with the pinning direction of 0° and 40° with respect to the major axis of the ellipse. The field was applied at every 10° within ± 90° from the pinning direction in the measurement. The hysteresis loop exhibits two steps in each branch of the loop only when a field is applied at an angle close to the bias direction but, as the field deviates from the direction, the two-step transition appears to become less obvious. This suggests that there exists a field direction, at which the two-step switching accompanying formation of the vortex state is most favored.

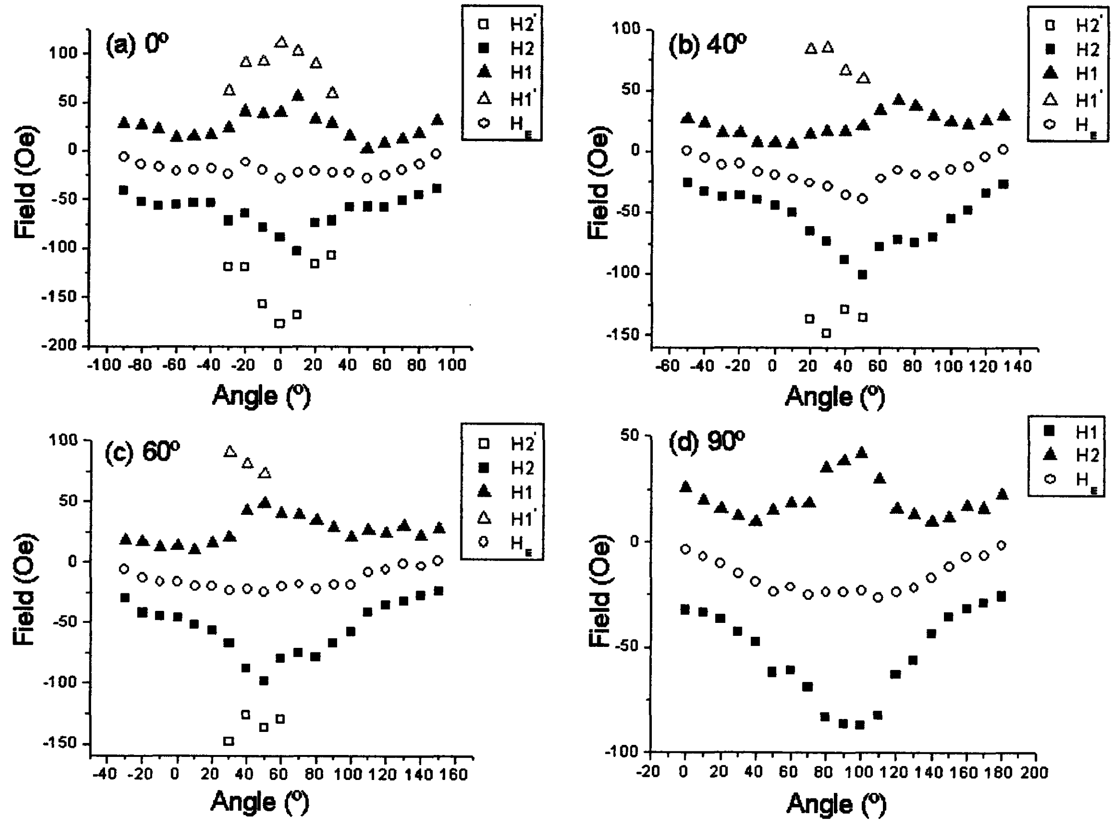

Figure 4.8 Switching fields and exchange field vs. applied field angle of 600nm wide NiFe / FeMn exchange bias elliptical rings with the pinning direction of 0° (a), 40° (b), 60° (c), and 90° (d). As of 90° pinning direction, no two-step switching occurs across all applied field angles.

Figure 4.8 shows the switching fields and exchange bias of the exchange-biased ring array presented in Figure 4.7 as a function of the field direction at several pinning directions. H1 and H2 represent the switching field of the descending branch and ascending branch, respectively. When a two-step switching occurs, H1 and H1′ correspond to the field of onion-to-vortex and vortex-to-reverse onion, respectively, in the descending branch, and H2 and H2′ denote those in the ascending branch. The exchange bias becomes zero at the field angle apart by ± 90° from the pinning direction, and has its maximum around the pinning direction.

Even though hysteresis loops measured at the field angles far from the pinning direction display no two-step switching, it does not necessarily indicate the total extinction of the vortex state at those angles. The measurement was carried out on the samples containing a huge number of rings so that the behavior of individual rings could be obscured by the collective result.

Such vortex formation dependence on the field angle shown in the exchange-biased elliptical rings is also found in single layer elliptical rings in which the vortex formation is promoted by a field parallel to the long axis (Fig. 4.1). The dependence of single layer elliptical rings might be understood in terms of the effect of a uniaxial anisotropy on the magnetization process. As a field is applied along the easy axis, that is, the long axis of the ring, the magnetization reversal occurs more likely via domain wall motion, while the application of a field along the hard axis facilitates magnetization rotation. It is noteworthy that propagation of one of domain walls in the onion state gives rise to the onion-to-vortex transition. In the case of exchange bias elliptical rings, a unidirectional exchange anisotropy should be taken into account as well as the uniaxial shape anisotropy. The easy axis would be no longer along the major axis, and might be placed between the pinning direction and the long axis. Assuming that an exchange-biased elliptical ring is saturated along an applied field, the energy density equation for the ring can be written as

$$\varepsilon = -M_s \cdot H - K_E \cos(\beta - \alpha) - K_S \cos^2 \alpha \qquad (4.1)$$

where the applied field (H) is parallel to the saturation magnetization (M_S) but tilted by an angle α from the major axis. β represents the angle between the exchange bias and the major axis. The exchange anisotropy constant $K_E = M_S \cdot H_E$ was calculated with the exchange field H_E derived from the shifted hysteresis loops of an array of NiFe / FeMn rings. The shape anisotropy constant K_S was attained from initial magnetization curves of demagnetized NiFe elliptical ring arrays by subtracting the integral of the minor axis curve from that of the major axis curve. The K_E and K_S derived from 700 nm wide elliptical rings were 3.9 and 3.2×10^4 erg/cm^3, respectively. The direction of magnetization, at which the anisotropy energy has a minimum, can be calculated with the equation (4.1). For instance, with the above K_E and K_S, the direction α is 15.2° as the pinning direction $\beta = 40°$ in the rings of the corresponding dimension shown in Figure 4.7. Though the equation is based on rough description for the anisotropy energies and the parameters might contain experimental errors, the calculation provides an insight into the easy magnetization direction in the exchange-biased elliptical ring. Taking into account what is shown in the hysteresis loops in Figure 4.7, it can be inferred that, like the vortex formation of single layer rings, that of exchange bias rings is supported by the nominal easy axis magnetization.

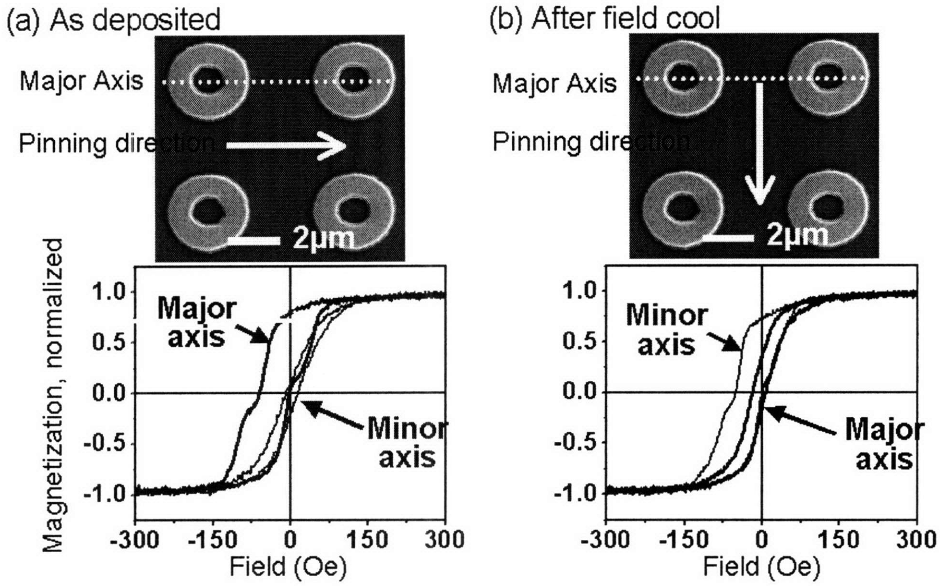

Figure 4.9 Hysteresis loops of NiFe (20 nm) / FeMn (10 nm) elliptical rings with 3.3 μm major diameter, 3.0 μm minor diameter, and a width of 1.0 μm. (a) as deposited, in which the exchange bias direction is along the major axis of the ellipse. The major axis is the easy axis. (b) After a field cooling that sets the exchange bias direction perpendicular to the major axis, the minor axis is now the easy axis. SEMs show the major axis and pinning direction of the rings.

The hysteresis loops of exchange bias elliptical rings with a very low aspect ratio 1.1 of long / short axis (Fig. 4.9) display that, as the pinning direction is changed by field cooling, the easy axis, at which the vortex formation is prominent, follows the pinning direction. However, unidirectional nature of the exchange anisotropy in general does not promote the vortex state. Sort et al. reported that in the exchange bias disks a vortex forms only when an applied field is oriented around the pinning direction not beyond a critical angle. They argued that the exchange bias is compensated by the application of an external field around the pinning direction and such elimination of exchange bias effect allows for the vortex to form during the reversal [15]. This argument might be a possible explanation of the favored vortex formation along the nominal easy axis close to the bias direction, though, since it is based on the assumption that the exchange bias can be described as a superimposed field, the real event should be more complicated.

4.5 Summary

Magnetization reversal in single-NiFe and NiFe / FeMn exchange-biased elliptical-ring arrays has been investigated. Experiments and micromagnetic simulations show that the mesoscopic elliptical rings are large enough to attain complex magnetic states such as the vortex core during the reversal. The complexity in the magnetization configurations increases as the width of the ring increases, and the vortex-to-onion state transition occurs at a smaller field in wider rings. The hysteresis loop of exchange-biased elliptical-ring arrays is shifted by exchange pinning, and the exchange pinning alters the states observed at remanence.

The Formation of the vortex state is affected by shape and exchange bias. In the exchange bias elliptical rings, the vortex formation is most favored with a field applied at an angle close to the pinning direction, which corresponds to the nominal easy axis set by the uniaxial shape anisotropy and unidirectional exchange anisotropy.

Reference

[1] C. A. Ross, S. Haratani, F. J. Castano, Y. Hao, M. Hwang, M. Shima, J. Y. Cheng, B. Vogeli, M. Farhoud, M. Walsh, and H. I. Smith, Journal of Applied Physics **91**, 6848 (2002).

[2] R. P. Cowburn and M. E. Welland, Science **287**, 1466 (2000).

[3] C. A. Ross, F. J. Castano, D. Morecroft, W. Jung, H. I. Smith, T. A. Moore, T. J. Hayward, J. A. C. Bland, T. J. Bromwich, and A. K. Petford-Long, Journal of Applied Physics **99**, 08S501 (2006).

[4] J. Rothman, M. Klaui, L. Lopez-Diaz, C. A. F. Vaz, A. Bleloch, J. A. C. Bland, Z. Cui, and R. Speaks, Physical Review Letters **86**, 1098 (2001).

[5] J. G. Zhu, Y. F. Zheng, and G. A. Prinz, Journal of Applied Physics **87**, 6668 (2000).

[6] F. J. Castano, D. Morecroft, W. Jung, and C. A. Ross, Physical Review Letters **95**, (2005).

[7] F. J. Castano, C. A. Ross, C. Frandsen, A. Eilez, D. Gil, H. I. Smith, M. Redjdal, and F. B. Humphrey, Physical Review B **67**, 184425 (2003).

[8] F. J. Castano, C. A. Ross, and A. Eilez, Journal of Physics D-Applied Physics **36**, 2031 (2003).

[9] S. P. Li, W. S. Lew, J. A. C. Bland, M. Natali, A. Lebib, and Y. Chen, Journal of Applied Physics **92**, 7397 (2002).

[10] Y. G. Yoo, M. Klaui, C. A. F. Vaz, L. J. Heyderman, and J. A. C. Bland, Applied Physics Letters **82**, 2470 (2003).

[11] M. Klaui, C. A. F. Vaz, J. A. C. Bland, T. L. Monchesky, J. Unguris, E. Bauer, S. Cherifi, S. Heun, A. Locatelli, L. J. Heyderman, and Z. Cui, Physical Review B **68**, (2003).

[12] Z. B. Guo, Y. K. Zheng, K. B. Li, Z. Y. Liu, P. Luo, Y. T. Shen, and Y. H. Wu, Journal of Applied Physics **93**, 7435 (2003).

[13] Z. B. Guo, Y. K. Zheng, K. B. Li, Z. Y. Liu, P. Luo, and Y. H. Wu, Journal of Applied Physics **95**, 4918 (2004).

[14] OOMMF is available at http://math.nist.gov.

[15] J. Sort, A. Hoffmann, S. H. Chung, K. S. Buchanan, M. Grimsditch, M. D. Baro, B. Dieny, and J. Nogues, Physical Review Letters **95**, 067201 (2005).

Chapter 5

Vortex chirality in exchange-biased elliptical rings

5.1 Introduction

Magnetization reversal and equilibrium magnetic states of thin-film ferromagnetic disks and rings have been extensively studied in recent years [1-5]. Several topologically distinct magnetic states have been observed in disks and rings, but particular attention has been given to the flux-closed or 'vortex' state, in which the magnetization is oriented circumferentially and there are no domain walls. This state has been proposed for data storage devices in which the chirality of the magnetization rotation is utilized to store a data bit [6], as was practiced in one of the first-generation computer memories, the magnetic core memory. In addition to their technological importance, magnetic vortices in disks and rings have been a subject of scientific interest. The formation of the vortex is determined by a number of different energy and anisotropy terms related to the shape, lateral dimension, and crystalline structure of the magnetic material.

Much work has been devoted to the investigation of the chirality of the vortex in rings and disks under the influence of an in-plane magnetic field, because control of the vortex chirality is essential for applications in data storage and sensors. The chirality has been manipulated by introducing notches or a flat edge to rings [9-11] and disks [12, 13], and rings with an off-centered core [14-16] exhibit a preference for one circulation direction. However, there has been little work on the control of chirality in circular rings other than by introducing geometrical asymmetries, and vortex control in elliptical rings has not been analysed.

As a tunable source of unidirectional anisotropy, exchange bias can be introduced to thin-film disks and rings by employing a ferromagnetic (FM) / antiferromagnetic (AFM) bilayer structure [17]. The effect of lateral confinement on exchange bias has been widely investigated [18-21]. Asymmetric magnetization reversal in exchange biased dots [22, 23], disks [24], and rings [25, 26] has been reported. Exchange bias can affect the formation and chirality of the vortex state. For example, in NiFe / IrMn disks a vortex forms during reversal only when the applied field orientation is close to the exchange pinning direction [27, 28], and circumferential exchange bias in rings with a flat edge has been used to control the vortex chirality [29].

In this chapter, a model is described that predicts the vortex chirality of an elliptical magnetic ring as a function of the direction of the applied field and of the exchange bias, based on the change in energy of the system as the domain walls move. It is demonstrated that the vortex chirality can be tailored with an appropriate combination of applied field direction and exchange bias direction with respect to the major axis.

5.2 Experiments

Arrays of elliptical rings with a major diameter of 3.2 μm, minor diameter of 2 μm and widths of 400 - 500 nm were fabricated using electron-beam lithography and lift-off processing. Single layer rings were made from polycrystalline Co (12 nm) films and exchange biased rings from Co (12 nm) / IrMn (5 nm) bilayer structures, with a Ta (10 - 20 nm) seed layer and Cu (2 nm) capping layer. Co films were deposited by ion beam sputtering at an Ar pressure of 3.5×10^{-5} Torr, a beam current of 35 mA and a beam voltage of 1,000 V. The other materials were grown by dc-triode magnetron sputtering at a pressure of 1 mTorr Ar. The base pressure of the sputter chamber was below 9×10^{-9} Torr. An in-situ magnetic field of 350 Oe was applied during the growth of exchange bias structures in order to induce a bias on the FM layer parallel to the field direction. The exchange bias of unpatterned Co / IrMn films was 75 Oe. The magnetic states of the rings were imaged at remanence using a Digital Instruments Nanoscope magnetic force microscope (MFM) with a low moment tip at a scan height of 30 nm. Fig. 5.1 shows three rows of Co rings, where each ring has a different major axis direction. Each sample consisted of thirteen such rows. In the Co / IrMn sample the exchange bias direction is parallel to the rows of ellipses.

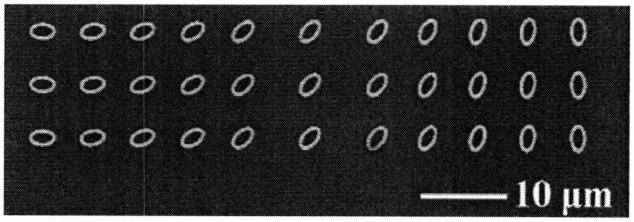

Figure 5.1 Scanning electron micrograph of three rows of Co elliptical rings with major diameter 3.2 μm, minor diameter 2 μm, and width 400 nm.

5.3 Vortex chirality in single layer elliptical rings

In ferromagnetic rings, switching from the onion state to the vortex state typically takes place as one of the domain walls of the onion state unpins and moves until it approaches and annihilates the other wall [2]. A field applied opposite to the saturation direction initiates the movement of the domain walls and they are expected to move such that the Zeeman energy of the system is reduced. The chirality of the resulting vortex state depends on the direction of motion of whichever wall moves first. In the case of symmetric rings, the Zeeman energy reduction is not influenced by the direction (clockwise (CW) or counterclockwise (CCW)) of domain wall motion. The preference for a particular direction of wall motion typically emerges when a ring shows asymmetry in its shape [9, 11, 14, 16]. In the case of an elliptical ring, the curvature varies around the ring, and one may expect a preference for the direction of wall motion if the field is applied at an angle away from the major or minor axes. To model this response, the change in Zeeman energy was calculated for CW and CCW motion of a domain wall. If α represents the angle between the applied field $\mathbf{H_a}$ and the major axis, θ the angle through which the wall has rotated around the ring, $\mathbf{M_s}$ the saturation magnetization, and V the volume of the segment where magnetization has been reversed (Fig. 5.3) then the energy change is given by

$$2\int_V \vec{M}_S \cdot \vec{H}_a \, dV$$

This expression was evaluated numerically for a range of values of α for the geometry of the Co ring samples. The ring was discretized into 100 circumferential strips, each of which was divided into 360 cells. The integral above was evaluated as the sum of inner products of $\mathbf{M_s}$ and $\mathbf{H_a}$ for each cell, multiplied by the volume of the cell, for the region of the ring that reversed (i.e. for a wall moving through angle θ). The calculation was carried out using MatLab, and the code can be found in the appendix at the end of this chapter. The magnetization $\mathbf{M_s}$ is assumed to be always parallel to the edges of the ring but it changes in direction by 180° as a result of wall motion. The magnitude of $\mathbf{H_a}$ was set at 150 Oe, corresponding to the average onion-to-vortex switching field obtained from the MFM measurements. The ring is assumed to have been previously saturated by a field opposite to $\mathbf{H_a}$, and this determines the position of the walls at remanence, prior to application of $\mathbf{H_a}$. The initial domain wall positions were determined experimentally from the MFM images of the remanent onion state of Co elliptical rings measured here (Fig. 5.4(i)). Figure 5.2 shows the remanent onion state domain wall positions. They were in general not coincident with the applied field direction, but were displaced towards the major axis of the ellipse, making a bow shape in the graph. For example, at $\alpha = 0$, 30, 60 and 90° the remanent wall positions are at 0, 11, 32 and 90° respectively to the major axis.

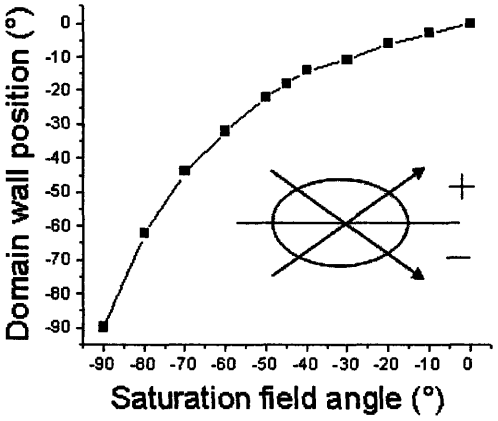

Figure 5.2 Remanent onion state domain wall position at different saturation field angles in the Co elliptical rings with major diameter 3.2 µm, minor diameter 2 µm, and width 400 nm. The inset diagram shows how the ± sign of the wall position and field angle is determined.

Figure 5.3 shows the change in Zeeman energy calculated for several field angles α as one of the domain walls rotates by $\theta \leq +/-90°$. As expected, for a field applied along the major axis (α = 0°) or minor axis (α = 90°), the result is symmetric for CW and CCW wall motion, but at other angles, the curves become asymmetric. The direction of domain wall rotation can be inferred from the slope of the curve of energy vs θ at θ = 0°. The walls of the onion state are predicted to rotate counterclockwise if the field is oriented between α = 0° and 90°, and clockwise if the field is oriented between α = -90° and 0°.

Experimental confirmation of these results was accomplished by observation of the domain walls in the rings by MFM. The detection of vortex chirality has been achieved using a range of imaging techniques [12, 30-32], by magneto-optic Kerr effect measurements [9, 33], and by magnetoresistance measurements [34-36]. MFM cannot measure vortex chirality directly because of the lack of stray fields in the vortex state, but the chirality can be inferred by observing the contrast of the 'twisted' magnetic state that precedes vortex formation [37, 38]. The twisted state is a metastable magnetic state which is formed during the onion-to-vortex transition by the movement of one of the onion state 180° domain walls towards the other to form an in-plane 360° wall. This structure can exist over an extensive field range, and at remanence, but is ultimately annihilated to generate the vortex state. There are four possible configurations of the twisted state, and their contrast in the MFM image enables determination of which domain wall moved first, and whether it moved CW or CCW.

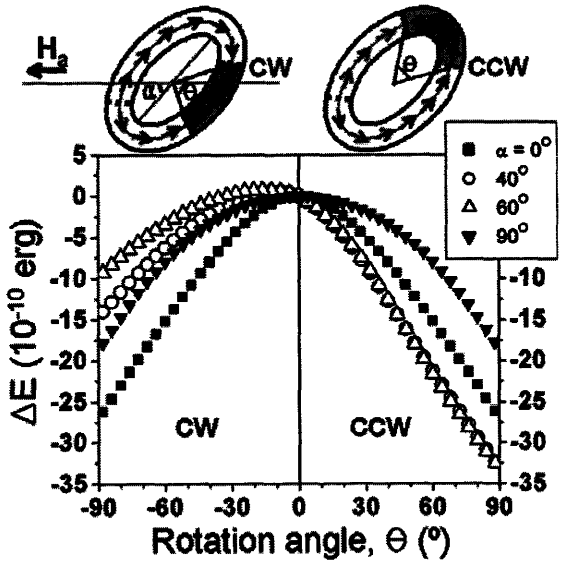

Figure 5.3 Top: schematic diagram describing the motion of domain walls of the onion state in a field H_a applied at angle α to the major axis. The ring was previously saturated opposite to the field direction. The dotted lines represent the initial domain wall positions, and the solid lines the final wall position after one of the walls has rotated by θ. The gray arrows correspond to the original magnetization direction of the onion state and the reversed magnetization region is represented by black arrows. Bottom: Zeeman energy change as a function of the domain wall rotation angle θ for different applied field angles α, after saturation opposite to the field direction. The calculation was carried out for rings with the same geometry as in Figure 5.1.

Figure 5.4 shows the contrast of several twisted states in rings measured at different values of α. The sample contains 143 rings in total, with eleven different major axis directions. For a given reverse field near the onion-to-vortex transition, about 5% of the rings exhibit twisted states. The probability of observing the twisted state was enhanced by applying fields slightly higher than the average onion-to-vortex switching field, which ensures all the rings had been switched from the onion state. Such fields, typically 200 or 232 Oe, do not disturb the twisted state because once the twisted state forms it can survive over an extensive range of the applied field [37]. The higher fields have no influence on the vortex chirality predicted from the model.

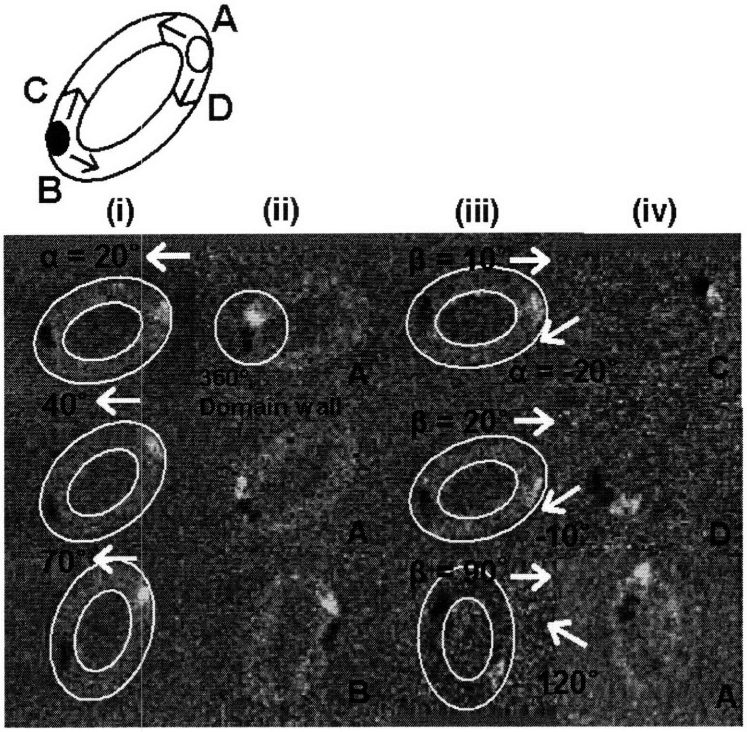

Figure 5.4 MFM images of Co (i, ii) and Co / IrMn (iii, iv) elliptical rings after saturation (i), (iii) and after applying a reverse field of 232 Oe (ii) and 200 Oe (iv) at an angle α. The rings in columns (iii) and (iv) are exchange biased at angle β. Rings (i) and (iii) are outlined for clarity. In (ii) the contrast of a 360 degree wall is shown with an outline. The schematic diagram on the top shows the four possible directions of domain wall motion. Directions A and B represent counterclockwise rotation, and C and D clockwise rotation. Each image of a twisted state in columns (iii) and (iv) is labeled with a letter showing the wall motion direction that generated it.

Several twisted states were found for each value of α. The twisted states consistently demonstrated CCW rotation of the domain walls for all field angles between α = 0° and 90°, in agreement with the calculation results. There was no preference for which of the two walls moved first; this is believed to be determined by local pinning due to edge imperfections or variations in magnetocrystalline anisotropy. For example, in Fig. 5.4(ii), in the sample with α = 20° the bright-contrast domain wall rotated CCW along the upper arm of the ring, whereas in the sample with α = 70° the dark-contrast domain wall also moved CCW but traveled along the lower arm of the ring. These results show that in elliptical rings the desired chirality of the vortex state can be obtained by switching the rings from the onion state using an appropriate field direction, and are analogous to vortex control by unpinning of walls in notched rings [10].

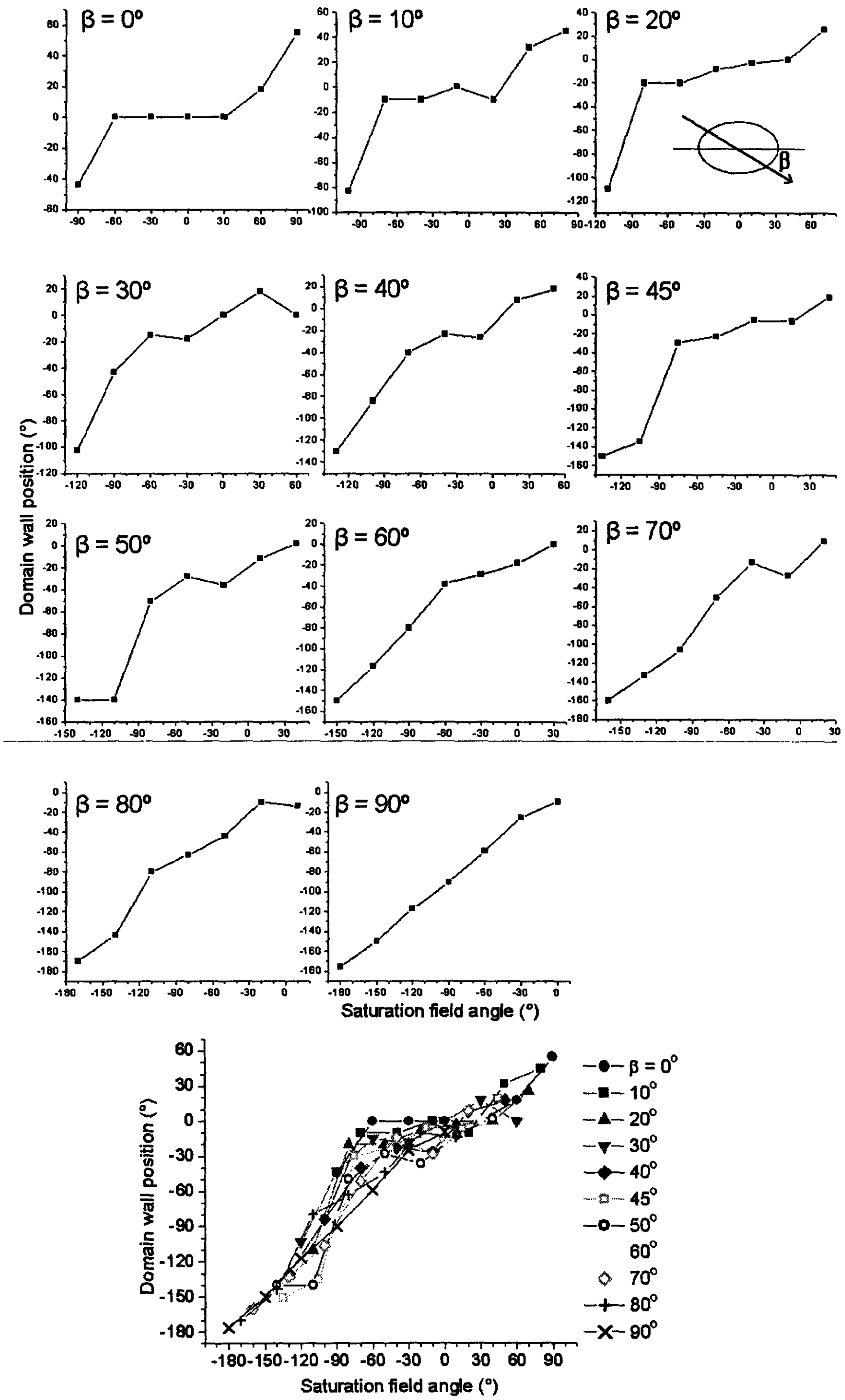

Figure 5.5 Remanent onion state domain wall position vs. saturation field angles at different exchange bias angle β between 0° and 90° in the Co / IrMn elliptical rings with major diameter 3.2 μm, minor diameter 2 μm, and width 500 nm. The angle β is shown in the inset diagram. All the data points are presented together in the graph at the bottom.

5.4 Vortex chirality in exchange-biased elliptical rings

Vortex chirality in exchange bias elliptical rings presents a more complex situation because the angle β between the exchange bias direction and the major axis also influences the wall motion. The model was modified to include exchange bias by adding the inner product of the exchange field and the magnetization to the energy term, so that changes in both Zeeman and exchange energy could be calculated as a domain wall rotates either clockwise or counterclockwise. The exchange field of the rings was taken to be the same as that of the unpatterned film, as found previously [39].

Initial domain wall positions of the rings were measured systematically from MFM images such as those in Fig. 5.4(iii), for a range of α and β (Fig. 5.5) When the exchange bias is oriented along the major axis of the ellipse (β = 0°), the remanent onion domain walls stay around the ends of the ellipse (at the domain wall position angle = 0°) until the saturation field angle reaches more than 30° off from the major axis. However, when β = 90°, that is, exchange bias direction is perpendicular to the major axis, the wall position varies almost linearly following the saturation field direction. These data show how the shape anisotropy and exchange bias anisotropy interplay and affect the onion state domain wall position in exchange biased elliptical rings.

Figure 5.6 shows the energy for a ring with β = 60°, for field angles of α = 0, 30, 60, and 90°. In contrast to the unbiased ring, the change in energy vs. wall displacement angle ΔE(θ) for α = 0° is no longer symmetrical, and indicates a preference for CW wall motion. For α = 30° the motion is CW, but for α = 90° the motion is CCW. The critical field angle α_c at which the wall motion changes sign corresponds to the value of α at which ΔE(θ) has a maximum at θ = 0°, which in this case is approximately 55° (inset of Fig. 5.6). For this particular ring geometry and material the critical field direction α_c is close to the exchange bias direction β because the exchange anisotropy is large compared with the shape anisotropy of the elliptical ring. For circular rings, we expect $\alpha_c = \beta$, while for elliptical rings, as the shape anisotropy increases compared to the exchange anisotropy, α_c will approach zero (coincident with the major axis of the ring).

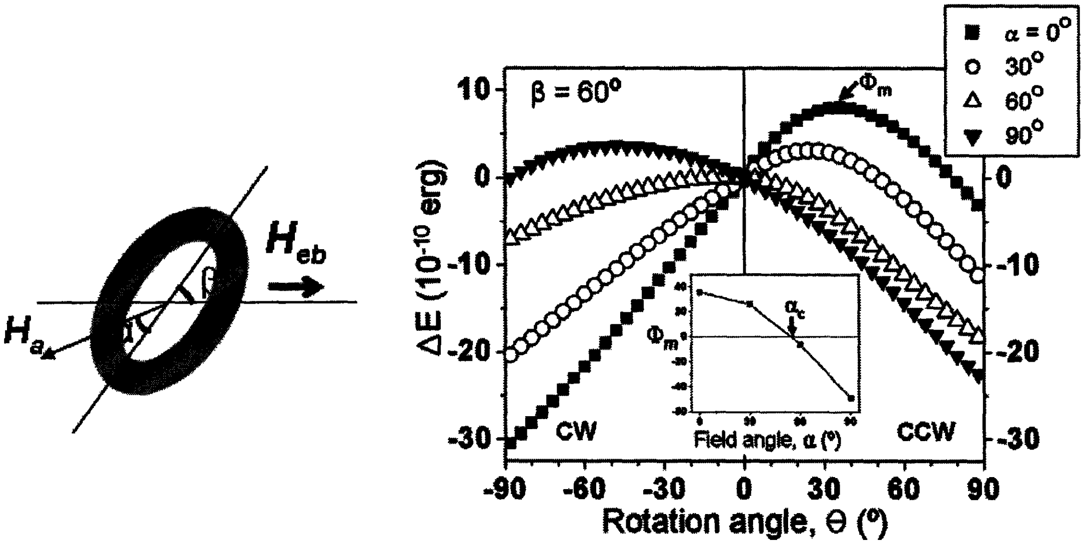

Figure 5.6 The calculated energy change in a 500 nm wide exchange biased elliptical ring for different field angles α as a domain wall rotates clockwise or counterclockwise through angle θ. The exchange pinning angle β was 60°. The value of $\theta = \Phi_m$ at which each curve has a maximum is plotted vs. field angle α in the inset. This passes through zero at α_c = 55° for this particular ring geometry and exchange bias direction.

Based on a series of calculations for various values of α and β, a phase diagram of CW and CCW domain wall rotation, i.e. a phase diagram of the vortex chirality, was plotted (Fig. 5.7). The boundary between the two regimes, at α_c, is located near the line α = β. This phase diagram was compared with the MFM images of the twisted states in the exchange biased elliptical rings. Examples of MFM data are given in Fig. 5.4(iv), which shows CW wall motion for α = -20°, β = 10°, and for α = -10°, β = 20°, and CCW motion for α = 120°, β = 90°.

The points where one or more twisted states were found were marked on the phase diagram with different symbols depending on the direction of domain wall rotation. These experimental data points are almost entirely in agreement with the findings from the calculation, and support the model that predicts the CW or CCW direction of movement of the domain walls. Rings with $\alpha \approx \alpha_c$ show CW or CCW wall motion approximately equally. As in the single-layer Co rings, there was no preference for which of the two domain walls in the onion state moved first; only for the direction of movement.

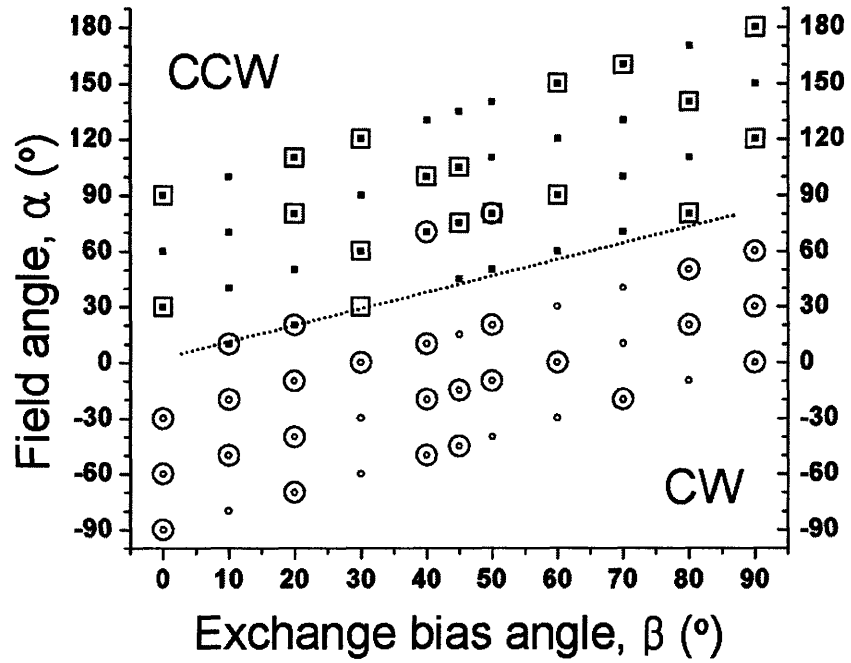

Figure 5.7 Phase diagram of the vortex chirality of a 500 nm wide exchange biased elliptical ring as a function of the external field angle α and exchange bias angle β. The small solid squares represent the points where counterclockwise circulation is predicted by the calculation and small open circles represent clockwise circulation. The critical field angle, $\alpha_c(\beta)$, is shown by a dotted line close to $\alpha = \beta$, along which there is no preference for either wall motion direction. The large open squares and circles indicate experimental observations of the chirality of the twisted state, the precursor to the vortex state: squares for CCW chirality and circles for CW chirality.

5.5 Summary

This work demonstrates that the direction of vortex circulation in exchange biased elliptical rings can be controlled by modifying the field and exchange bias angles. Moreover, the fact that exchange biased elliptical rings respond differently to the same reverse field compared with single layer rings is noteworthy. For example, using the geometry and layer thicknesses in this experiment, if a reverse field at $\alpha = 30°$ is applied to an exchange biased elliptical ring pinned at $\beta = 60°$, the domain wall in the ring would rotate clockwise, while the domain wall in a single layer Co ring would rotate counterclockwise in the same field, leading to antiparallel vortices. This characteristic suggests that in a structure comprised of a multilayer stack containing both pinned and unpinned rings, for example a spin valve, a desired vortex state can be obtained independently in each ferromagnetic layer by using the effects of shape and exchange bias. Also the tunability of the exchange bias direction by field cooling can be used for post-production control of the vortex chirality, which is unavailable from shape anisotropy. This modeling approach can be generalized to other geometries and materials, and will be valuable in understanding the behavior of ring shaped magnetoelectronic or sensor devices.

References

[1] C. A. Ross, F. J. Castano, D. Morecroft, *et al.*, J. Appl. Phys. **99**, 08S501 (2006).

[2] J. Rothman, M. Klaui, L. Lopez-Diaz, *et al.*, Phys. Rev. Lett. **86**, 1098 (2001).

[3] T. Shinjo, T. Okuno, R. Hassdorf, *et al.*, Science **289**, 930 (2000).

[4] R. P. Cowburn and M. E. Welland, Science **287**, 1466 (2000).

[5] R. P. Cowburn, D. K. Koltsov, A. O. Adeyeye, *et al.*, Phys. Rev. Lett. **83**, 1042 (1999).

[6] J. G. Zhu, Y. F. Zheng, and G. A. Prinz, J. Appl. Phys. **87**, 6668 (2000).

[7] Y. G. Yoo, M. Klaui, C. A. F. Vaz, *et al.*, Appl. Phys. Lett. **82**, 2470 (2003).

[8] L. Lopez-Diaz, J. Rothman, M. Klaui, *et al.*, J. Appl. Phys. **89**, 7579 (2001).

[9] M. Klaui, J. Rothman, L. Lopez-Diaz, *et al.*, Appl. Phys. Lett. **78**, 3268 (2001).

[10] M. Klaui, C. A. F. Vaz, J. A. C. Bland, *et al.*, Appl. Phys. Lett. **81**, 108 (2002).

[11] R. Nakatani, T. Yoshida, Y. Endo, *et al.*, J. Appl. Phys. **95**, 6714 (2004).

[12] T. Taniuchi, M. Oshima, H. Akinaga, *et al.*, J. Appl. Phys. **97**, 10J904 (2005).

[13] M. Schneider, H. Hoffmann, and J. Zweck, Appl. Phys. Lett. **79**, 3113 (2001).

[14] P. Vavassori, R. Bovolenta, V. Metlushko, *et al.*, J. Appl. Phys. **99**, 053902 (2006).

[15] F. Q. Zhu, G. W. Chern, O. Tchernyshyov, *et al.*, Phys. Rev. Lett. **96**, 027205 (2006).

[16] E. Saitoh, M. Kawabata, K. Harii, *et al.*, J. Appl. Phys. **95**, 1986 (2004).

[17] J. Nogues, J. Sort, V. Langlais, *et al.*, Phys. Rep.-Rev. Sec. Phys. Lett. **422**, 65 (2005).

[18] V. Baltz, J. Sort, S. Landis, *et al.*, Phys. Rev. Lett. **94**, 117201 (2005).

[19] J. Eisenmenger, Z. P. Li, W. A. A. Macedo, *et al.*, Phys. Rev. Lett. **94**, 057203 (2005).

[20] Z. P. Li, O. Petracic, J. Eisenmenger, *et al.*, Appl. Phys. Lett. **86**, 072501 (2005).

[21] J. Yu, A. D. Kent, and S. S. P. Parkin, J. Appl. Phys. **87**, 5049 (2000).

[22] E. Popova, H. Loosvelt, M. Gierlings, *et al.*, Eur. Phys. J. B **44**, 491 (2005).

[23] E. Girgis, R. D. Portugal, H. Loosvelt, *et al.*, Phys. Rev. Lett. **91**, 187202 (2003).

[24] J. Camarero, J. Sort, A. Hoffmann, *et al.*, Phys. Rev. Lett. **95**, 057204 (2005).

[25] Z. B. Guo, Y. K. Zheng, K. B. Li, *et al.*, J. Appl. Phys. **95**, 4918 (2004).

[26] Z. B. Guo, Y. K. Zheng, K. B. Li, *et al.*, J. Appl. Phys. **93**, 7435 (2003).

[27] J. Sort, G. Salazar-Alvarez, M. D. Baro, *et al.*, Appl. Phys. Lett. **88**, 042502 (2006).

[28] J. Sort, A. Hoffmann, S. H. Chung, *et al.*, Phys. Rev. Lett. **95**, 067201 (2005).

[29] R. Nakatani, T. Yoshida, Y. Endo, *et al.*, J. Magn. Magn. Mater. **286**, 31 (2005).

[30] U. Welp, V. K. Vlasko-Vlasov, J. M. Hiller, *et al.*, Phys. Rev. B **68**, 054408 (2003).

[31] M. Klaui, C. A. F. Vaz, J. A. C. Bland, *et al.*, Phys. Rev. B **68**, 134426 (2003).

[32] J. Raabe, R. Pulwey, R. Sattler, *et al.*, J. Appl. Phys. **88**, 4437 (2000).

[33] M. Grimsditch, P. Vavassori, V. Novosad, *et al.*, Phys. Rev. B **65**, 172419 (2002).

[34] T. Kimura, Y. Otani, and J. Hamrle, Appl. Phys. Lett. **87**, 172506 (2005).

[35] P. Vavassori, M. Grimsditch, V. Metlushko, *et al.*, Appl. Phys. Lett. **86**, 072507 (2005).
[36] K. Harii, E. Saitoh, H. Miyajima, *et al.*, J. Magn. Magn. Mater. **282**, 19 (2004).
[37] F. J. Castano, C. A. Ross, A. Eilez, *et al.*, Phys. Rev. B **69**, 144421 (2004).
[38] F. J. Castano, C. A. Ross, and A. Eilez, J. Phys. D-Appl. Phys. **36**, 2031 (2003).
[39] W. Jung, F. J. Castano, D. Morecroft, *et al.*, J. Appl. Phys. **97**, 10K113 (2005).

Appendix

Matlab code used to calculate Zeeman energy change in a single-layered elliptical ring with 3.2/2μm diameter and 400 nm width.

```
r=1.6;
ar=2/3.2;
w=.4;
t_film=1.2;
th=[-90 -80 -70 -60 -50 -45 -40 -30 -20 -10 0 10 20 30 40 45 50 60 70
80 90];
dwa=[90 49 37 29 21 16 14 11 9 3 0 -3 -9 -11 -14 -16 -21 -29 -37 -49 -
90];
for q=1:21
theta_h=th(q)*pi/180;
h=[-cos(theta_h) sin(theta_h)];
dw_angle=dwa(q)*pi/180;
for n=1:101
   ra=r-w+w/100*(n-1);
   rb=ar*r-w+w/100*(n-1);
   hk=sqrt(1-rb^2/ra^2);

   if dw_angle<=0
   arclength=ra*(elit(hk,-dw_angle*180/pi)+elit(hk,dw_angle*180/pi+90));
   else
   arclength=ra*(2*elit(hk,90)-elit(hk,dw_angle*180/pi)-elit(hk,-
dw_angle*180/pi+90));
   end

   for m=1:91
      t=dw_angle+pi/2/90*(m-1);
      vx=-ra*sin(t);
      vy=rb*cos(t);
      va=sqrt((vx.^2)+(vy.^2));
      v=[vx./va; vy./va];
      d_arclength=arclength/90;
      f(n,m)=-2*h*v*d_arclength*w/100*t_film*1400*150*1e-4;
   end
end
cs=cumsum(f,2);
z_energy=sum(cs,1);
disp_angle=0:90;
z=[disp_angle; z_energy];
if th(q)>=0
   filenum=strcat('z_',int2str(th(q)));
else
   filenum=strcat('z_m',int2str(-th(q)));
end
filename=strcat(filenum,'.asc');
fid=fopen(filename, 'wt');
fprintf(fid,'%7.4f %7.4f\n', z);
fprintf(fid,'\n');
```

```
for n=1:101
   ra=r-w+w/100*(n-1);
   rb=ar*r-w+w/100*(n-1);
   hk=sqrt(1-rb^2/ra^2);

   if dw_angle>=0
   arclength=ra*(elit(hk,dw_angle*180/pi)+elit(hk,-dw_angle*180/pi+90));
   else
   arclength=ra*(2*elit(hk,90)-elit(hk,-dw_angle*180/pi)-
elit(hk,dw_angle*180/pi+90));
   end

   for m=1:91
      t=dw_angle-pi/2/90*(m-1);
      vx=ra*sin(t);
      vy=-rb*cos(t);
      va=sqrt((vx.^2)+(vy.^2));
      v=[vx./va; vy./va];
      d_arclength=arclength/90;
      f(n,m)=-2*h*v*d_arclength*w/100*t_film*1400*150*1e-4;
   end
end
cs=cumsum(f,2);
z_energy=sum(cs,1);
disp_angle=0:-1:-90;
z=[disp_angle; z_energy];


fprintf(fid,'%7.4f %7.4f\n', z);
fclose(fid);
disp('File saved as:');
disp(filename);


end
```

Matlab code used to calculate Zeeman energy and exchange energy change in an exchange-biased elliptical ring with 3.2/2μm diameter and 500 nm width.

```
r=1.6;
ar=2/3.2;
w=.5;
t_film=1.2;
the=[0 10 20 30 40 45 50 60 70 80 90];
dwa=[55 45 26 0 18 19 2 0 9 -14 -9;%-90
     18 32 0 18 8 -7 -12 -18 -28 -10 -25;%-60
     0 -10 -3 0 -26 -6 -36 -29 -14 -44 -59;%-30
     0 0 -8 -18 -23 -23 -28 -38 -51 -63 -90;%0
     0 -10 -20 -15 -40 -30 -50 -80 -106 -80 -117;%30
     0 -10 -20 -43 -84 -135 -140 -117 -133 -144 -150;%60
     -44 -83 -110 -103 -130 -151 -140 -150 -160 -170 -176];%90
for p=1:11
theta_e=the(p)*pi/180;
```

```
e=[cos(theta_e) -sin(theta_e)]/2;
for q=1:7
theta_h=theta_e-pi/2+pi/6*(q-1);
h=[-cos(theta_h) sin(theta_h)];
dw_angle=dwa(q,p)*pi/180;
for n=1:101
   ra=r-w+w/100*(n-1);
   rb=ar*r-w+w/100*(n-1);
   hk=sqrt(1-rb^2/ra^2);

   if dw_angle>=0
       arclength=ra*(2*elit(hk,90)-elit(hk,dw_angle*180/pi)-elit(hk,-
dw_angle*180/pi+90));
   elseif dw_angle>=-pi/2
       arclength=ra*(elit(hk,-
dw_angle*180/pi)+elit(hk,dw_angle*180/pi+90));
   else
       dw_angle1=pi+dw_angle;
       arclength=ra*(2*elit(hk,90)-elit(hk,dw_angle1*180/pi)-elit(hk,-
dw_angle1*180/pi+90));
   end

   for m=1:91
      t=dw_angle+pi/2/90*(m-1);
      vx=-ra*sin(t);
      vy=rb*cos(t);
      va=sqrt((vx.^2)+(vy.^2));
      v=[vx./va; vy./va];
      d_arclength=arclength/90;
      f(n,m)=-2*(h+e)*v*d_arclength*w/100*t_film*1400*150*1e-4;
   end
end
cs=cumsum(f,2);
z_energy=sum(cs,1);
disp_angle=0:90;
z=[disp_angle; z_energy];
if -90+30*(q-1)>=0
   filenum=strcat('ez_',int2str(the(p)),'_',int2str(-90+30*(q-1)));
else
   filenum=strcat('ez_',int2str(the(p)),'_m',int2str(90-30*(q-1)));
end
filename=strcat(filenum,'.asc');
fid=fopen(filename, 'wt');
fprintf(fid,'%7.4f %7.4f\n', z);
fprintf(fid,'\n');

for n=1:101
   ra=r-w+w/100*(n-1);
   rb=ar*r-w+w/100*(n-1);
   hk=sqrt(1-rb^2/ra^2);

   if dw_angle>=0
   arclength=ra*(elit(hk,dw_angle*180/pi)+elit(hk,-dw_angle*180/pi+90));
   elseif dw_angle>=-pi/2
   arclength=ra*(2*elit(hk,90)-elit(hk,-dw_angle*180/pi)-
elit(hk,dw_angle*180/pi+90));
   else
```

```
        dw_angle1=pi+dw_angle;
        arclength=ra*(elit(hk,dw_angle1*180/pi)+elit(hk,-
dw_angle1*180/pi+90));
   end

   for m=1:91
      t=dw_angle-pi/2/90*(m-1);
      vx=ra*sin(t);
      vy=-rb*cos(t);
      va=sqrt((vx.^2)+(vy.^2));
      v=[vx./va; vy./va];
      d_arclength=arclength/90;
      f(n,m)=-2*(h+e)*v*d_arclength*w/100*t_film*1400*150*1e-4;
   end
end
cs=cumsum(f,2);
z_energy=sum(cs,1);
disp_angle=0:-1:-90;
z=[disp_angle; z_energy];

fprintf(fid,'%7.4f %7.4f\n', z);
fclose(fid);
disp('File saved as:');
disp(filename);


end
end
```

Matlab function used to calculate the arc length of the ellipse

```
function [ee]=elit(hk,phi);
%       ==================================================
%       Purpose: Compute complete and incomplete elliptic
%                integrals F(k,phi)and E(k,phi)
%       Input  : HK  --- Modulus k(0 ?k ?1)
%                Phi --- Argument(in degrees)
%       Output : FE  --- F(k,phi)
%                EE  --- E(k,phi)
%       ==================================================
g=0.0d0;
pi=3.14159265358979d0;
a0=1.0d0;
b0=sqrt(1.0d0-hk.*hk);
d0=(pi./180.0d0).*phi;
r=hk.*hk;
if(hk == 1.0d0&phi == 90.0d0);
fe=1.0d+300;
ee=1.0d0;
elseif(hk == 1.0d0);
fe=log((1.0d0+sin(d0))./cos(d0));
ee=sin(d0);
else;
fac=1.0d0;
```

```
for  n=1:40;
a=(a0+b0)./2.0d0;
b=sqrt(a0.*b0);
c=(a0-b0)./2.0d0;
fac=2.0d0.*fac;
r=r+fac.*c.*c;
if(phi ~= 90.0d0);
d=d0+atan((b0./a0).*tan(d0));
g=g+c.*sin(d);
d0=d+pi.*fix(d./pi+.5d0);
end;
a0=a;
b0=b;
if(c < 1.0d-7)break; end;
end;
ck=pi./(2.0d0.*a);
ce=pi.*(2.0d0-r)./(4.0d0.*a);
if(phi == 90.0d0);
fe=ck;
ee=ce;
else;
fe=d./(fac.*a);
ee=fe.*ce./ck+g;
end;
end;
return;
```

Chapter 6

GMR of pseudo spin valve and spin valve elliptical rings

6.1 Introduction

Flux-closure magnetization of ring-shaped magnetic structures, referred as the 'vortex' state, is of technological interest due to its possible application in magnetic random access memories (MRAM) [1]. The absence of the stray field in the vortex state is advantageous of high density data storage. In the ring-shaped memory devices data bits are stored by different chirality of the vortex state, clockwise (CW) or counterclockwise (CCW). Much work has been devoted to achieve the control over the chirality of the vortex state, mostly by introducing geometrical asymmetries in the ring. Notches, a flat edge [2, 3] or an off-centered core [4-6] has been used in single-layered circular rings.

Besides the shape modifications, few work has been carried out on the control of the vortex chirality. It has been reported that the unidirectional anisotropy of ferromagnetic (FM) / antiferromagnetic (AFM) exchange coupling structures influences the chirality of the vortex state in the exchange-biased rings. Circumferential exchange bias was used to control the vortex chirality in a NiFe / IrMn ring with a flat edge [7]. In Chapter 5, control of the vortex chirality in a single layer and exchange-biased elliptical ring was demonstrated. An analytical model was proposed, which allows prediction of the chirality of the vortex state at a given applied field direction and exchange pinning direction with respect to the major axis of the ellipse. The model was confirmed by experimental observation using magnetic force microscopy (MFM).

Multilayered magnetic rings such as exchange-biased rings have been received relatively little attention compared to the single layer rings. Recently there has been an upsurge of interest in giant magnetoresistance (GMR) or magnetic tunnel junction (MTJ) structured rings [8-16]. Pseudo spin valve (PSV) rings, consisting of two FM layers separated by a non-magnetic spacer, have been fabricated and their magnetization reversal and magnetoresistance (MR) were investigated [13-16]. However, no vortex chirality control of individual FM layers in GMR multilayered rings has been reported.

In this chapter, the vortex chirality of spin valve rings is explored. Spin valve structures are comprised of two FM layers, one is pinned by exchange coupling with an antiferromagnet (AFM) and one is free, separated by a non-magnetic metal spacer. Such structure is equivalent to the combination of a single FM layer and an exchange bias structure having a metal layer in between. Based on the control previously established over single layer rings and exchange-biased rings [17], an independent control of the vortex chirality in the free layer and pinned layer in a spin valve ring is demonstrated.

6.2 Experiments

Spin valve ring devices were fabricated using two-level electron-beam lithography and lift-off processing (Fig. 6.1). Elliptical rings of a 3.2 μm major diameter, 1.9 μm minor diameter and widths of 340 – 370 nm were fabricated on a chip that contains contact pads of Ti (4nm) / Au (30nm) for electric measurement. The electron-beam lithography was carried out using Raith 150 system. Spin valve films was deposited by dc-triode magnetron sputtering and ion beam sputtering at Ar pressure of 1 mTorr and 4×10^{-5} Torr, respectively. Such a low deposition pressure enables a successful lift off of sputtered metal. The film structures were Ta (2nm) / NiFe (10nm) / Cu (8nm) / Co (8nm) / IrMn (5nm) / Cu (2nm) and NiFe (6nm) / Cu (4nm) / Co (5nm) / IrMn (5nm) / Au (4nm). A field cooling was carried out after the spin valve rings were defined and PMMA was spun on them for the second level e-beam writing of the final contact patterns. The field cooling re-established the exchange bias in the rings, which might be disturbed by the post-bake of the PMMA layer. 370 nm wide Ta (2nm) / Cu (140nm) contact wires connect the rings to the contact pads.

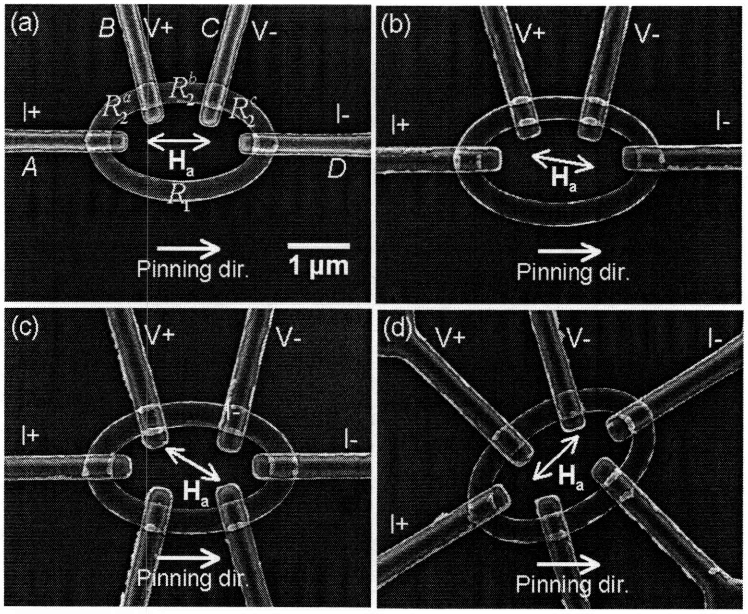

Figure 6.1 Scanning electron micrographs of Ta (2nm) / NiFe (10nm) / Cu (8nm) / Co(8nm) / IrMn (5nm) / Cu (2nm) spin valve rings with major / minor diameter of 3.2 / 1.9 μm and width of 340 nm (a), and NiFe (6nm) / Cu (4nm) / Co (5nm) / IrMn (5nm) / Au (4nm) rings with width of 370 nm (b – d). The arrows represent the direction of an applied field (H_a) and the direction of exchange pinning. Labels beside the contact wires show the electric configuration of the MR measurement. A, D and B, C in (a) are the leads for current and voltage, respectively. Resistance of each section of the ring is also labeled in (a).

6.3 Magnetoresistance (MR) measurement of GMR ring devices

Current-in-plane (CIP) magnetoresistance (MR) of the spin valve ring devices was measured using a 4-point-probe ac technique with lock-in detection at 1 kHz. A current was injected to the ring via two contacts at the ends of the ellipse (A and D, Fig. 6.1(a)) and the resistance of the ring is measured by detecting the voltage drop between two other leads (B and C). In a ring, the current flow is divided into the two arms, which can be modeled as a parallel circuit. The magnitude of the current flowing through each arm is determined by the relative resistance R$_1$ and R$_2$ ($R_2 = R_2^a + R_2^b + R_2^c$), and the measured voltage drop V_2^b is related to R_2^b, the resistance of the section between the voltage leads, as following.

$$\frac{V_2^b}{I} = \frac{R_1 R_2^b}{R_1 + R_2} \qquad (6.1)$$

where I represents the injected current, which was 10 μA as the root-mean-square average.

Equation 6.1 indicates that V_2^b reflects not only R_2^b but also the resistance of the rest of the ring. V_2^b can be expressed with GMR of the unpatterned film structure. GMR is described as below

$$GMR = \frac{\rho - \rho_o}{\rho_o} = \frac{\rho_m - \rho_o}{\rho_o}\frac{(1-\cos\theta)}{2} = \frac{\Delta\rho_m}{\rho_o}v = \psi_m v \qquad (6.2)$$

where ρ_m and ρ_o denote the maximum and minimum resistivity, respectively, and θ is the relative angle between the magnetization directions of the two ferromagnetic layers. $\psi_m = \Delta\rho_m / \rho_o$ is the maximum MR of the film structure. If it is assumed that the length of each arm, l_1 and l_2, is identical, and the cross-section area A is constant throughout the entire ring, because

$$R = \frac{l}{A}\rho = \frac{l}{A}(\Delta\rho_m v + \rho_o) \qquad (6.3)$$

V_2^b can be written as

$$\frac{V_2^b}{I} = \frac{l_2^b}{A}\rho_o \frac{(\psi_m v_1 + 1)(\psi_m v_2^b + 1)}{\psi_m v_1 + \psi_m v_2 + 2} \qquad (6.4)$$

Therefore if one has information about θ, the relative angle of the magnetization directions of the two FM layers in a GMR structure, the voltage measured in a ring-shaped structure can be calculated by Equation 6.4.

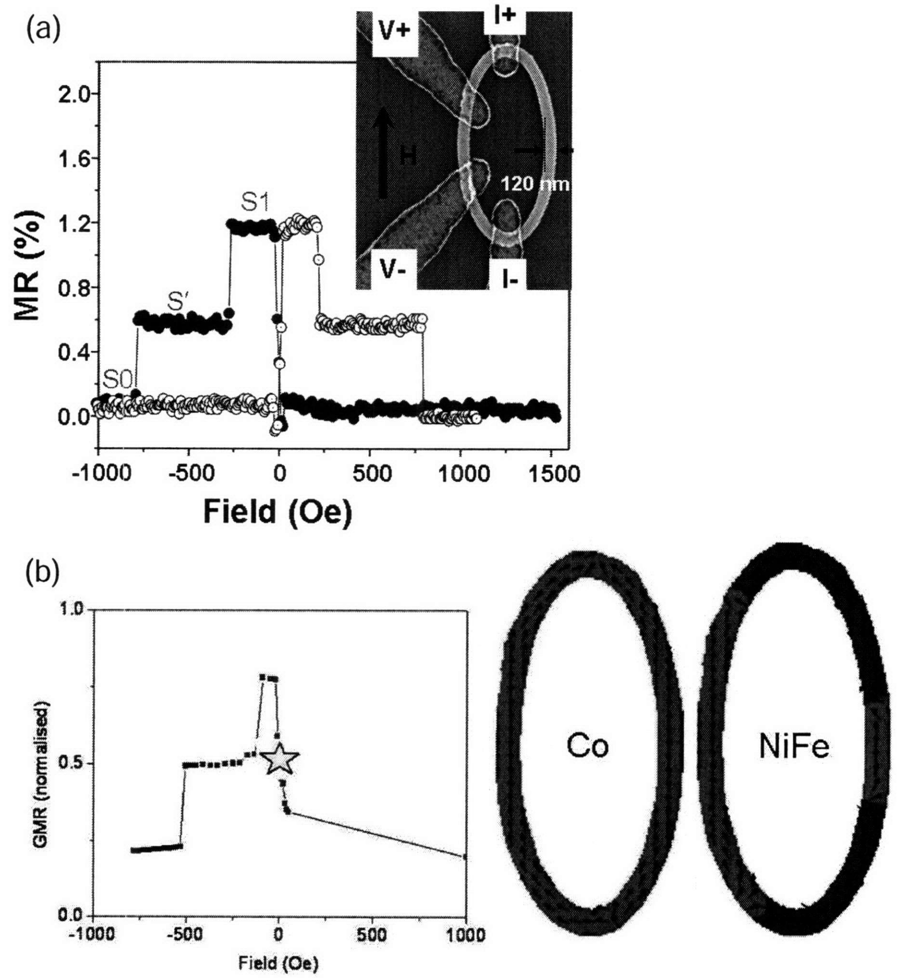

Figure 6.2 (a) MR curve obtained from a pseudo spin valve NiFe (4 nm) / Cu (6.5 nm) / Co (8 nm) elliptical ring with 3.8 / 1.9 μm major / minor diameter and width of 150 nm. A field was applied along the major axis as shown in the inset scanning electron micrograph (SEM) of the ring. Three MR states labeled as S1, S′ and S0 are shown in the curve. (b) GMR curve calculated from micromagnetic simulations for a PSV elliptical ring with 2 / 1 μm long major / minor axis, and width of 120 nm. The film structure was NiFe (4 nm) / Cu (4 nm) / Co (8 nm), and fields were applied along the major axis. Only the descending branch of the curve is shown. Spin configuration in Co and NiFe layer, shown in the right, was calculated at the field value indicated with the star in the curve. [13]

6.4 Pseudo spin valve (PSV) rings

Figure 6.2(a) shows an MR measurement on a PSV ring and 6.2(b) displays a calculated MR on a ring that has comparable dimension with the ring in the measurement [13]. The calculation was carried out using 3D OOMMF micromagnetic simulation and Equation 6.4. The simulation provides the spin configuration in each FM layer at a given field value as shown in Figure 6.2(b). The angle θ is obtained from the spin configurations and that allows computation of the giant magnetoresistance of the ring using Equation 6.4. Figure 6.2(b) shows that the calculated GMR mimics well the experimental result.

Three different MR states (S0, S1, S′) shown in the measurement (Fig. 6.2) are related to the magnetization states of the FM rings. Ring magnets typically exhibit two magnetic states. One is the onion state, in which the magnetization of each half of the ring is oriented following the boundary and two head-to-head domain walls exist, and the other is the vortex state. Various combinations of such magnetic states in the soft NiFe and hard Co layer of a spin valve ring result in different MR states (Fig. 6.3). A lowest MR state S0 is obtained with both rings being in either the onion with the same polarity or the vortex state with identical chirality. In those cases, all magnetization in the two FM rings are parallel to each other, that is, every $v = 0$ in Equation 6.4, which results in the smallest MR value. The highest MR state S1 is obtained when both FM rings are either in the onion state with antiparallel polarity or in the vortex state with the opposite chirality corresponding to every $v = 1$ in Equation 6.4. When one FM ring is in the onion state and the other is in the vortex state, that is, a half of the ring is in parallel configuration and the other half in antiparallel, the structure shows approximately a half value of the highest MR with $v_1 = 1$ and $v_2 = 0$ or vice versa (MR state S′). The micromagnetic simulation confirms that the MR state S1 corresponds to the Co and NiFe in antiparallel onion state, S0 both being in the same onion state, and S′ Co in the vortex state and NiFe in the onion state [13].

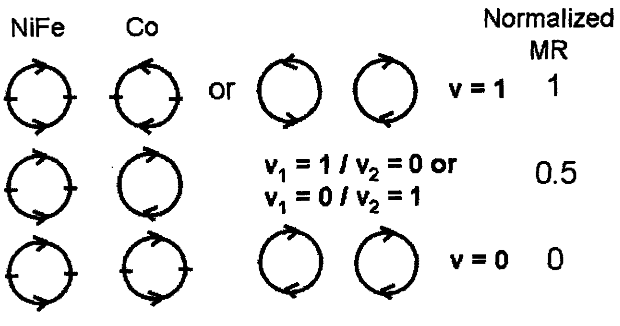

Figure 6.3 Possible combination of magnetic states in NiFe and Co ring in a spin valve ring as well as corresponding v values in Equation 6.4. Normalized MR values are shown in the right.

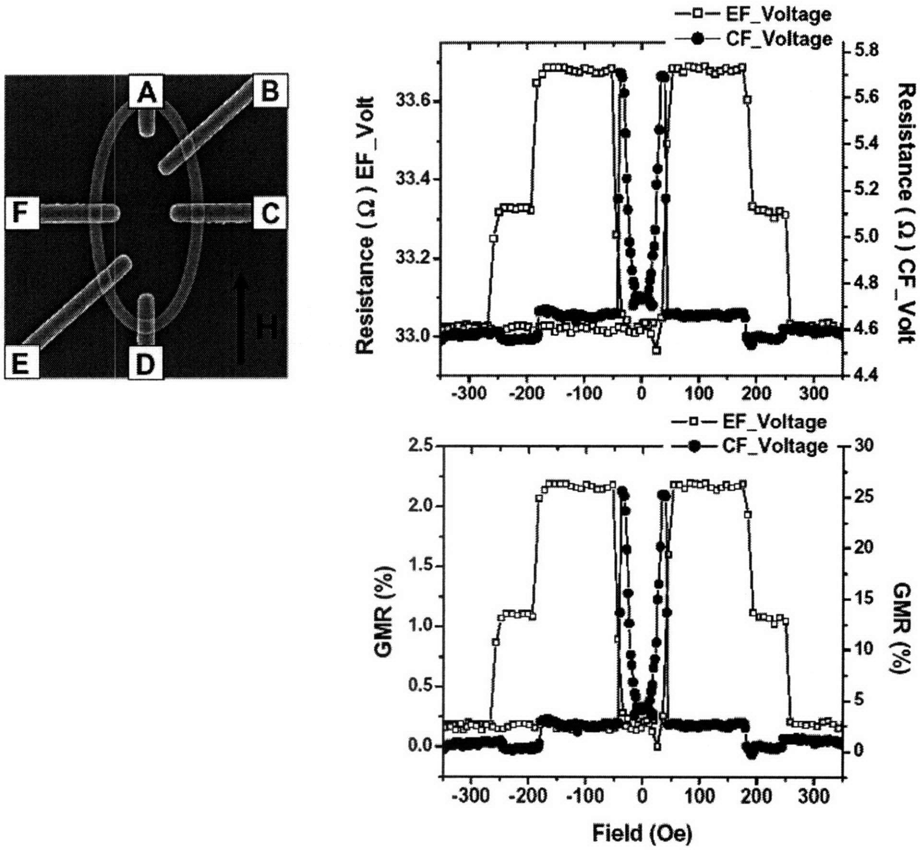

Figure 6.4 MR measurements on a NiFe (6nm) / Cu (4) / Co (5) / Au (4) PSV elliptical ring with 4 / 2 μm major / minor diameter and width of 220 nm.: (left) a SEM of the ring with labels for the contacts. The current was injected through A and D.; (right) Resistance and MR curves when the voltage is measured using E / F (open square), and C / F (solid circle).

6.5 Wheatstone-bridge contact configuration

In our CIP MR measurement configuration, MR responses are intimately dependent on which contact leads are used for flowing a current or picking up the voltage [15, 16]. Modification of the contact arrangement results in different MR responses, which, for instance, provide the details of spin configuration in a particular section of the ring [15]. The 'Wheatstone-bridge' contact configuration, which utilizes two contacts at the end of major axis of the ellipse as current leads (A, D in Fig. 6.4) and two contacts at the end of the minor axis as voltage leads (C, F in Fig. 6.4), allows an order-of-magnitude increase in the maximum MR value. Figure 6.4 shows MR measurements of a PSV ring with 4 / 2 μm major/minor diameter and width of 220 nm, in which a current flows through A / D and the voltage is measured using E / F or C / F. With the I_{AD}-V_{EF} contact configuration, which is similar to the conventional arrangement shown in Figure 6.2, the maximum MR was 2.2 %, however, the I_{AD}-V_{CF} Wheatstone-bridge configuration leads for the ring to exhibit a huge MR peak that reaches about 27%.

This increase in MR with the Wheatstone-bridge configuration can be understood by an analytical model that allows the MR of the PSV ring to be calculated as the NiFe ring switches.

In the Wheatstone-bridge contact configuration, an offset of the contact position with respect to the major / minor axis of the ellipse must exist because otherwise nonzero resistance at a high field cannot be explained (Fig. 6.5(a)).

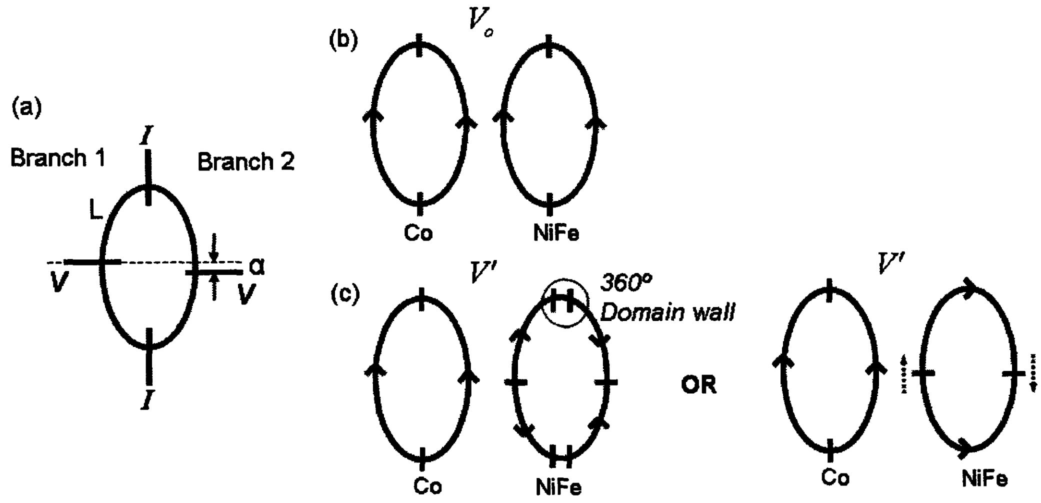

Figure 6.5 Model for the wheatstone-bridge contact configuration (a). L denotes length corresponding to a quarter of circumference of the ellipse, and α is the offset of the position of the voltage contact with respect to the minor axis of the ellipse. (b) When Co and NiFe are in the same onion state, the measurement shows the lowest voltage V_o. (c) Magnetic domain configuration that results in the highest voltage V'. Co remains in the same onion state, while NiFe reverses either by forming reversed domains accompanied by 360° domain walls or by simultaneous rotation of the onion state domain walls.

When the magnetization of the FM layers is in parallel configuration, for example both layers are in the forward onion state (Fig. 6.5(b)), the minimum voltage V_o is obtained, which is given by

$$V_o = i_2 \frac{L+\alpha}{A} \rho_o - i_1 \frac{L}{A} \rho_o = \frac{I\rho_o}{2A} \alpha \qquad (6.5)$$

L: Arclength corresponding to a quarter of circumference of the ellipse

α: Offset of the position of the voltage contact with respect to the minor axis of the ellipse.
A: Cross section area of the ring
ρ_o: Minimum resistivity of the GMR structure
ρ_m: Maximum resistivity
$i_1 = i_2 = I/2$

As the applied field reverses, a huge peak, the voltage V', appears, at which Co is still in the forward onion and the NiFe ring starts to reverse. Micromagnetic simulation suggests that NiFe switching occurs via reversed domain formation around the ends of the elliptical ring (Fig 6.2). The reversed domains might form as described in Figure 6.5(c), which occurs with 360° domain wall formation. Another possible mechanism of the NiFe reversal is simultaneous rotation of the domain walls, which leads to reverse onion state formation.

In those domain configurations described in Figure 6.5(c), the voltage V'

$$V' = i_2 \frac{L+\alpha}{A} \rho_m - i_1 \frac{L}{A} \rho_o \qquad (6.6)$$

Let $\psi_m = (\rho_m - \rho_o)/\rho_o$ and assume $i_1 = i_2 = I/2$ because L >> α, then

$$V' = \frac{I\rho_o}{2A}((L+\alpha)(\psi_m + 1) - L) = \frac{I\rho_o}{2A}((L+\alpha)\psi_m + \alpha) \qquad (6.7)$$

In this case,

$$(MR)_{WB} = \frac{R' - R_o}{R_o} = \frac{V' - V_o}{V_o} = \frac{L+\alpha}{\alpha}\psi_m \approx \frac{L}{\alpha}\psi_m \qquad (6.8)$$

The value of ψ_m can be obtained from the maximum MR value of the ring measured with a conventional contact configuration. In that case, the MR is

$$(MR)_C = \frac{(V_2^b)_{\max} - (V_2^b)_{\min}}{(V_2^b)_{\min}} \qquad (6.9)$$

which is equal to ψ_m. The maximum and minimum V_2^b,

$$(V_2^b)_{\max} = \frac{I\rho_o}{2A} l_2^b (\psi_m + 1)$$

$$(V_2^b)_{\min} = \frac{I\rho_o}{2A} l_2^b$$

are obtained from Equation 6.4, and substitution of those into Equation 6.9 results in ψ_m.

The value of $(\mathrm{MR})_C = \psi_m$ is 2.1 %. L / α = 14.3 is obtained comparing the values of $(V_2^b)_{\min}/I$ and V_o/I, 33.0 Ω and 4.6 Ω, respectively, which can be read from the experimental data (Fig. 6.4). Therefore substituting those values to Equation (6.8) results in 30% MR in the Wheatstone-bridge configuration, which is comparable to the experiment.

6.6 Spin valve (SV) rings

Figure 6.6 shows a MR measurement on a spin valve elliptical ring, in which the pinning direction is along the major axis (the exchange bias angle β = 0°) and an in-plane field is applied also along the major axis (the field angle α = 0°). After saturation of the ring, both rings are in the forward onion state at remanence, which results in the lowest MR S0. As the applied field reverses, a two-step switching of the free, soft NiFe ring occurs while the pinned, hard Co ring is still in the forward onion. The onion-to-vortex and vortex-to-reverse onion switching field of the NiFe ring were –12 Oe and –32, respectively. The vortex state in the NiFe ring sustains briefly, which is represented by the little plateau S′ shown in the first jump in the MR curve (Fig. 6.6). Such transition of NiFe leads to an antiparallel configuration in the onion states of NiFe and Co ring, which gives rise to the highest MR state S1. The highest MR maintains until Co ring switches into the vortex state at –249 Oe and further switches into the reverse onion state at –280 Oe.

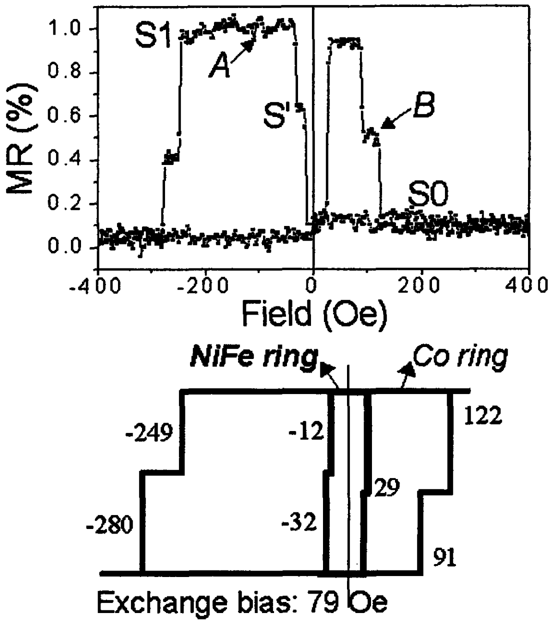

Figure 6.6 (Top) MR measurement of Ta(2nm) / NiFe(10nm) / Cu(8nm) / Co(8nm) / IrMn(5nm) / Cu(2nm) spin valve rings with major / minor diameter of 3.2 / 1.9 μm and width of 340 nm. S0, S1, and S′ denote three different MR levels. A and B represent the starting point of the minor loop MR measurement in Figure 6.7. (Bottom) Corresponding hysteresis loop speculated from the MR curve. Switching fields were labeled beside each transition and the exchange bias of Co ring was 79 Oe.

On the ascending branch, the reverse onion state of NiFe switches back into the forward onion at 29 Oe without a clear sign of the vortex formation (no plateau). The reverse onion-to-vortex transition of the Co ring occurs at 91 Oe, which is asymmetric compared to the onion-to-vortex switching field of –249 Oe. This asymmetry in the switching fields of Co ring is attributed to the exchange pinning by the neighboring AFM IrMn layer. The exchange bias deduced from the MR measurement is 79 Oe, which is smaller but comparable to the exchange bias of 104 Oe of the unpatterned film.

6.7 Minor loop MR measurement on spin valve rings

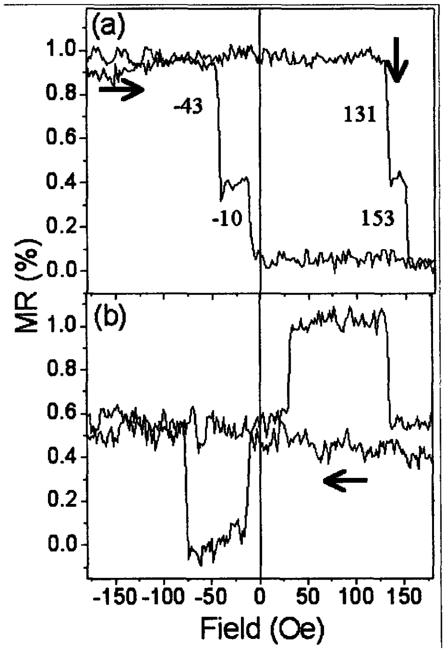

Figure 6.7 Minor loop measurement of 340 nm wide spin valve elliptical rings starting with Co: forward onion, NiFe: reverse onion (a) and Co: vortex, NiFe: forward onion (b). The field angle α = 0° and exchange bias angle β = 0°. Switching fields are labeled in (a) and the loop is shifted by 58 Oe.

Individual switching of the NiFe ring was investigated by carrying out minor loop MR measurements. A small magnitude of field was cycled, which is enough to switch NiFe, but does not disturb the Co magnetization. Figure 6.7 shows minor loops of a spin valve ring with the exchange bias angle β = 0°. The measurement was done with applying a field at the angle α = 0°. In Figure 6.7(a), the field cycle starts with NiFe in the reverse onion state and Co in the forward onion state (at A in Fig. 6.6). As the field increases, the NiFe ring switches into the vortex and then the forward onion at 131 Oe and 153 Oe, respectively. On the descending branch the NiFe switching fields are –10 and –43 Oe. Such shift in the loop can be explained taking into account the presence of the stray field emanating from the onion state Co ring, which induces an antiparallel magnetostatic coupling between the FM rings and, thus, promotes the reverse onion state in the NiFe ring. Figure 6.7(b) shows switching of the NiFe ring, which occurs while Co ring is mantained in the vortex state. (The measurement starts at B in Fig. 6.6.) The peak and dip in the loop correspond to the NiFe ring being magnetized in the vortex state. It is noteworthy that the up and down of such minor loops, which appears as the vortex state is present in both Co and NiFe ring, are determined by the relative chirality of the vortex states in each FM layer. Detection of the chirality in ring-shaped spin valve structures can be achieved by minor loop measurements with the pinned layer being in the vortex state.

6.8 Vortex chirality in spin valve rings

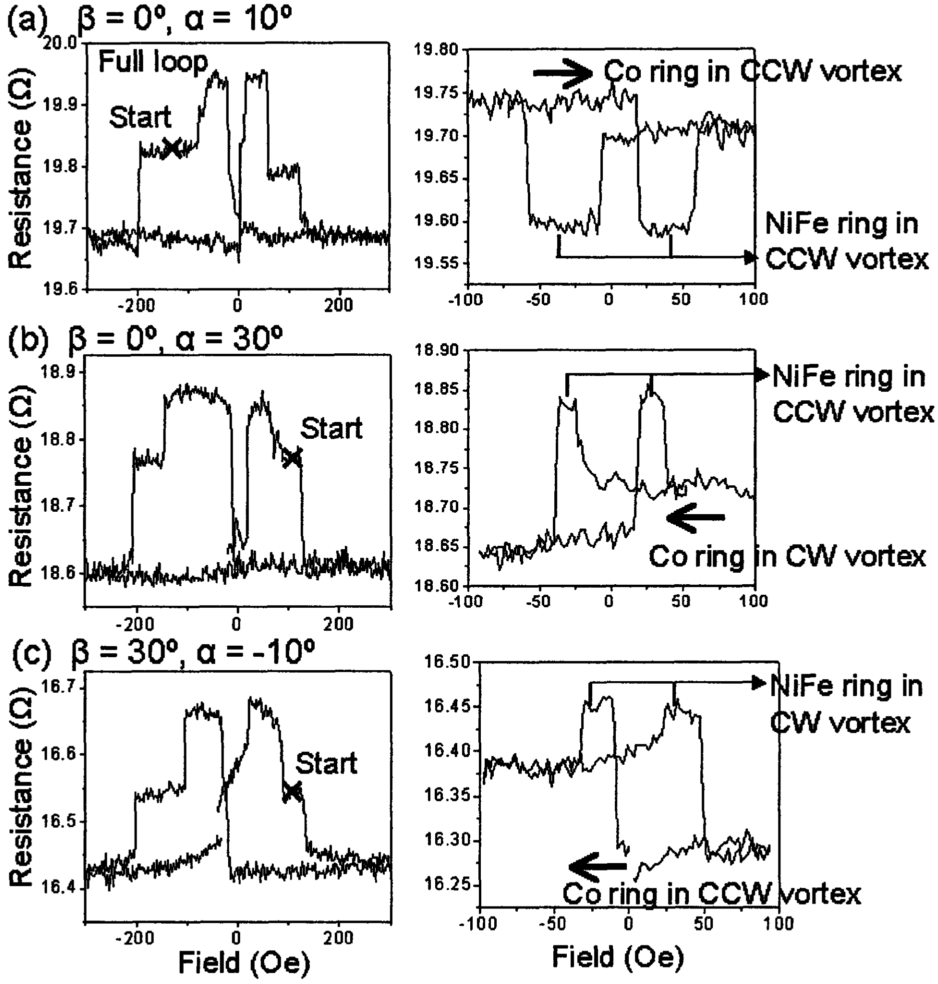

Figure 6.8 Minor loop resistance measurements on a spin valve ring with NiFe(6nm) / Cu(4nm) / Co(5nm) / IrMn(5nm) / Au(4nm), major / minor diameter: 3.1 / 1.9 μm, Width: 370 nm at β = 0°, α = 10° (a), at β = 0°, α = 30° (b), and at β = 30°, α = -10° (c). The points where a small field cycle started are marked in the full loop (Left). The chirality of Co and NiFe rings are labeled in corresponding field range (Right).

Vortex chirality control in single layer and exchange biased elliptical rings with the combination of field direction and pinning direction was demonstrated in Chapter 5 [17]. Such control was tested in the spin valve ring, which consists of single layer and exchange bias structure with a Cu spacer in between. Minor loops for vortex-state pinned layer were measured at various pinning directions and field directions with respect to the major axis (Fig. 6.8). Figure 6.8(a) shows the minor loop measurement as $\beta = 0^\circ$ and $\alpha = 10^\circ$ on the ring shown in Figure 6.1(b). Chapter 5 suggests that in single layer elliptical rings if $0^\circ < \alpha < 90^\circ$ the chirality is CCW and if $-90^\circ < \alpha < 0^\circ$ it is CW, where the critical angle $\alpha_c = 0^\circ$. In the exchange-biased rings the critical angle α_c is approximately equal to the exchange bias angle β of the ring. CCW vortex appears at $\alpha > \alpha_c$ and CW vortex at $\alpha < \alpha_c$. Therefore, at $\beta = 0^\circ$ and $\alpha = 10^\circ$, the chirality of both free layer and pinned layer would be CCW. After saturating the ring with a positive field, a field sweep to –100 Oe makes the Co ring to be in the CCW vortex state as shown in the full loop. The chirality of the NiFe vortex state, which forms during the small field cycling, is also CCW. Therefore, there appear two dips in the minor loop. The direction of the saturating field is an important factor to determine the Co vortex chirality. At $\beta = 0^\circ$ and $\alpha = 30^\circ$ (ring shown in Fig. 6.1(c)), if the ring is saturated with a negative field, the effective α becomes -150° for the exchange-biased Co ring, at which the chirality is predicted to be clockwise (CW). However, in single layer rings, the polarity of the saturating field has no influence on determination of the vortex chirality. The CCW NiFe vortex chirality with $\alpha = 30^\circ$ and CW Co vortex state lead to the increases in MR in the minor loop (Fig. 6.8(b))

The vortex chirality in spin valve rings with any pinning direction and field direction can be predicted and the relative chirality configuration can be confirmed from the minor loop measurements. With $\beta = 30^\circ$, $\alpha = -10^\circ$ (Fig. 6.1(d)), and negative saturation, the Co vortex would be CCW and NiFe would be CW, which results in the two peaks shown in the measurement (Fig. 6.8(c)). The discrepancy in the resistance value of S′ state between each side of the minor loop is attributed to the displacement of the position of the NiFe onion state domain walls, which is determined by the field direction with respect to the major axis and exchange coupling with the magnetization of the Co ring. When $\beta = 0^\circ$ and $\alpha = 0^\circ$, no discrepancy appears (Fig. 6.7(b)). The remanent domain wall position in single layer and exchange-biased rings is dependent on the field angle and exchange bias angle (Fig 5.2 and 5.5).

6.9 Summary

In this chapter, magnetic states and magnetization reversal of ring-shape multilayered structures were investigated and understood by using MR measurements and micromagnetic modeling. Also different MR responses depending on the electric contact configuration were observed in ring devices. For instance, a large increase in MR signal occurred with a Wheatstone-bridge type contact configuration, which was explained by an analytical model.

The vortex chirality control in multilayered rings is successfully demonstrated based on the understandings on the vortex chirality of single layer and exchange bias rings. The application of a small in-plane field at the field angle α on a spin valve ring pinned at the angle β allows for each FM layer to have a desired vortex chirality and enables modification of the MR states in minor MR loops. The MR states are determined by a combination of three different parameters, the field angle, exchange bias angle, and the saturation direction. Those parameters can be modified at any time, even as the exchange bias direction is allowed to be tuned by field cooling. Such a variety of the parameters and controlled MR response lead for the spin valve rings to have great potential to be utilized as magnetic logic devices.

Reference

[1] J. G. Zhu, Y. F. Zheng, and G. A. Prinz, Journal of Applied Physics **87**, 6668 (2000).

[2] M. Klaui, J. Rothman, L. Lopez-Diaz, *et al.*, Applied Physics Letters **78**, 3268 (2001).

[3] R. Nakatani, T. Yoshida, Y. Endo, *et al.*, Journal of Applied Physics **95**, 6714 (2004).

[4] E. Saitoh, M. Kawabata, K. Harii, *et al.*, Journal of Applied Physics **95**, 1986 (2004).

[5] P. Vavassori, R. Bovolenta, V. Metlushko, *et al.*, Journal of Applied Physics **99**, 053902 (2006).

[6] F. Q. Zhu, G. W. Chern, O. Tchernyshyov, *et al.*, Physical Review Letters **96**, 027205 (2006).

[7] R. Nakatani, T. Yoshida, Y. Endo, *et al.*, Journal of Magnetism and Magnetic Materials **286**, 31 (2005).

[8] M. T. Moneck and J. G. Zhu, Journal of Applied Physics **99**, 08H709 (2006).

[9] N. Dao and S. L. Whittenburg, IEEE Transactions on Magnetics **39**, 2525 (2003).

[10] J. Guo and M. B. A. Jalil, IEEE Transactions on Magnetics **40**, 2122 (2004).

[11] C. C. Chen, C. C. Chang, Y. C. Chang, *et al.*, IEEE Transactions on Magnetics **43**, 920 (2007).

[12] C. C. Chen, C. C. Chang, C. Y. Kuo, *et al.*, IEEE Transactions on Magnetics **42**, 2766 (2006).

[13] F. J. Castano, D. Morecroft, W. Jung, *et al.*, Physical Review Letters **95**, 137201 (2005).

[14] F. J. Castano, D. Morecroft, and C. A. Ross, Physical Review B **74**, 224401 (2006).

[15] D. Morecroft, F. J. Castano, W. Jung, *et al.*, Applied Physics Letters **88**, 172508 (2006).

[16] D. Morecroft, F. J. Castano, W. Jung, *et al.*, Journal of Applied Physics **99**, 08T504 (2006).

[17] W. Jung, F. J. Castano, and C. A. Ross, Physical Review Letters **97**, 247209 (2006).

Chapter 7

Conclusions and future work

7.1 Conclusions

This thesis investigated the equilibrium magnetic states and magnetization reversal of the multi-layered elliptical rings, focusing on the vortex magnetic state which has been proposed as a data storage token in ring-shaped magnetic memory devices.

Hysteresis measurements were carried out on the arrays of NiFe / FeMn exchange-biased elliptical rings varying the applied field angles with respect to the pinning direction, and the effect of the shape and exchange anisotropy on the vortex state formation was investigated. The hysteresis loop exhibits two step switching, which indicates formation of the vortex state, only when a field is applied at an angle close to the bias direction. This suggests that there exists an easy axis field direction, at which the vortex state formation is most favored. Using an analytical model, the easy axis set by the uniaxial shape anisotropy and unidirectional exchange anisotropy was calculated, which was comparable to the experiment.

In addition to the study on the formation of the vortex state, chirality of the vortex state, which is utilized to store data bits in ring-shaped memory devices, was explored. The effect of elliptical shape and exchange pinning on the vortex state chirality was investigated and control of the chirality was demonstrated in exchange-biased elliptical rings by modifying the field direction and pinning direction. With an analytical model, the energy change of the ring was calculated for clockwise (CW) and counterclockwise (CCW) motions of an onion state domain wall during the onion-to-vortex transition, which allows prediction of the vortex chirality. The model suggests that in a single layer elliptical ring if the relative angle α between the applied field direction and major axis is $0° < \alpha < 90°$ a CCW vortex is expected and a CW vortex if $-90° < \alpha < 0°$, therefore, the critical angle $\alpha_c = 0°$. In the exchange-biased rings with strong exchange coupling the critical angle α_c is approximately equal to the exchange bias angle β of the ring. CCW vortex appears at $\alpha > \alpha_c$ and CW vortex at $\alpha < \alpha_c$. This model was confirmed by experimental observations using magnetic force microscope (MFM). Based on the calculation and experiment at various field angle and exchange bias angle, a phase diagram of vortex chirality in the exchange-biased elliptical ring was plotted.

NiFe / Cu / Co pseudo spin valve (PSV) and NiFe / Cu / Co / IrMn spin valve (SV) rings were fabricated and their giant magnetoresistance (GMR) was measured in the current-in-plane geometry. PSV and SV elliptical rings show multiple MR states, which might enable for each ring-shape memory cell to carry more than one bit of data. The details of the switching behavior and magnetic states of the GMR ring structures were revealed by

3D OOMMF micromagnetic simulations. The vortex chirality control of each ferromagnetic (FM) layer in multi-layered rings is successfully demonstrated by minor loop MR measurements, in which a small magnitude of field is swept in order to reverse only the soft layer of the spin valve. The vortex chirality of each FM layer in the structure was manipulated by tailoring the field angle, exchange bias angle, and the saturation direction relative to the major axis of the ring. Such a control on the chirality leads for the spin valve rings to have great potential to be utilized as magnetic memory and logic devices.

7.2 Future work

Exchange-biased elliptical rings provide a unique opportunity to explore how the shape anisotropy and exchange anisotropy interact and affect the magnetization reversal and magnetic states of the rings. In this thesis, it has been shown that the vortex state formation and chirality is dependent on the field angle relative to the pinning direction of the ring. The results would become more comprehensive if micromagnetic simulations are carried out for the exchange-biased elliptical rings, which reveal the details of magnetization states in the rings.

In the thesis, the onion states in exchange-biased elliptical rings were imaged at remanence by MFM and the position of the wall was measured at different field angle and exchange bias angles. These data indicate that the domain wall position lags behind the field angle change as the field deviates from the major axis or exchange pinning direction of the ring, which suggests strong influence of shape anisotropy and exchange anisotropy on the remanent onion state wall position. It has been shown that those anisotropies are also intimately related to the vortex state formation and vortex chirality. Further modeling studies on the shape and exchange anisotropy in elliptical rings would provide useful insights into complete understanding of the switching behavior of exchange-biased rings.

Study on the MR transition and vortex chirality control in GMR rings, shown in this thesis, is an important first step for the development of ring-shaped memory and logic devices. For those devices to be more practical, the ring size needs to be significantly reduced. Miniaturization of the ring devices not only presents difficulties in fabrication but also requires different physics to understand the phenomena. For example, in the ring with the outer diameter of several tens of nanometers, the vortex state could be no longer stable due to the surge of exchange energy caused by the high curvature. Also the MR of the spin valve rings should be enhanced by at least an order of magnitude, which could be achieved by employing magnetic tunnel junction (MTJ) structure (Chapter 1.4.4).

In our spin valve ring devices, the switching was induced by application of in-plane external fields, which can be practiced in actual devices by passing a current through word lines beside the magnetic cell. Current induced switching, which uses spin transfer from the current-perpendicular-plane (CPP) current to switch a neighboring FM layer, allows faster, more controlled switching that is free from a long range external field [1-3]. Ring-shaped vertical GMR [4, 5] or MTJ [6] structures reversed by CPP spin torque transfer would be an ideal cell structure of high-density magnetic random access memories (MRAM). In addition, logic operations could be performed in the ring magnets by current driven motion [7, 8] of 180° walls in the onion state or 360° walls in the twisted state, which could allow such a multi-layered ring structure to incorporate both the memory and logic function in one cell.

Reference

[1] J. Grollier, V. Cros, A. Hamzic, *et al.*, Applied Physics Letters **78**, 3663 (2001).

[2] E. B. Myers, D. C. Ralph, J. A. Katine, *et al.*, Science **285**, 867 (1999).

[3] J. C. Slonczewski, Journal of Magnetism and Magnetic Materials **159**, L1 (1996).

[4] K. Bussmann, G. A. Prinz, S. F. Cheng, *et al.*, Applied Physics Letters **75**, 2476 (1999).

[5] M. T. Moneck and J. G. Zhu, Journal of Applied Physics **99**, 08H709 (2006).

[6] C. C. Chen, C. C. Chang, C. Y. Kuo, *et al.*, IEEE Transactions on Magnetics **42**, 2766 (2006).

[7] M. Tsoi, R. E. Fontana, and S. S. P. Parkin, Applied Physics Letters **83**, 2617 (2003).

[8] D. A. Allwood, G. Xiong, C. C. Faulkner, *et al.*, Science **309**, 1688 (2005).